High-Performance Organic Light-Emitting Diodes for Flexible and Wearable Electronics

A Dissertation
Presented to
The Academic Faculty

by

Michael P. Gaj

In Partial Fulfillment
of the Requirements for the Degree
Doctor of Philosophy in the
School of Electrical engineering

Georgia Institute of Technology
May 2016

High-Performance Organic Light-Emitting Diodes for Flexible and Wearable Electronics

Approved by:

Dr. Bernard Kippelen
School of Electrical Engineering
Georgia Institute of Technology

Dr. Andrew Peterson
School of Electrical Engineering
Georgia Institute of Technology

Dr. Benjamin Klein
School of Electrical Engineering
Georgia Institute of Technology

Dr. Peter Hesketh
School of Mechanical Engineering
Georgia Institute of Technology

Dr. David Citrin
School of Electrical Engineering
Georgia Institute of Technology

Date Approved: March 29, 2016

ACKNOWLEDGEMENTS

None of the work presented in this thesis would have been possible without the generous support of all my friends, family and colleagues. First, I would like to thank my adviser, Prof. Bernard Kippelen, for the central role he played in the development of this work and my development as an individual. Bernard's constant demand for high quality results and high standards for science were instrumental in my personal development and provided me with skills that I will carry for the rest of my professional career. I am truly grateful for all of his support, guidance, and insights. I would also like to thank Prof. Benjamin Klein and Prof. David Citrin for the time they have taken to serve as members of my dissertation reading committee. These roles are not mandatory and your willingness to serve on my committee will not be forgotten – thank you.

This work was heavily dependent on teamwork, and it would not have been possible without the current (and former) members of the Kippelen lab. Specifically, Keith Knauer and Wojciech Haske, who both took it upon themselves to train me in proper practice and techniques in the lab. These two were instrumental in mentoring me during my first two years in Prof. Kippelen's group and became not only good colleagues, but great friends. I would also like to thank Dr. Canek Fuentes-Hernandez for all his great technical advice and refinement on everything from proof-reading manuscripts, to in depth discussions on the most difficult challenges posed by my research. Additionally, I would like to thank members of other groups whose assistance is represented in this work. Dr. Yadong Zhang from Prof. Seth Marder's group is a wizard in the chemistry lab and his creativity/mastery provided me with all the necessary materials needed to solve the tough problems presented

in this work. Additionally, I would like to thank Andrew Wei and Prof. Walter Voit from the University of Texas at Dallas for their support in the shape memory polymer synthesis.

It is expensive to run a lab, and there are many organizations that made this work financially possible. This work was made possible through contracts with Applied Materials, Mitsubishi Chemical, Solvay, Corning Inc., Samsung, the National Science Foundation's STC program under Agreement No. DMR-0120967, and the Department of Energy under Agreement No. DE-FG02-04ER46165.

Last, but certainly not least, I would like to thank all of my friends and family. Their continued support provided light in even the darkest of nights and gave this journey meaning. Thank you to Carly for enduring through the Ph.D. process and providing me with unwavering support – you're the best, Bugga Boo. In particular, thank you to my father, mother, brother and sister. My achievements are your achievements and they could not be possible without all your sacrifices and support throughout the years. I strive to make you all proud.

TABLE OF CONTENTS

LIST OF TABLES

LIST OF FIGURES

LIST OF SYMBOLS AND ABBREVIATIONS

OLED	Organic Light-Emitting Diode
LCD	Liquid Crystal Display
TFT	Thin-Film Transistor
AMOLED	Active Matrix OLED
ITO	Indium Tin Oxide
TAPC	4,4’-Cyclohexylidenebis[N,N-bis(4methylphenyl)benzamine]
Alq_3	8-hydroxyquinoline aluminum
EQE	External Quantum Efficiency
IQE	Internal Quantum Efficiency
HTL	Hole Transporting Layer
HIL	Hole Injecting Layer
ETL	Electron Transporting Layer
EIL	Electron Injecting Layer
EML	Emissive Layer
TIR	Total Internal Reflection
T_g	Glass Transition Temperature
FIrpic	Iridium(III)bi[(4,6-di-fluorophenyl)-pyridinato-N,C2’]picolinate
CBP	4,4’-bis(N-carbazolyl)-1,1’-biphenyl
$Ir(ppy)_3$	Tris(2-phenylpyridine)iridium(III)
$Ir(ppy)_2(acac)$	Bis[2-(2-pyridinyl-N)-C](2,4-pentaneditonato-O,O)iridium(III)
TPBi	2,2′,2"-(1,3,5-Benzinetriyl)-tris(1-phenyl-1-H-benzimidazole)
TCTA	4,4’,4”-tris(carbazol-9-yl)-triphenylamine
B3PYMPM	bis-4,6-(3,5-di-3-pyridylphenyl)- 2-methylpyrimidine

TADF	Thermally Activated Delayed Fluorescence
4CzIPN	(4s,6s)-2,4,5,6-tetra(9H-carbazol-9-yl)isophthalonitrile
DMAC-DPS	Bis[4-(9,9-dimethyl-9,10-dihydroacridine)phenyl]sulfone
PEDOT:PSS	Polyethylene dioxythiophene-polystyrene sulfonate
PET	Polyethylene Terephthalate
PES	Polyethersulfone
WVTR	Water Vapor Transmission Rate
TFE	Thin-Film Encapsulation
PECVD	Plasma Enhanced Chemical Vapor Deposition
UDC	Universal Display Corporation
VTE	Vacuum Thermal Evaporation
OVPD	Organic Vapor Phase Deposition
HOMO	Highest Occupied Molecular Orbital
LUMO	Lowest Unoccupied Molecular Orbital
EA	Electron Affinity
IE	Ionization Energy
SCLC	Space-Charge-Limited Current
NR	Non-Radiative
ISC	Intersystem Crossing
RISC	Reverse Intersystem Crossing
SPA	Singlet-Polaron Annihilation
SSA	Singlet-Singlet Annihilation
STA	Singlet-Triplet Annihilation
TPA	Triplet-Polaron Annihilation
TTA	Triplet-Triplet Annihilation

PL	Photoluminescence
CIE	Commission Internationale de l'Eclairage
PE	Power Efficacy
CRI	Color Rendering Index
α-NPD	N,N'-di(naphthalene-1-yl)-N,N'-diphenyl-benzidine
BCP	2,9-dimethyl-4,7-diphenyl-1,10-phenanthroline
TAZ	3-phenyl-4-(1'-naphthyl)-5-phenyl-1,2,4-triazole
TPBi	1,3,5-tri(phenyl-2-benzimidazole)-benzene
TpPyPB	1,3,5-tri(p-pyrid-3-yl-phenyl)benzene
mCPSOB	3,5-di(carbazol-9-yl)-1-phenylsulfonylbenzene
Poly-TriCZ	9,9'-(5-(phenylsulfonyl)-1,3-phenylene)bis(9H-carbazole)
2CzPN	1,2-bis(carbazol-9-yl)-4,5-dicyanobenzene
SMP	Shape Memory Polymer
EL	Electroluminescence
TATATO	1,3,5-triallyl-1,3,5-triazine-2,4,6(1H,3H,5H)-trione
TMTMP	Trimethylolpropane tris(3-mercaptopropionate)
TCMDA	Tricyclo [5.2.1.02,6] decanedimethanol diacrylate
DMPA	2,2-dimethoxy-2-phenylacetophenone
PVDF	Electroluminescence
DMA	Dynamic mechanical analysis

SUMMARY

Optoelectronic devices based on organic semiconductors have been the focus of increasing research over the past two decades. While many of the potential organic electronic concepts (solar cells, transistors, detectors etc.) are still in their infancy stage, organic light-emitting diodes have gained commercial acceptance for their potential in high resolution displays and solid-state lighting. The intrinsic advantages of this materials have allowed them to steal the imagination of engineers and scientists who look to exploit their many advantageous device characteristics for next generation consumer electronics. These include low power consumption and heat dissipation, a tunable color gamut, ease of manufacturing and the potential for flexible, deformable and conformable form factors. However, in order for these devices to reach their full potential significant advances need to make to address their fundamental limitations, specifically: device life-time, thin-film encapsulation and scalability to a high volume manufacturing setting.

The work presented in this thesis demonstrates new strategies to design and manufacture high performance OLEDs for next generation electronics. In the first part, high performance OLEDS using a simple three-layer organic semiconductor device structure are demonstrated. These devices utilizes two novel materials (Poly-TriCZ and mCPSOB) to achieve efficient charge balance and exciton confinement in the emissive region of the device. Moreover, the electrical properties of these materials allow them to serve as a suitable ‘universal’ material combination to yield high performance OLEDs with high energy phosphors (i.e. blue- or deep-blue-emitting dopants). To demonstrate this feature, green-emitting and blue-emitting OLED results are provided that define the state-of-the-art for phosphorescent OLEDs. These results are then extended to demonstrate high

performance with a new set of high efficiency blue-emitting and green-emitting dopants based on thermally activated delayed fluorescence (TADF), which also proceed to define the state-of-the-art in electroluminescence from TADF.

The second part of this thesis extends on the work from part one and demonstrates high-performance OLED potential on a new class of polymeric substrates called shape memory polymers (SMPs). SMPs offer to provide a new alternative to flexible, polymeric substrates due to their unique mechanical properties. When an external stimuli is applied to these materials (heat), they have the ability to form a temporary phase that has a Young's modulus orders of magnitude lower than its original state. The material can then be re-shaped, deformed or conform to any object until the stimuli is removed, at which point the Young's modulus returns to its original state the temporary geometric configuration is retained. Re-applying the stimulus will trigger a response in its molecular network which induces a recovery of its original shape. By using mCPSOB in an inverted top-emitting OLED architecture, green-emitting OLEDs are demonstrated on SMP substrates. The combination of the unique properties of SMP substrates with the light-emitting properties of OLEDs pave to the way for new applications, including conformable smart skin devices, minimally invasive biomedical devices, and flexible lighting/display technologies.

CHAPTER 1

INTRODUCTION

Over the last couple decades, organic light-emitting diodes (OLEDs) have been the focus of intense research in both academia and private industry. Their unique qualities make them ideal candidates for next-generation display and solid-state lighting technologies. In this chapter, the reader will be introduced to the basics of OLED technology, its history and current state-of-the-art design, and the future of OLEDs as predicted by industry experts. The inherit advantages of OLEDs will become more obvious through a side-by-side comparison to existing and competing technologies in both industries. This chapter will conclude with an overview of the challenges OLED technology much overcome to reach its full potential, followed by an overview of the structure for the proceeding chapters of this dissertation.

1.1 Organic Light-Emitting Diodes

In their simplest form, OLEDs are electroluminescent devices consisting of multiple organic layers sandwiched between two electrodes (an anode and a cathode) [1]. Figure 1.1 shows a simplified illustration of a single layer OLED. In this particular configuration, holes and electrons are injected and transported through the organic material under a forward bias voltage *V*, with the positive terminal connected to the anode and the negative terminal connected to the cathode. These charges work their way through the organic materials, towards the center of the device under the influence of the applied electric field, and recombine in the form of electron-hole pairs called excitons. Light is emitted when

these exited states decay and release their energy through the emission of a photon, which exits the device through either a semi-transparent anode or cathode.

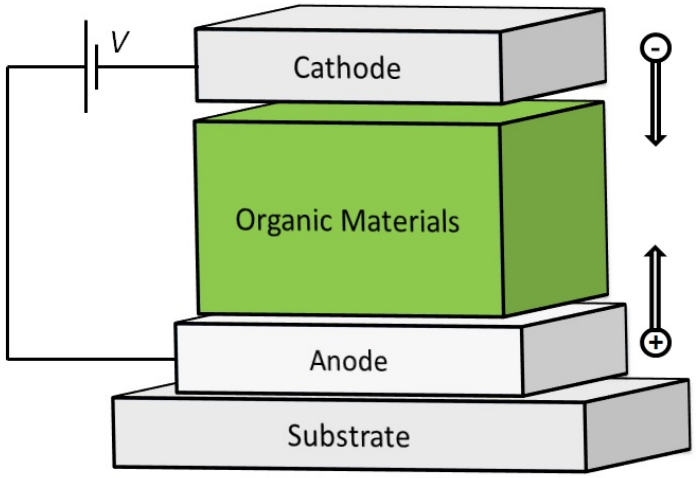

Figure 1.1 Simplified single layer OLED structure.

The market potential for OLEDs has mainly focused on two large industries so far: displays and solid-state lighting. The adoption of OLEDs for displays has seen substantially larger growth and market penetration than OLEDs for solid-state lighting, but both show promise and they are expected to see tremendous growth over the next decade as companies continue to devote resources and create the infrastructure necessary for low-cost, large scale manufacturing [2].

1.2 Applications

The massive growth of the consumer electronics industry over the past decade has helped OLED technology grow from a research lab concept to a commercially viable technology. OLEDs are now being used as the emissive element in many modern day consumer electronic devices, such as: smart phones, smart watches, digital cameras, tablets

and televisions. This technological movement is being driven by large electronic companies such as Samsung, LG, Panasonic and Apple. Both Samsung and LG are utilizing OLEDs in their current smart phone offerings (Samsung Galaxy 6/6 Edge and LG G Flex), while Apple has recently started their use of OLEDs for the display in their newest product Apple Watch. The most striking example of the progress OLEDs have made over the last decade can be seen by comparing the cost of OLED televisions. In 2013, a 55" Samsung OLED TV had a retail price of $8,999.99 [3]. At the time of this writing, LG is selling a similar 55" OLED TV for $1,899.99 (LG EC9300) [4]. This drastic price drop over two years illustrates the progress these companies are making with large scale OLED manufacturing, and it is the author's opinion that these prices will only continue to drop to levels comparable to LCD/LED technologies in the years ahead.

Figure 1.2 Consumer products with an AMOLED display. (a) Samsung Galaxy 6, (b) LG G Flex, (c) Apple Watch, (d) LG EC9300 55" TV

The commercial appeal of OLEDs for displays can best be described through a comparison of its main competing technology: liquid-crystal displays (LCDs). LCDs have been the dominant technology for flat panel displays, and continue to be the benchmark that all competing technologies are compared. But liquid crystals do not themselves emit light and must be integrated with a diffuse backlighting source, such as a diffusive film with embedded LEDs. Because of this, the modern LCD is a complex structure that incorporates a thin-film transistor (TFT) backplane, a series of polarizers, spacers, color filters and a backlight in order to produce an image on a display [5]. Figure 1.3 provides a cross-sectional view of the LCD module and its various components.

Liquid crystals operate through a principle called the twisted nematic effect [6]. In the absence of an electric field, the liquid crystal molecules will rotate by 90-degree in the layer along the axis of the liquid crystals. This will allow the light to transmit through an orthogonal polarizer and produce a bright pixel. Conversely, when a voltage is applied across the cell, the molecules of the liquid crystal align parallel to the electric field and no longer rotate the polarization of the light. Thus, the light is blocked by the second crossed polarizer resulting in a dark screen. Additionally, the strength of the electric field across the liquid crystal layer can be controlled by changing the voltages applied to the pixel electrode, which can further modulate the strength of the incident light and produce a gray level screen between fully bright and completely dark [7]. Color is achieved by subdividing each pixel into red, green and blue subpixels that are created by allowing the white backlight to pass through appropriate color filters [8]. This process is highlighted in Figure 1.4.

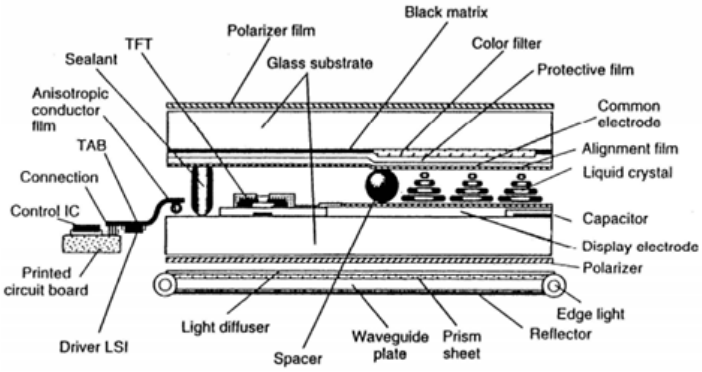

Figure 1.3 Cross-sectional view of LCD module. Figure from [6].

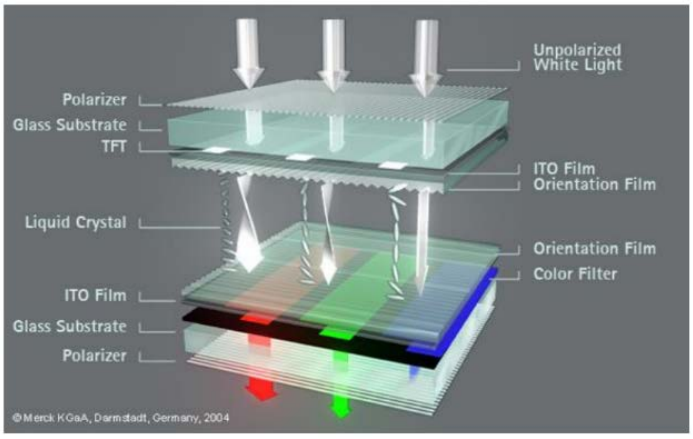

Figure 1.4 Twisted nematic operational process for an LCD module. Figure from [7].

The modern day LCD utilizes active matrix addressing, which allows each pixel to be controlled independently by an individual circuit comprising of 2-6 transistors. This technique results in displays with faster response times, higher contrast ratios and higher resolutions than the alternative passive-matrix addressing technique [9]. Commercial OLED displays also utilize active matrix addressing and are commonly referred to as active-matrix organic light-emitting diode (AMOLED) displays. This similarity has made allowed manufactures to utilize existing infrastructure and technical competence to make

the transition to AMOLED displays more efficiently. However, that is where the similarities end.

Unlike LCDs, each OLED pixel is itself a light-emitting source. That means there is no need for any diffuse backlighting source, color filters or spacers. For an AMOLED display, the OLEDs are deposited directly on top of the TFT backplane and the display is complete, excluding an encapsulation layer. The simplicity of this design is highlighting in Figure 1.5, which compares a basic LCD to an AMOLED.

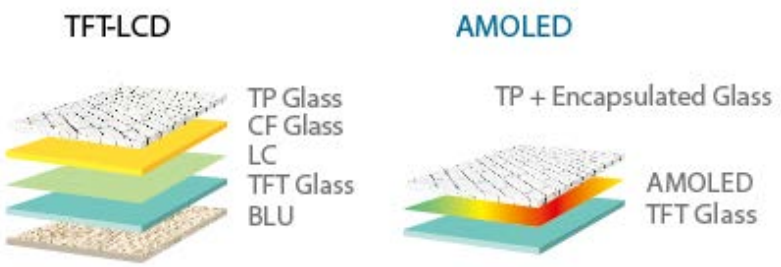

Figure 1.5 Components of a (left) TFT-LCD and (right) AMOLED display. Figure from [10]

This simplicity and elegance provides AMOLED displays with a long list of advantages over LCDs [9]. These include:

- Higher resolution
- Wide-viewing angles
- Wide color gamut
- Ultra-high contrast ratios
- Fast response times to reduce motion blur
- Ultra-thin and potential flexible form factors
- OLED screens can be semi-transparent

The most important advantage of AMOLED vs. LCD, however, is its low energy consumption. Because OLED pixels directly their desired light and black pixels in OLED displays are electrically inactive, they are extremely energy efficient and require 40 – 50% of the power an LED/LCD display consumes [11]. In contrast, only 10% of the diffuse backlighting source is transmitted through the various components in an LCD module [12]. Because of these advantages, the market forecast for OLED displays is expect to grow nearly eight-fold over the next 5 years [13].

In their most recent report, IDTechEx predicted that the market for OLED displays with grow from $2 billion in 2015 to nearly $16 billion in 2020 [14]. These findings are contained in Figures 1.6a and 1.6b. Figure 1.6a illustrates the annual revenue for OLED displays over the next five years, while Figure 1.6b breaks this down into market segment.

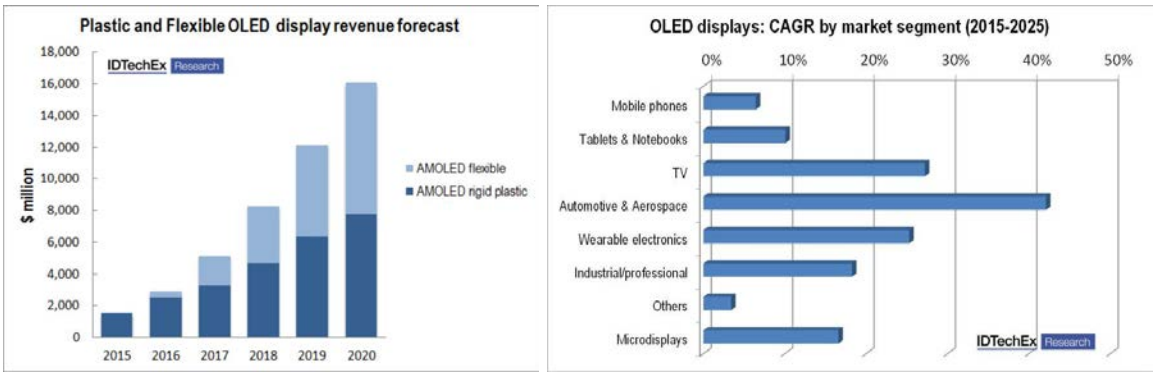

Figure 1.6 OLED display revenue (left) and CAGR by market segment (right) forecast. Figures from [14].

This large growth in revenue is expected to be fueled by the growth and demand for flexible and wearable electronics, which by 2020 is expected to be greater than that for rigid electronics. Of more interest though is the market segments driving this growth. Of more interest through is the market segments driving this growth. Mobile phones are already a

mature industry where OLEDs have proven to be the dominant technology. Because of this, experts do not expect it to contribute much to the OLED display growth. This growth is expected to come from large screen televisions, the automotive and aerospace industry, and wearable electronics.

Compared to OLED displays, OLED lighting is still gaining momentum and steps away from full-level commercialization. Compared to its strongest competitor (LED lighting), OLEDs offer the advantages of low heat generation, color tenability and flexible form factors. Currently, the manufacturing costs of an OLED lighting panel is still a large hurdle needed to overcome before they can directly compete with LED lighting options. However, as the industry and manufacturing processes becomes more mature, it is expected that the retail prices will decrease and the lifetimes will increase and OLED lighting modules can become cost competitive with competing technologies. This obstacle hasn't prevented companies like Seimens [15] and Acuity [16] from releasing next generation OLED lighting prototypes that promise to produce environmentally friendly lighting in new design mediums, as shown below in Figure 1.7.

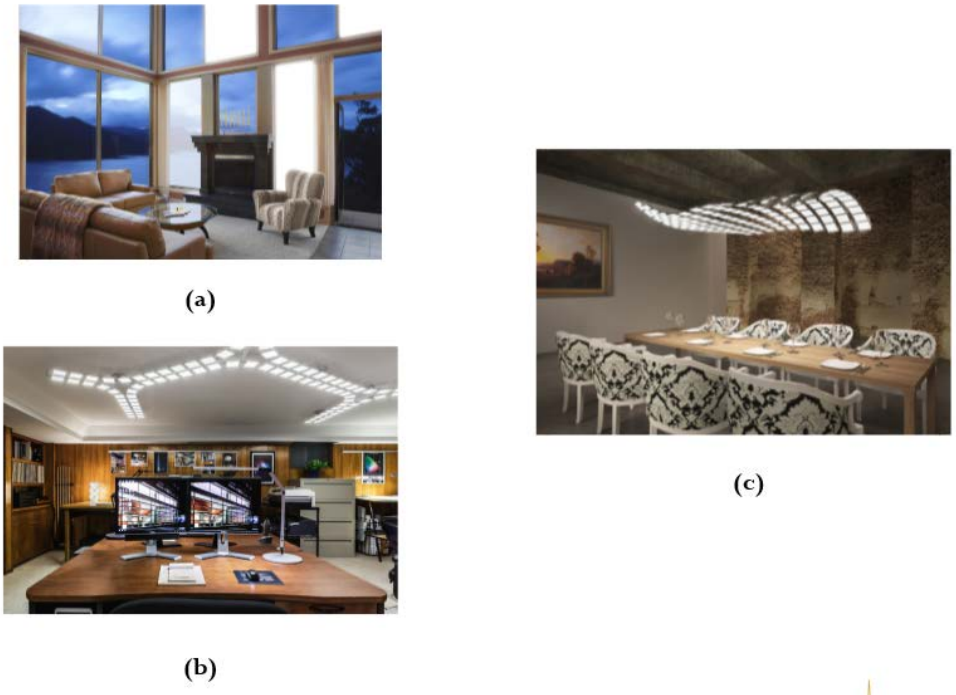

Figure 1.7 Next generation OLED lighting prototypes from: (a) Seimens, (b) Acuity brands and (c) Selux

1.3 A Brief History of OLEDs

The first report of a simple and efficient OLED structure was presented by Tang and Van Slyke in 1987 [1]. While working at Eastman Kodak, they were able to show electroluminescence from a two-layer organic stack, between an ITO bottom anode and silver cathode. Their organic structure consisted of the aromatic amine TAPC as a hole conductor and AlQ_3 as the electron transport material and emitter. This fluorescent device produced an external quantum efficiency (EQE) of 1%, a power efficacy of 1.5 lm/W and achieved a maximum luminance of over 1,000 cd/m^2 [1]**.** Electroluminescence from organic materials had been presented in the past [17, 18], but this structure was the first to

achieve an EQE above 1% and produce high luminance values. These performance metrics will all be discussed in more detail in Chapter 3.

Fluorescent emitters remained the state-of-the-art until 1998, when Forrest and Thompson reported the first use of iridium and platinum complexes to harvest triplet state excitons for phosphorescent emission. This breakthrough allowed the industry to realize 100% internal quantum efficiency (IQE) and paved the way for the development of highly efficient OLEDs [19]. Since their report, a wide variety of iridium and platinum based emitters have been developed that produce EQE's over 25% for blue-, green- and red-emitting doped structures, with both vacuum and solution processed techniques [20-22].

These state-of-the-art OLED structures are multi-layer organic heterostructures [23]. Each material/layer is chosen to reduce the energetic barrier between the electrodes and the recombination zone, and also improve carrier balance in the device. This design phase is critical in developing high efficiency devices with low voltage operations. In general, these layers consist of injection and transport layers. Hole-injection and electron-injection layers (HIL and EIL, respectively) are used to modify the work function of the adjacent electrode to improve injection of holes and electrons into the organic layers. Hole-transporting and electron-transporting layers (HTL and ETL, respectively) aid in the transport of holes and electrons into the emissive layer (EML) of the device. The EML, or host, material is carefully chosen to promote efficient formation and radiative relaxation of excitons for light emission [24]. Because phosphorescent emitters are doped in this host material, careful consideration must be made to the triplet energies of both materials to ensure an efficient exothermic energy transfer between the two triplet states [25, 26].

In order to realize high EQE devices, the host material must have several key properties. (1) It must have a larger triplet energy than the dopant material. This becomes difficult for blue dopants, where triplet energies greater than 2.75 eV are necessary [26-28]. (2) It must have suitable energy levels to match the cathode and anode for efficient charge injection. (3) It must ensure a balanced charge distribution across the EML. Charge balance is critical because charge accumulation at the interface leads and to exciton quenching and maximizes the exciton formation zone across the EML, while also reducing device efficiency roll-off [28]. Ambipolar host materials are materials that have similar hole and electron mobility values, thus promoting carrier balance and recombination in the EML. The design and development of new ambipolar materials is very important for improving device performance [26, 29].

1.3.1 OLED Classifications

OLEDs can be fabricated in a variety of architectures and designed to emit light in various directions. The given design choices relate a given classification. The most common way to classify an OLED is based on the location of its electrodes. Figure 1.8a and 1.8b illustrate so-called conventional and inverted OLED geometries, respectively. Conventional OLEDs have a bottom anode in contact with the substrate and a top contact on the opposite side of the device. Conversely, inverted OLEDs have a bottom cathode

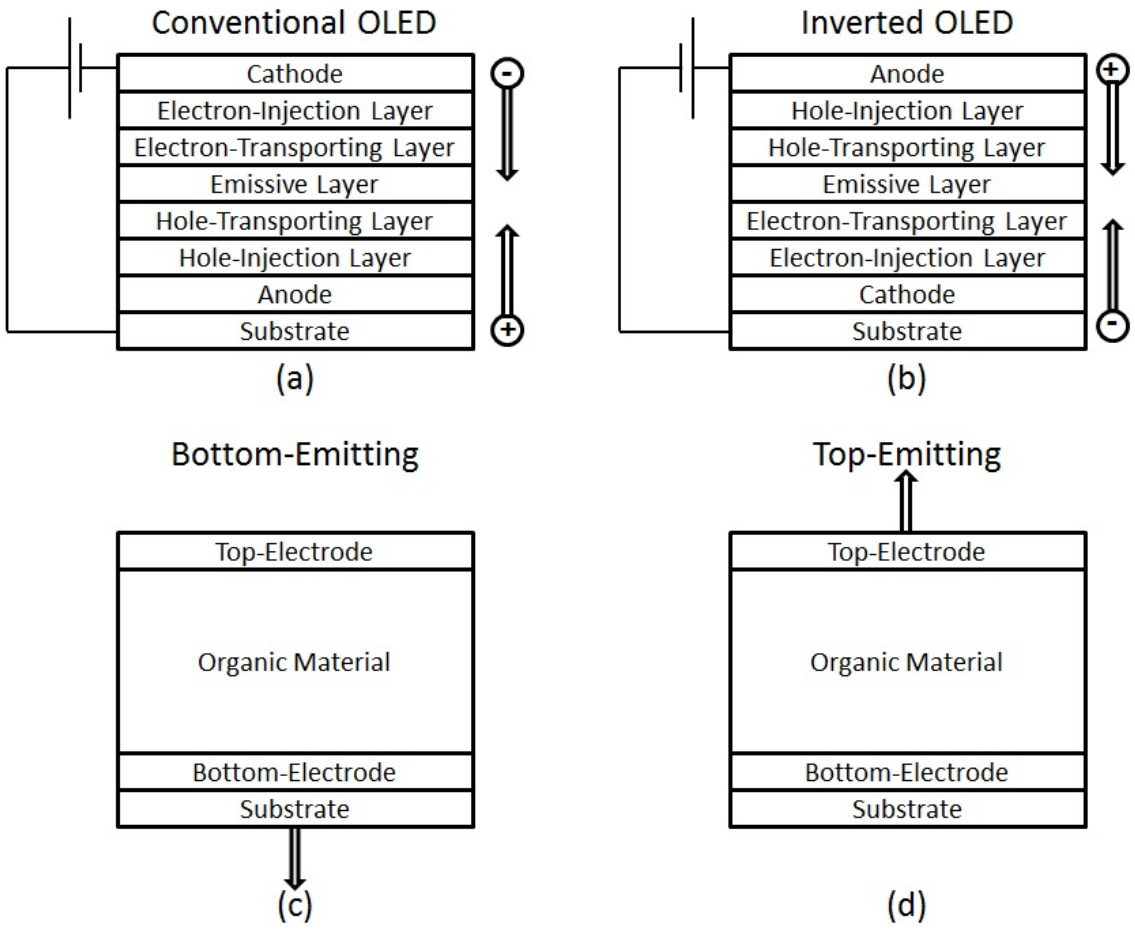

Figure 1.8 OLED classifications. (a) Conventional OLED structure. (b) Inverted OLED structure. (c) Bottom-emitting OLED. (d) Top-Emitting OLED

and top anode. Because of this difference, the constituting organic layers between the electrodes must also be reversed to allow for efficient carrier injection into the EML. The generated light can then escape either through the bottom of the substrate (bottom-emitting), or through the top layer of the device (top-emitting), as shown in Figures 1.8c and 1.8d, respectively. In both cases, a semi-transparent electrode is required for the light to escape the device.

Top-emitting OLEDs offer many inherent advantages over conventional bottom-emitting OLEDs. One of the major loss mechanisms in conventional OLEDs is wave-

guiding loses through the substrate [30, 31]. With top-emitting OLEDs, the light escapes through the top of the device and eliminates all loses resulting for total internal reflection (TIR) between the bottom electrode and substrates. Out-coupling layers can easily be deposited directly on top of the device to enhance the amount of light escaping the device [32-34]. Second, the ability to vacuum deposit metals as the bottom electrode allows designers the ability to use a wide array of substrates, including glass, flexible plastic, foils, or even paper, to create flexible, or even wearable, electronic devices [20, 35-37]. Third, top-emitting OLEDs can be easily integrated into the n-type transistor circuitry used to drive the active matrix displays while preserving the aperture ratio of the pixel [38].

While there are many advantages to OLEDs, there are also many disadvantages. The high efficiency phosphorescent dopants used in state-of-the-art devices are expensive and blue-emitting dopants are unstable at high current densities [39]. Conventional, bottom-emitting architectures use expensive and brittle indium tin oxide (ITO) as the bottom anode and require high temperature sputtering techniques for its deposition [20]. The current state-of-the-art inverted top-emitting geometries, while efficient and ITO free, use materials with low glass transitions temperatures (T_g) that reduce their overall stability and performance [26].

1.3.2 Blue-Emitting OLEDs

The first multi-layer blue-emitting OLED was fabricated by Adachi et al in 1990. This fluorescent device achieved a max luminance of 700 cd/m^2 and a power efficacy of 0.22 lm/W at a bias of 10 V [40]. The first phosphorescent blue OLED was demonstrated by Adachi et al in 2001 and yielded a max EQE of 5.7% and a power efficacy of 6.3 lm/W [25]. While this represented a significant improvement over fluorescent OLED

efficiencies, these devices relied on endothermic energy transfer between the dopant iridium(III)bi[(4,6-di-fluorophenyl)-pyridinato-N,$C^{2'}$]picolinate (FIrpic) and host 4,4'-bis(N-carbazolyl)-1,1'-biphenyl (CBP). By switching the host material to N,N'-dicarbazolyl-3,5-benzene (mCP), which has a higher triplet energy than FIrpic, the EQE and power efficacies of these devices improved to 7.5% and 8.9 lm/W, respectively [41]. Highly efficient phosphorescent blue-emitting OLEDs have proven to be much more difficult than their green- and red-emitting counterparts for two reasons. (1) The blue-emitting phosphors used in these devices have a high triplet energy and requires host materials with larger triplet levels for efficient, exothermic energy transfer between the two materials. (2) These phosphors are hard to synthesize and are unstable under high bias, leading to poor lifetimes [29]. Both of these issues with blue-emitting devices lead to very high device roll-off and affect efficiency measurements at high current densities. Lee et al. showed that these blue phosphorescent OLEDs were very sensitive to the properties of the hole transporting materials used in the stack. HTLs with high triplet energies and high hole motility values have yielded more efficient devices with less roll-off [42]. By employing these device design strategies, the currents state-of-the-art for blue OLEDs has exceeded 25% EQE and a 48 lm/W power efficacy [43]. However, phosphor lifetime continues to be a problem, as well as finding suitable host materials, and the current state-of-the-art device architecture requires a complex tri-layer EML with several different host materials used to maximize carrier injection and recombination.

1.3.3 Green-Emitting OLEDs

Because of the favorable energetic alignment between these green-emitting phosphors and host materials, green-emitting OLEDs have often defined the state-of-the-

art in OLEDs [20]. While CBP does not perform well as a host for blue-emitting materials, it works exceptional well with green-emitting dopants. In the first report of green phosphorescent OLEDs in 1999, Baldo et al showed that tris(2-phenylpyridine)iridium(III) ($Ir(ppy)_3$) doped in CBP at a 6% concentration can produce OLEDs with an EQE of 8% and power efficacy of 31 lm/W [44]. Since then, much work has been done to improve the performance and stability of these devices by exploring new phosphors, charge transport materials and device design strategies. In 2011, Wang et al. reported green-emitting OLEDs that produced an EQE of 29.2%. This structure used the horizontally oriented green phosphor bis(2-phenylpyridine) (acetylacetonate)iridium(III) ($Ir(ppy)_2(acac)$) doped in a CBP matrix as the EML and the electron transporting material 2,2',2" -(1,3,5-benzinetriyl)-tris(1- phenyl-1-H-benzimidazole) (TPBi) as the ETL. The bottom anode in this device was chemically modified with chlorine to increase the work function of the electrode and decrease the energetic barrier between it and the organic materials. When an out-coupling lens array was attached to the devices, they were able to reach efficiencies of 54% and produced a maximum power efficacy of 230 lm/W [20]. These devices remain the state-of-the-art for out-coupled OLEDs. In 2013, Kim et al. demonstrated green OLEDs with an EQE of 30.2% and power efficacy of 127.3 lm/W for a non out-coupled device, surpassing Wang et al. Their structure also utilized $Ir(ppy)_2(acac)$, but used a complex exiplex forming co-host system of [4,4′,4″-tri (*N*-carbazolyl) triphenylamine] (TCTA) and [bis-4,6-(3,5-di-3-pyridylphenyl)-2-methylpyrimidine] (B3PYMPM) [45].

1.3.4 Challenges of Phosphorescent Emitters

While phosphorescent emitters can provide 100% IQE and greater efficiencies, they also have many challenges. First is their cost. Phosphorescent emitters consist of

heavy metal iridium- or platinum- complexes that make them substantially more expensive (2-3x) to synthesize than conventional fluorescent emitters [39]. Second is their stability. There have been very few reports on blue-emitting phosphors with long lifetime and they suffer from significant efficient roll-off at higher current densities – the current state-of-the-art lifetime for blue-emitting OLEDS is 20,000 h [46]. Because of their high triplet energies, blue-emitting phosphors are less efficient at confining excitons in the emitting zone of the OLED and, consequently, show much steeper roll-offs at high applied biases compared to green- and red-emitting OLEDs [25, 26, 29]. This becomes an important issue for white OLED for display and lighting applications, where blue-emitting OLEDs degrade much quicker than green- and red-emitting counterparts and cause image distortions [9, 28, 47]. To circumvent this problem, manufacturers have adopted hybrid white displays that use fluorescent blue-emitting OLEDs with phosphorescent green and red OLEDs [9]. Third is their design. One of the key factors contributing to the efficiency of phosphorescent OLEDs is energy transfer from the host to the guest. An ideal host should have a triplet energy higher than that of the guest, and preferably greater than 2.9 eV so that it can be used for all dopants [29]. Reports of universal host materials with high triplet energies greater than 3.0 eV and ambipolar carrier mobility's have been scarce, but are crucial for the development of efficient and stable OLEDs [26, 48] .

1.3.5 Thermally Activated Delayed Fluorescence Based OLEDs

In 2012, Adachi et al. were able to show highly efficient OLEDs from thermally activated delayed fluorescence (TADF) [39]. This approach utilizes emitter molecules with a small energy difference between their singlet and triplet states (< 0.1 eV) to achieve TADF. Like fluorescent emitters, emission arises from the singlet state. However, unlike

fluorescent emitters, TADF emitters are able to achieve 100% IQE and harvest triplet excitons by reverse intersystem crossing (RISC) through thermal activation. This method has allowed for a new class of heavy-metal free fluorescent emitters to be developed with phosphorescent level efficiencies. Their initial work provided the synthesis details for the TADF emitter (4s,6s)-2,4,5,6-tetra(9H-carbazol-9-yl)isophthalonitrile (4CzIPN), which has become the benchmark green TADF emitter. In their paper, they produced OLEDs with a maximum EQE of 19.3% when doped in a CBP host matrix at a 1 wt. % concentration. However, recent work has shown that the efficiencies of these devices can be even further improved with the use of ambipolar host materials, and TADF devices with EQEs over 25% have been reported [49-52]. In 2014, Zhang et al synthesized a blue-emitting TADF compound, bis[4-(9,9-dimethyl-9,10-dihydroacridine) phenyl]sulphone (DMAC-DPS), which produced a maximum EQE of 19.5% [53]. This remains the state-of-the-art for blue TADF devices. As with phosphorescent blue-emitting OLEDS, efficiency roll-off at high current densities remains a concern with TADF emitters and is an area of increasing research.

1.3.6 OLEDs on Flexible Substrates

The manufacturing capabilities of OLEDs allow them to be fabricated on a wide-variety of substrates. OLEDs have been demonstrated on polyethylene terephthalate (PET), polyethersulfone (PES), nano-cellulose and flexible glass, and with good efficiencies [20, 35-37]. Han et al. reported flexible green OLEDs on PET with a graphene anode that produced a power efficacy of 102.7 lm/W. His structure, however, was very complex and involved tri-doped transport and emissive layers and used unstable materials [54]. Recently, members from our group were able to demonstrate highly efficient inverted top-

emitting OLEDs based on an aluminum/lithium fluoride (Al/LiF) bottom cathode. These devices, when assembled in a stacked sequence, produced current efficacies over 200 cd/A at 1000 cd/m^2, and were demonstrated on PES and flexible glass substrates [35]. This device architecture eliminates the need for an ITO bottom cathode and instead uses a vacuum deposited Al/LiF bottom cathode and semi-transparent gold (Au) top anode, which allows for easy vacuum deposited fabrication on flexible substrates.

1.4 OLED Challenges

While OLEDs offer many advantages over competing technologies, there are still many challenges that they must overcome before they can further increase their market share in the display and solid-state lighting industries. Significant progress needs to be achieved in large scale manufacturing, device encapsulation and operation lifetime. One interesting but undesired feature of OLEDs is that their efficiency decreases as the applied current increases. This is often referred to as 'efficiency roll-off'. Although inorganic LEDs experience similar roll-offs, their on-set current density for roll-off is much higher (> 10 A/cm^2) than for OLEDs (~ 0.1 A/cm^2) [55]. This deficiency can be compensated with a large area emissive region, which is difficult to fabricate with inorganic LEDs, and optimized device structures/cost-effective out-coupling techniques.

Manufacturing efficiency/yield is very closely related to invested resources and infrastructure. Currently, OLED manufacturing techniques are in their infancy and very expensive. This is especially true for large-area displays, where large glass substrates are required for back-plane patterning and OLED deposition [2]. Because of the size, it only takes several bad OLED pixels per sheet to cut the yield in half for large area displays. In

the future, improvements are needed in the manufacturing process, and the process needs to be scalable to large generation substrates. Most importantly, the industry needs to focus its resources and collectively work together if they want OLED technology to become the industry standard for display and solid-state lighting. The best way for technological standardization is industry wide collaboration.

In order to ensure OLEDs work as designed, encapsulation layers are needed to prevent small quantities of atmospheric moisture and oxygen from oxidizing the materials in the OLED [56]. Without a proper encapsulation layer, water will permeate through a thin-film barrier by four modes: micro-cracks, contaminant particles, along interfaces and through the bulk of the material. These mechanisms have been shown to reduce the operational lifetime of an OLED by as much as 99%. To prevent this quick degradation, a encapsulation (barrier) coating with a maximum water vapor transmission rate (WVTR) of 10^{-6} g m^{-2} day^{-1} is necessary [57]. The barrier coating for rigid applications has traditionally been a layer of glass sealed with epoxy [58], but this issue becomes more complex with flexible substrates. To accommodate these new form factors, active research has focused on the development of thin film encapsulation (TFE) methods for OLEDs. However, this introduces a new set of challenges because the techniques used to deposit these materials require high temperature process steps, which could potentially damage or destroy the underlying OLED. Several types of encapsulation barriers have been developed using different materials and processes – these include: the Vitex encapsulation method in which polymer filler layers and inorganic barrier layers (such as Al_2O_3) are alternatively deposited in a multilayer stack, and low temperature plasma enhanced chemical vapor deposition (PECVD) barrier films [56]. These films are designed to decouple the defects of the

individual barrier layers to force the water molecules to follow a tortuous diffusion path through the multilayer structure before reaching the OLED.

One of the most essential properties of an OLED is its operation lifetime. OLEDs need to be designed and manufactured so that they can operate at sufficiently high luminance levels for extended periods of time (< 100,000 h) [59]. The brightness depends on the application, with solid-state lighting requiring a higher brightness than displays (see Table 1 in Chapter 3). Optimizing OLED lifetime is challenging because the root causes for OLED degradation are multifaceted. Both intrinsic (current density levels, temperature, materials, purity, device area etc.) and extrinsic (environmental conditions, moisture, trace amounts of oxygen etc.) conditions can contribute to the stability of the device and its operational lifetime [60] [61-63]. Despite the levels of complexity, significant progress has been made in increasing the lifetime of OLEDs. In their seminal work, Tang and Van Slyke demonstrated an OLED with an operational lifetime of 100 h at an initial luminance of 50 cd/m^2. Since then, there has been significant progress in OLED stability using phosphorescent emitters. Universal Display Corporation (UDC) has demonstrated red-emitting OLEDs which take an estimated 900,000 h to decrease from 1,000 cd/m^2 to 500 cd/m^2 (so-called half-life), and green-emitting OLEDs which take an estimated 400,000 h [2]. However, OLEDs containing blue-emitting phosphors have not had similar success and pose a major challenge for OLED research. Their long excited state lifetime and high triplet energies make operationally stable blue OLEDs a challenge. Currently, the longest-lived blue OLEDs demonstrated by UDC have only a 20,000 half-life [2]. This represents a significant obstacle that the OLED community must solve in order for OLED technology to become the dominant technology in displays and solid-state lighting.

1.5 Thesis Organization

The work presented in this thesis aims to address three major concerns with OLED technology: engineering simplified device structures for high performance OLEDs, high performance OLEDs with heavy-metal free emitters, and OLEDs for flexible and wearable electronics. To provide the reader with the necessary background information, Chapter 2 will review the basics of organic semiconductor physics and organic light-emitting diodes. Chapter 3 will then introduce the reader to various radiometric and photometric quantities used to characterize OLEDs, as well as highlight the device fabrication and characterization process. In Chapter 4, high-performance electrophosphorescent OLEDs are demonstrated using a simplified device structure that utilizes a novel ambipolar host material and polymeric hole transporting material for both blue- and green-emitting dopants. Chapter 5 extends this work and demonstrates the ability for these novel materials to be used for high-performance blue- and green-emitting OLEDs from TADF, with reduced roll-off. Lastly, in Chapter 6 these materials are used to demonstrate a high-performance OLED on shape memory polymer (SMP) substrates for flexible and wearable electronics. Chapter 7 will summarize our work and discuss future work

CHAPTER 2

Physics of Organic Semiconductors

The physical mechanisms beneath organic semiconductors are complex and loosely understood, compared to their inorganic counterparts. The goal of this chapter is to provide the reader with the necessary background in organic semiconductor physics to help facilitate the discussions in the proceeding chapters. To achieve this, this chapter will be divided into four key sections. Section 1 will provide an overview of the general features of organic semiconductors and their processing techniques. Section 2 will discuss the electrical properties of these materials and include discussions on charge injection, charge transport and recombination. Section 3 will then introduce the reader to the photo-physics of organic semiconductors and explain exciton formation, energy transfer and emission. Lastly, Section 4 will briefly highlight the main loss mechanisms that influence OLED efficiency.

2.1 Introduction to Organic Semiconductors

The building blocks of organic semiconductors are carbon-containing small molecules or polymers, which are bonded through weak van der Waals forces. Small molecules are materials that have a very well defined molecular structure and weight, usually less than 1,000, which allows them to be easily evaporable. Polymeric materials, on the other hand, consist of varying-length chains of repeating molecular units without a definite molecular weight [64]. Because of this, polymer materials are too heavy to thermally evaporate and are typically deposited through solution processed techniques. The work presented in this thesis deals with both small molecules and polymer materials.

Many of the unique properties of organic semiconductors can be traced back to the weak intermolecular bonding. These weak Van der Waals interactions are a stark contrast to those associated with inorganic semiconductors, which utilize strong covalent bonds to form ordered crystalline structures [65]. Because of the weak molecular interactions present in organic semiconductors, structures can be engineered without regard for matching the lattice of the substrate, which allows for the use of cheap glass, plastic, foils and paper substrates with low temperature depositions [20]. Moreover, organic semiconductors have the unique ability to form amorphous structures, which allow them to form bonds that have a random distribution and orientation. Figure 2.1 provides a structural comparison between crystalline silicon and the amorphous small molecule tris(8-hydroxyquinoline)aluminum (Alq_3). These structural properties provide organic semiconductors with a unique set of mechanical, electrical and optical properties compared to inorganic semiconductor materials.

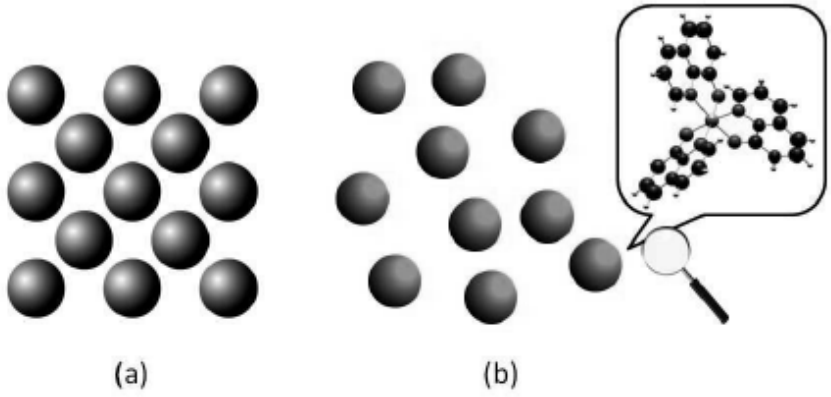

Figure 2.1 Structure of (a) [100] view of crystalline silicon (b) Organic small molecule Alq_3 (inset shows full chemical structure of material). Figure taken from [65].

Due to their low bonding strength and amorphous structure, organic films have a low Young's modulus compared to Si (1 GPa vs. 180 GPa) [65]. This feature allows these organic films to be used for curved, flexible, foldable and stretchable electronic devices. They also possess much lower indices of refraction than Si (1.5-2 vs. 3.85), which allows them to be used for transparent electronic devices [66].

2.1.1 Material Purification

The purity of the organic material used for electronic devices is of critical importance and high purity levels are crucial for high performance devices. The presence of impurities can lead to both the formation of charge trapping states and excited state quenching centers that can significantly affect the performance of the overall device [64, 67]. Therefore, in order to produce high quality and highly reliable devices, it is necessary to remove these impurities from the organic material. An effective technique to purify and remove these impurities is gradient zone sublimation.

Gradient zone sublimation is widely used and accepted technique to purify small molecule materials. In this technique, the organic material that is to be purified is placed within a long quartz tube, that is then placed in a furnace with a temperature gradient. This quartz tube is divided into ten smaller tubes that act as sleeves to catch the purified material (see Figure 2.2). The tube is evacuated through its open end using a turbo pump to a pressure below 1×10^{-6} Torr and the three zone furnace is gradually ramped up, with the highest temperature zone near the end of the quartz tube near the organic material and the lowest temperature zone near the tube opening. As the temperature is increased, the organic material will begin to sublime and travel through the quartz tube, where it will begin to recrystallize along the sleeves in the tube, while the volatile impurities condense near the

tube opening [68]. This crystalized region contains pure material and is extracted for use. This purification process usually requires approximately one week, but has been shown to reduce the level of fractional impurities to as low as 10^{-4} [64].

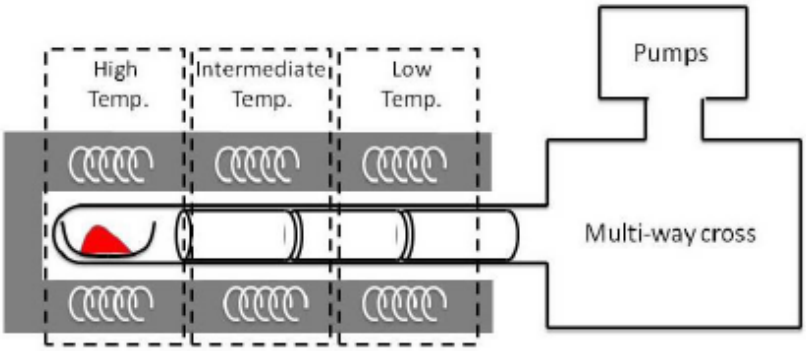

Figure 2.2 Setup for a gradient zone sublimation of organic materials

2.1.2 Vacuum Thermal Evaporation

There are a variety of deposition techniques available for organic films, including vacuum thermal evaporation (VTE), spin-cast, ink-jet printing, and organic vapor phase deposition (OVPD) etc. [64, 69, 70]. In this thesis, we will focus on VTE since the majority of the materials used in this work are small molecules and all of our devices were fabricated through VTE techniques (shown in Figure 2.3).

VTE is by far the most widely used organic film deposition technique for both research and large scale manufacturing. In this process, a source material is placed in a crucible and is loaded inside an electrically heated source. When current is applied across these sources, the temperature of the crucible increases and the material begins to evaporate. The rate of sublimation is monitored by quartz crystal microbalances that use the change in their resonant frequency to calculate the film thickness. These sensors allow

for a thickness control of approximately ± 0.5 nm [64]. This process is called 'Vacuum' Thermal Evaporation because this process requires an ultra-high vacuum level be maintained during evaporation; organic films are generally deposited under pressures < 1 x 10^{-7} Torr (the lower the vacuum, the better). The substrates that are to be patterned are suspended in the center of the chamber, several centimeters above the sources, and protected by a shutter until the desired deposition rate is achieved. Substrate rotation is typically enabled to achieve high film thickness uniformity. Patterning is achieved by the use of shadow masks in proximity to the substrates. This techniques allows for a minimum feature size of 20 μm to be achieved on the substrates.

A typical VTE system consists of 8 – 11 sources that allow for many different layers of various material to be deposited during a single system evaporation. Moreover, multiple organic sources can be co-evaporated simultaneously, with individual crystal monitors to control the rate and concentration of each material. This allows for a simple approach to

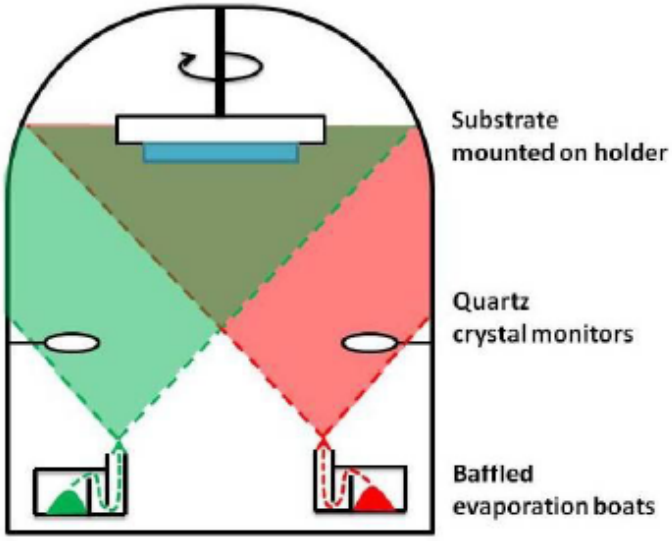

Figure 2.3 Set-up and operation of a vacuum thermal evaporation (VTE) system

dope individual layers during a deposition. Although this system is convenient and relatively simple to use, it does have many short-comings which make it a less than ideal solution for the future of organic film depositions.

The major short-coming of VTE is its poor material utilization efficiency (i.e. the amount of material deposited onto the substrates compared to that evaporated). Point-type sources (like those found in academic research labs) have less than a 5% material utilization rate [71]. In contrast, industrial VTE systems utilize line-type sources and have material utilization rates near 50%. All the unused material is deposited on the deposition system itself and is a cause of future contamination as these coated regions begin to flake and generate particles and, thus, defects in the device. In order to keep the system clean, it needs

to be exposed to oxygen and manually cleaned, which requires significant equipment downtime.

A new technology that has the ability to increase the material utilization efficiency and provide greater manufacturing flexibility is organic vapor phase deposition (OPVD), shown in Figure 2.4 [71]. In an OPVD system, organic material is evaporated into a hot carrier gas, which flows the gas through a path between two heated chamber walls to a cooled substrate. These heated walls prevent the material from depositing on them and, thus, substantially increases the material utilization efficiency of the process.

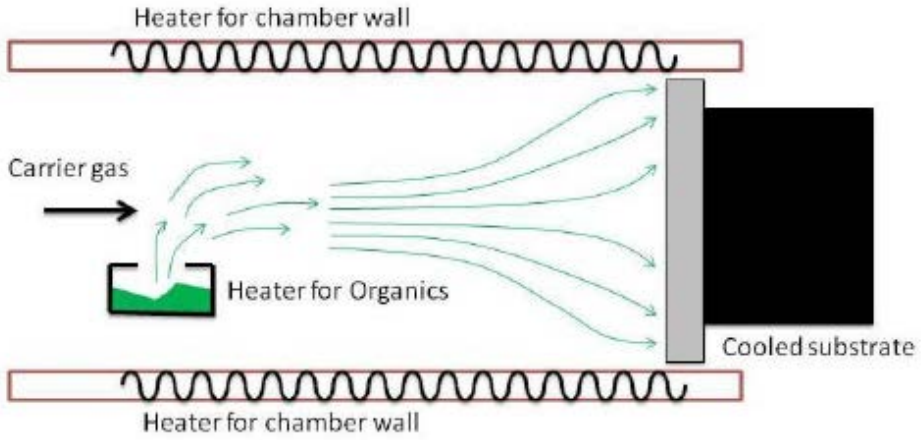

Figure 2.4 Set-up and operation of an organic vapor phase deposition (OPVD) system

2.1.3 Solution Processing

VTE techniques are only possible with small molecular materials. Polymeric materials with larger molecular weights are too heavy to evaporate and require alternative deposition strategies. There are many methods available for solution-based deposition, which include ink-jet printing, screen-printing, blade-coating, spin-coating etc. However, all the polymeric materials described in this thesis were processed via spin-coating

techniques. Spin-coating is accomplished by dissolving the source material is a liquid, dispensing the liquid onto the substrate and rapidly spinning the substrate to spread and coat it with the material. The final thickness of the film is dependent on a wide set of parameters, but is most strongly related to the solution concentration and spin-speed. Annealing the samples after spinning is necessary to remove any excess liquid from the film, or to alter its morphology. Compared to VTE, this process offers a number of processing advantages: it has a high material utilization ratio, it does not require a high vacuum and films can be easily created in seconds. However, issues arise when multi-layer solution-processed devices are created. Careful consideration needs to be made to ensure that top layers do not damage the underlying layers, or ruin the interface morphology. This places an inherent limitation on this process and the number of layers that can be deposited.

2.2 Electrical Properties of Organic Semiconductors

The unique electrical (and optical) properties of organic semiconductors arise because of the nature of carbon's atomic orbitals and the bonds that these carbon atoms form with other atoms. In order to understand the electrical properties of these materials, it is necessary to understand the intramolecular bonding within the molecules that form their molecular orbitals, which thus influence the molecules transport properties [72].

Within an organic semiconductor molecule, electrons in carbon atoms can form either strong covalent bonds – referred to as sigma (σ)-bonds – that result from head-on overlapping of two sp^2 hybridized orbitals, or weak covalent bonds – referred to as pi (π)-bonds – that result from off-plane p_z orbital overlap. sp^2 hybridization is achieved when a carbon atom bonds to three other atoms – the 2*s* orbital and two of the 2*p* orbitals (p_x and

p_y) bond to each other to form a sp^2 hybridized orbital [72]. After sp^2 hybridization, there remains a single un-hybridized p_z orbital, which is perpendicular to the sp^2 plane [73]. Each of these covalent bonds is represented as the linear superposition of the wave function of the electron associated with each interacting orbital. In the formalism of quantum mechanics, this behavior is represented by a wave function, ψ, which is a solution to the Schrödinger equation.

$$i\hbar \frac{\partial}{\partial t}\Psi = \hat{H}\Psi(\boldsymbol{r}, t), \tag{2.1}$$

In Eq. (2.1), i is the imaginary number, $\hbar$ is the reduced Planck's constant, and $\hat{H}$ is the Hamiltonian operator which is the sum of the potential and kinetic energy of the system [74]. Once the wave function is known, it can be used to determine the energy of the electron. The square of the wave function gives the probability of finding an electron at a certain position at a certain time. As an example, the simple ethylene molecule, C_2H_4, is shown in Figure 2.5.

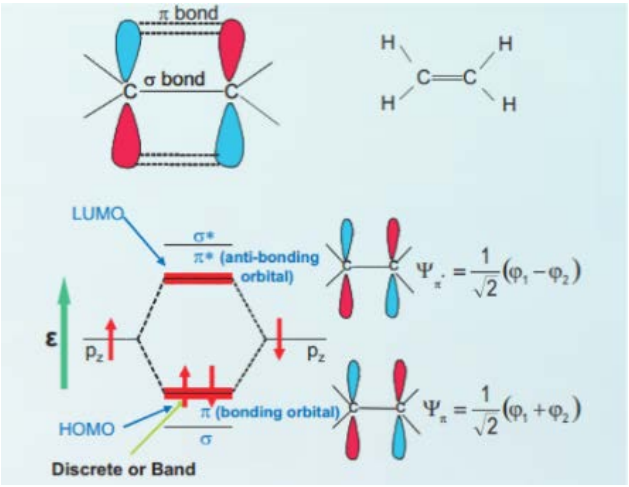

Figure 2.5 Graphical illustration of an ethylene molecule (C_2H_4) with σ- and a π-bond between the carbon atoms (top), and its corresponding frontier orbitals (bottom) Figure taken from [73].

The strength of these π-bonds is much weaker than the strength of the σ-bonds. Consequently, the electrons forming these π-bonds are less tightly bound and are more delocalized in space. Molecules of particular interest for organic semiconductors have a series of alternating single and double bonds and are said to be conjugated. This conjugation leads to delocalization of the electrons across the conjugated regions of the molecule and are largely responsible for the electronic and optical properties of organic semiconductor materials.

The π-bond between the two carbon atoms results from the linear superposition of the wave functions of two π-electrons in the p_z orbitals of each carbon atom, represented by $|\psi_n>$ and $|\psi_n^*>$, respectively, which leads to the formation of two states: a low energy state $\psi_\pi = \frac{1}{\sqrt{2}}(\varphi_1 + \varphi_2)$, where the probability of finding an electron between nuclei is very high – this is referred to as the bonding orbital; and a high energy state $\psi_{\pi^*} = \frac{1}{\sqrt{2}}(\varphi_1 - \varphi_2)$, where the probability of finding an electron between nuclei is low – this is referred to as the anti-bonding orbital [73]. These orbitals are commonly referred to as the highest occupied molecular orbital (HOMO) and lower unoccupied molecular orbital (LUMO) or a molecule, respectively.

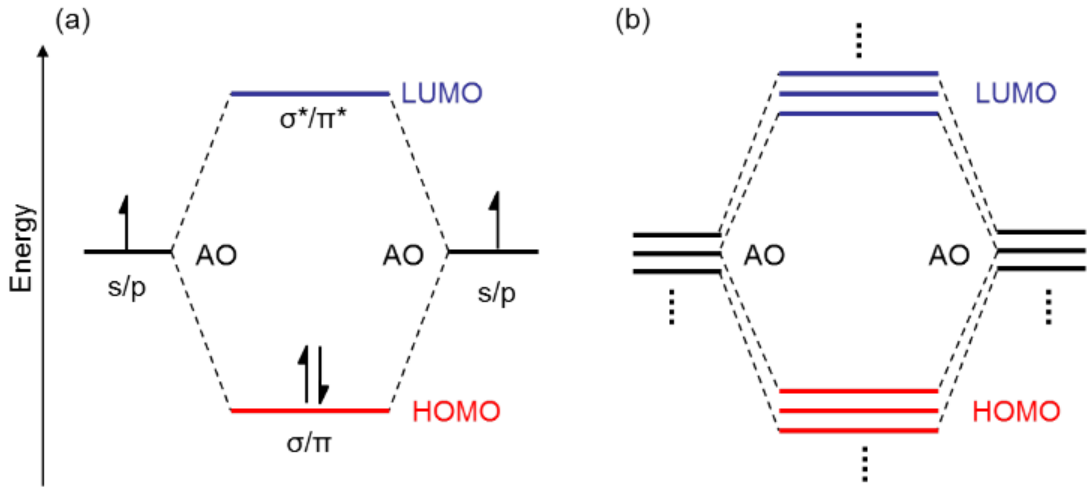

Figure 2.6 Bonding and anti-bonding molecular orbitals. Unpaired valence electrons fill the molecular orbitals according to the Aufbau and Pauli exclusion principles. (b) Many nearly-degenerate atomic orbitals combine within a molecule to create closely spaced molecular orbitals

Figure 2.6(a) graphically illustrates this interaction. The number of molecular orbitals equals that of the participating atomic orbitals. The spacing between these levels within the bonding and anti-bonding orbitals will decrease as the number of atoms increases [75] (see Figure 2.6(b)).

In the ground state configuration, the HOMO is filled with two electrons of opposite spin (in accordance with the Aufbau and Pauli exclusion principles), while the LUMO remains empty. Recall, the Pauli Exclusion Principle dictates that no two electrons can simultaneously occupy the same quantum state [72]. Thus, electrons can only occupy the same state if their spins are anti-parallel. The Aufbau principle dictates that electrons orbiting one or more atoms must fill the lowest available energy states before filling higher levels. This allows for the most stable electronic configuration.

These orbitals of the molecule correspond to one-electron wave-functions and can be calculated. But it is important to point out that what is measured experimentally upon excitation (or ionization) is the difference in energy between the *N*-electron ground state of the molecule and its *N*-electron excited state (or its $N \pm 1$-electron ionized state) [76].

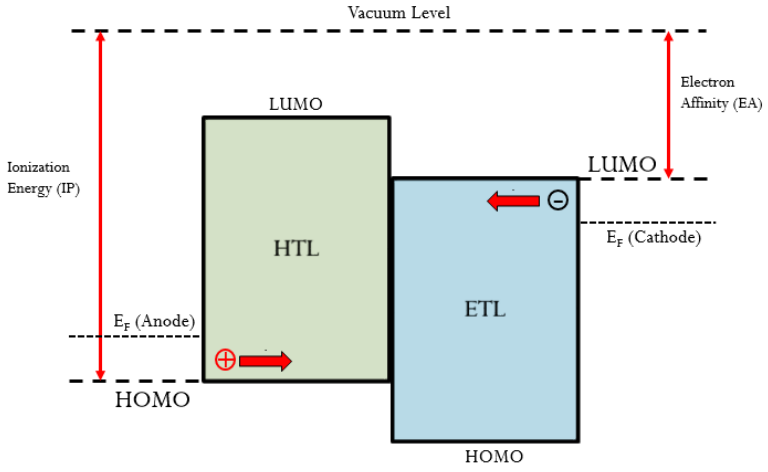

Figure 2.7 Energy level diagram of a simple OLED with two organic materials

For the purpose of these calculations, the HOMO is minus the energy of the ionization energy (IE), and the LUMO energy is minus the energy of the electron affinity (EA) of the molecule.

Figure 2.7 illustrates the HOMO/LUMO (IE/EA) energy levels for two common organic semiconductor materials (a hole-transport layer (HTL) and electron-transport layer (ETL)) in relation to a common vacuum level and the Fermi energies of an anode and cathode. As you can see from the figure, electrons are injected into the LUMO/EA level from the cathode, and holes are injected into the HOMO/IE from the anode. The physical operation of an OLED can be broken down into three key electrical steps: charge injection from the electrodes and charge transport across the organic materials towards the emissive

region of the device (EML), and charge recombination. A state-of-the-art OLED structure is a complex, multi-layer device that is designed to minimize the energetic barriers between HOMO/LUMO (IE/EA) levels while preserving equal charge balance in the emissive layer, as can be shown in Figure 2.8.

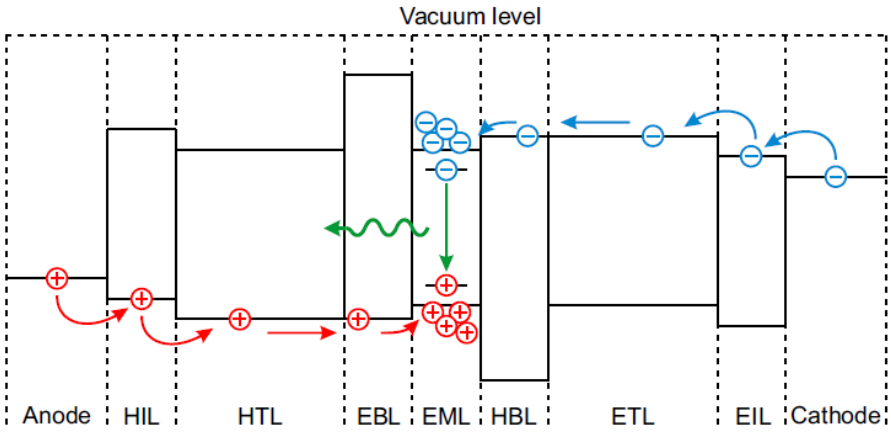

Figure 2.8 Energy level diagram of a multi-layer OLED

When the charges reach the EML of the device, the electrons and holes combine and become bound by the Coulomb force in excited states called excitons [77]. The excitons can then radiatively decay and release their energy through the emission of a photon. This is the light we see and measure from a OLED [23].

2.2.1 Charge Injection

Charge injection from the electrodes and into the organic semiconductors is a critical component for high-performance electronic devices. As shown in Figure 2.9, this process involves moving charges from the Fermi level of an electrode, E_F, to the frontier orbital of the organic material (in this diagram, charge is being injected into the LUMO

level). The electron injected from the cathode needs to overcome a built-in barrier height of $\Delta V = E_{LUMO} - E_F$. While this seems like a simple concept, it is actually quite a difficult process to describe.

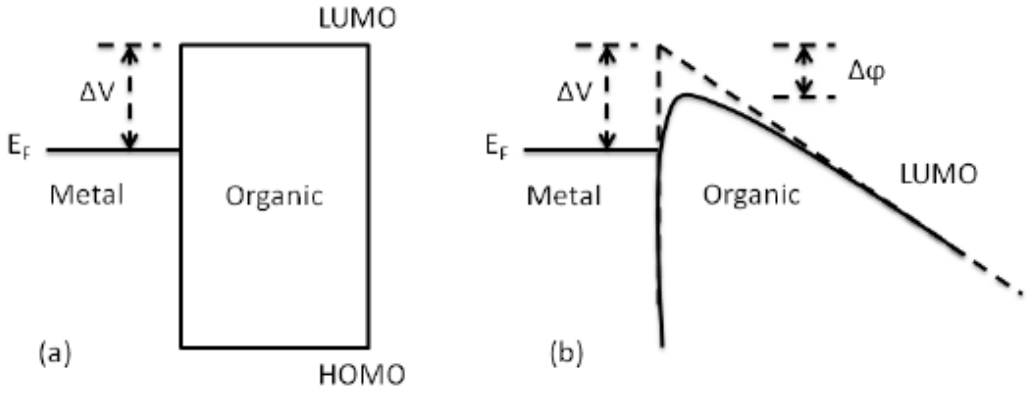

Figure 2.9 (a) Graphical illustration of the barrier height for current injection from a cathode to an organic material. (b) Barrier height reduction due to an interfacial electric field

Currently, there is no theory that completely describes this process because: 1.) these metal/organic interfaces are far from ideal and are strongly dependent on the surface chemistry, structure, disorder and morphology of the organic material; and 2.) it is difficult to determine the energy barrier between the metal electrode and organic material due to the presence of interfacial dipoles that can introduce energy level shifts and vacuum level offsets [78].

Despite these challenges, a common strategy that is often used to model this behavior is to assume this process to be analogous to the injection from a metal/inorganic Shockley contact in thermionic emission [78]. The expression for injected current from a Shockley diode in thermionic emission is given by:

$$J = A^{*}T^{2}e^{\left(\frac{-\Delta V}{kT}\right)}\left(e^{\left(\frac{eV}{nkT}\right)} - 1\right) \tag{2.2}$$

where A^* is the effective Richardson constant, ΔV is the height of the barrier to injection e is the elementary charge, V is the voltage across the diode, n is the ideality factor, k is the Boltzmann constant, and T is the temperature of the junction.

Emtage et al. added to this thermionic emission model by deriving expressions relevant to insulators (organic semiconductors) with low charge mobility, which simplifies to the following expressions when under a low electric field (Eq. (2.3)) and high electric field (Eq. (2.4)) [79]

$$J_{low} = N_e \cdot \mu \cdot e^{\left(\frac{-\Delta V}{kT}\right)}eF \tag{2.3}$$

$$J_{high} = N_e \cdot \mu \cdot (4eF^3\epsilon)^{1/4} \cdot \sqrt{\frac{k_B T}{\pi}} \cdot e^{\left(\frac{-\Delta V + \Delta\varphi}{k_B T}\right)} \tag{2.4}$$

Where N_e is the electron density of states, μ is the mobility, F is the electric field at the metal/organic interface, ε is the dielectric constant of the organic semiconductor and $\Delta\varphi$ is the barrier height reduction due to the interface electric field.

Recent improvements to this thermionic emission model from Scott and Malliaras include an organic-to-metal interface recombination current in addition to the metal-to-organic injection current, which has been shown to help understand charge injection into OLEDs [80].

All the above mentioned models assume a diode is in thermionic emission, but it is worth noting that there is another strategy to model current injection in organic materials. The method described by Fowler and Nordheim assumes electrons tunnel through the injection barrier between the Fermi level of the cathode and organic material, and results directly from solving Schrödinger's equation for a triangular barrier:

$$J = AE^2 e^{\left(\frac{-4\sqrt{2m}\Delta V^{2/3}}{3\hbar qE}\right)} \tag{2.4}$$

where *A* is a tunneling pre-factor, *E* is the applied electric field, and *m* is the electron mass [81].

The main drawback of all these models is that none of them take into account the energetic disorder that is present in organic semiconductor materials. These models all assume wave-like propagation of electrons through bands, not electron injection into localized states and charge transport via hopping between interfaces [82].

2.2.2 Charge Transport

Charge transport in disordered, amorphous organic materials proceeds by free charge carrier hopping between interacting molecules, or polymer chains. These hopping events are typically described by incoherent electron-transfer reactions that are strongly dependent on electronic coupling [83]. When an organic molecule is charged, its configuration is distorted and energy is relaxed to a lower level than its molecular orbital energy. This newly formed quasi-particle is called a polaron. Free charge carriers in organic semiconductors are characterized by polarons, which are classified as small or large depending on the size of the lattice distortion introduced by a free charge carrier with respect to the lattice size [84]. Polarons in organic molecules are generally classified as small due to the short range of the electron-polaron coupling.

This process is understood to be an electron-transfer reaction between neighboring molecules, *A* and *B*, and is schematically represented by a reaction of the type

$$A + B^+ \rightarrow A^+ + B \tag{2.5}$$

The rate constant k_{ET} of the electron-transfer reaction can be described by Marcus theory as

$$k_{ET} = A_0 \exp\left[\frac{-\lambda}{4k_B T}\right] \tag{2.6}$$

where A_0 is a pre-factor related to the electron coupling between the donor *A* and acceptor *B*, and λ is the reorganization energy [61, 62]. The reorganization energy λ represents the energy that is necessary to transfer an electron from molecule A to molecule B, while the geometries of both molecules remains fixed since the electron-transfer process occurs in a much faster time frame than the molecules can relax into a geometry that is energetically most stable (see Figure 2.10) [85].

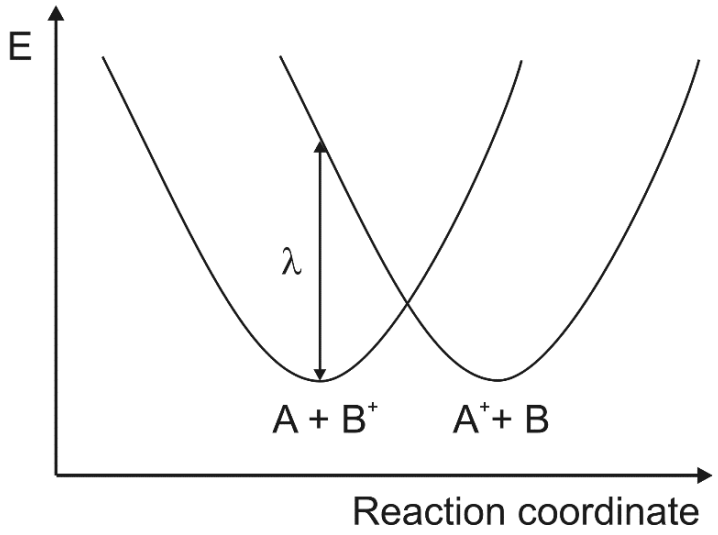

Figure 2.10 Representation of the reorganization energy λ for a hopping process according to Marcus Theory.

The earliest model used for charge transport in organic materials was the space-charge-limited-current (SCLC) model. In this model, the charge injection from the electrodes into the organic material is assumed to form an Ohmic contact, which allows for higher applied electric fields to inject more charges than can be transported in the material.

This causes the excess charges to build up in the material, and results in a non-constant electric field in the semiconductor. The derivation of the SCLC *J-V* behavior begins with Ohm's law and Gauss' law.

$$J = e\mu nE \tag{2.7}$$

$$\frac{dE}{dx} = \frac{e \cdot n}{\epsilon_r \cdot \epsilon_0} \tag{2.8}$$

where n is the electron density, ε_r is the relative permittivity of the insulator and ε_0 is the vacuum permittivity [82]. If we integrate Eq. (2.7) and insert it into Eq. (2.8), we obtain:

$$\int \frac{J}{\epsilon_r \cdot \epsilon_0} dx = \int E dE \rightarrow E = \sqrt{\frac{2xJ}{\epsilon_r \cdot \epsilon_0 \cdot \mu}} \tag{2.9}$$

Integrating Eq. (2.9) once more yields the Mott and Gurney SCLC *J-V* relation:

$$\int E dx = \int \sqrt{\frac{2xJ}{\epsilon_r \cdot \epsilon_0 \cdot \mu}} dx \rightarrow J_{SCLC} = \frac{9}{8} \frac{\epsilon_r \cdot \epsilon_0 \cdot \mu}{d^3} V^2 \tag{2.10}$$

If there are trap states present within the bandgap of the organic semiconductor material, a trap-charge limited current can be written. Assuming the trap states have an exponential distribution energy, $N_T(E)$, relative to the molecular orbital energies, the trap-charge limited current density is written as:

$$J = \frac{N_{eff} e\mu}{H^l} \left(\frac{\varepsilon_0 \varepsilon_r}{e} \frac{l}{l+1} \right)^l \left(\frac{2l+1}{l+1} \right)^{l+1} \frac{V^{l+1}}{L^{2l+1}} \tag{2.11}$$

where N_{eff} is the effective density of states in the transport band, H is the total concentration of traps, and $l = T_T / T$ is the characteristic distribution parameter (T_T is the trap distribution temperature) [86].

Compared to inorganic materials, the charge mobility in organic semiconductors is relatively low. For example, for amorphous Si used in thin-film transistors, the field-effect

mobility values range from 0.3-1 $cm^2\ V^{-1}\ s^{-1}$, for low-temperature poly-Si 10-200 $cm^2\ V^{-1}\ s^{-1}$, for high-temperature poly-Si 100-300 $cm^2\ V^{-1}\ s^{-1}$, and for crystalline silicon 400 $cm^2\ V^{-1}\ s^{-1}$ [8]. Highly pure, crystalline films of organic materials can have maximum field-effect mobility values that exceed that of amorphous-Si, such as 40 $cm^2\ V^{-1}\ s^{-1}$ for pentacene crystals [87], 15 $cm^2\ V^{-1}\ s^{-1}$ for rubrene crystals [88], and 4.9 $cm^2\ V^{-1}\ s^{-1}$ for crystalline films of C_{60} [89]. However, typical bulk conductivity values of disordered small-molecule and polymer films typically fall in the range of about $10^{-3} – 10^{-5}\ cm^2\ V^{-1}\ s^{-1}$ [64].

The understanding of charge mobility in organic semiconductors is much more complex than that in inorganic semiconductors, because the mobility is influenced by a large degree of factors, such as disorder, impurities, applied electric field strength, temperature and film morphology [90]. A formalism has been developed to account for the presence of this disorder in amorphous organic materials. Two main models have been used to calculate the hopping rate in the presence of static disorder, where electron-transfer reactions occur between nonequivalent hopping sites with energy ε_i and ε_j. These are the Miller-Abrahams model [91] and the Marcus model [92]. In both models, the hopping sites are assumed to be independent, with a hopping rate, k_{ij}, and assumed to be distributed following a Gaussian distribution density of states (DOS) with a standard deviation σ_{DOS}, from which potential hopping sites are randomly selected:

$$N_{c,v}(E) = \frac{N_1}{\sqrt{2\pi}\sigma_{DOS}{}^2} exp\left[-\frac{E^2}{2\sigma_{DOS}{}^2}\right] \equiv g(E) \tag{2.12}$$

where N_1 is the total DOS.

In the Miller-Abrahams formalism, the hopping rate k_{ij} is given by the form:

$$k_{ij} = \nu_0 exp(-2\gamma a \frac{\Delta R_{ij}}{a}) \begin{cases} exp\left(-\frac{\varepsilon_j - \varepsilon_i}{k_B T}\right); & \varepsilon_j > \varepsilon_i \\ 1 \quad ; & \varepsilon_j < \varepsilon_i \end{cases} \tag{2.13}$$

where v_0 is a pre-factor, γ is a factor representing the electronic wave function overlap, a is the lattice constant, ΔR_{ij} is the distance between transport sites i and j, and ε_i and ε_j are the energies of transport sites i and j [91]. In jumping from a site of lower to higher energy, the hopping rate decreases exponentially with the difference in electronic site energies. On the other hand, if the jump proceeds from a site of higher to lower energy, the last term in the expression is equal to unity.

With these assumptions, Monte Carlo simulations result in an expression for mobility given by

$$\mu = \mu_0 exp\left[-\left(\frac{2\hat{\sigma}}{3}\right)^2\right] exp\left[C(\hat{\sigma}^2 - \Sigma^2)E^{1/2}\right] \tag{2.14}$$

where μ_0 is a pre-factor, C is a constant empirically determined to have a value of 2.9×10^{-4} $cm^{1/2}$ $V^{-1/2}$, Σ is the width of the positional disorder, and $\hat{\sigma}$ is given by Eq. (2.25) [90].

$$\hat{\sigma} = \frac{\sigma}{k_B T}. \tag{2.25}$$

It is worth noting that this formalism was derived to describe charge hopping in crystalline materials with high trap densities. In crystals, charge transport typically occurs through highly delocalized modes in the conduction band but the presence of high concentrations of trapping sites leads to multiple charge trapping and de-trapping events that closely resemble a charge-hopping mechanism [93]. A more successful model to describe hopping in organic semiconductors is given by semi-classical electron-transfer rates provided by Marcus [92]:

$$k_{ij} = \frac{t^2}{h}\sqrt{\frac{\pi}{kT\lambda}}exp\left[-2\gamma\Delta R_{ij}\right]exp\left[-\frac{\left(\lambda+\varepsilon_j-\varepsilon_i\right)^2}{4\lambda kT}\right] \quad (2.16)$$

A main advantage of the Marcus model over the Miller-Abrahams theory is that in Marcus formalism, we do not see a monotonic increase in the hopping probability with increasing free-energy $|\Delta G^o| = |\varepsilon_j - \varepsilon_i|$. Instead, we see two different regime: a normal regime and an inverted regime. In the normal regime, $\lambda > |\Delta G^o|$ and the hopping rate increases with increasing $|\Delta G^o|$, until it reaches its max value when $\lambda = |\Delta G^o|$. In the inverted regime, $\lambda < |\Delta G^o|$ and the hoping rate decreases with increasing $|\Delta G^o|$ [94].

2.2.3 Charge Recombination

Once electrons and holes have been effectively injected into the organic materials and transported through the multi-layer device, charge recombination occurs. The recombination rate, *R*, in organic materials is generally modeled after the treatment by Langevin, which assumes that electrons and holes move towards each other under the influence of their mutual Coulomb interaction [95]

$$R = \frac{e\cdot\left(\mu_n+\mu_p\right)}{\varepsilon_o\varepsilon_r}np = k_L np \quad (2.37)$$

where $\mu_{n,p}$ are the electron and hole mobility values, respectively, and k_L is the Langevin recombination rate.

After electrons and holes recombine in the organic semiconductor material, the electron-hole pair forms an excited state, called an exciton [77]. These excitons play a critical role in the photo-physical properties of the organic semiconductor material.

2.3 Photo-physics of Organic Semiconductors

2.3.1 Singlet and Triplet Excited States

When organic molecules are excited, electrons from the HOMO level are excited to the LUMO level of molecule, leaving a hole in the HOMO level. The resulting electron-hole pair is bound together through Coulomb interactions to form an exciton. This excited state can be described by quantum mechanics [74].

Electrons are fermions with a spin angular momentum of $s = \pm\frac{1}{2}$. For convenience, we denote the spin of the individual electron states as either 'up' or 'down':

$$\begin{aligned} \langle\frac{1}{2}, +\frac{1}{2}\rangle &\equiv \langle\uparrow\rangle \\ \langle\frac{1}{2}, -\frac{1}{2}\rangle &\equiv \langle\downarrow\rangle \end{aligned} \tag{2.48}$$

Using this basis for a two-electron system, we obtain four combinations:

$$\uparrow\uparrow, \uparrow\downarrow, \downarrow\uparrow, \downarrow\downarrow$$

where the first and second arrows represent the spin states of the first and second electron, respectively. Of the possible combinations of the system, two spin states are possible in this two-electron system (*S = 0* (antisymmetric singlet state) and *S = 1* (symmetric triplet state)). The basis sets for the *S = 0* and *S = 1* states are shown in Eq. (2.19) and Eq. (2.20), respectively [74].

$$\langle 0,0\rangle = \frac{1}{\sqrt{2}}[\langle\uparrow\downarrow\rangle - \langle\downarrow\uparrow\rangle] \tag{2.59}$$

$$\langle 1,-1\rangle = \langle\downarrow\downarrow\rangle \tag{2.68}$$

$$\langle 1,0\rangle = \frac{1}{\sqrt{2}}[\langle\uparrow\downarrow\rangle + \langle\downarrow\uparrow\rangle]$$

$$\langle 1,+1\rangle = \langle\uparrow\uparrow\rangle$$

Of the four possible states of a two-electron system, three are in the triplet state and only one is in the singlet state (3:1 ratio). For the sake of completeness, it is worth noting that there are three types of excitons, depending on their spatial state. These are: Frenkel excitons, Charge-Transfer excitons and Wannier Mott excitons. The most common in organic semiconductors are Frenkel excitons, which are the most localized and have the higher binding energy (~ 1 eV) amongst the three [96].

2.3.2 Light Emission in Organic Semiconductors

These excitons are mobile excited states that have a finite lifetime. When they relax back down to their ground states, they release their excess energy in the form of photons (light) or heat. Depending on the guest material in an OLED matrix, light emission can arise from the S_1 singlet state or T_1 triplet state [19, 39]. The various decay pathways are illustrated in the Jablonski diagram shown in Figure 2.11.

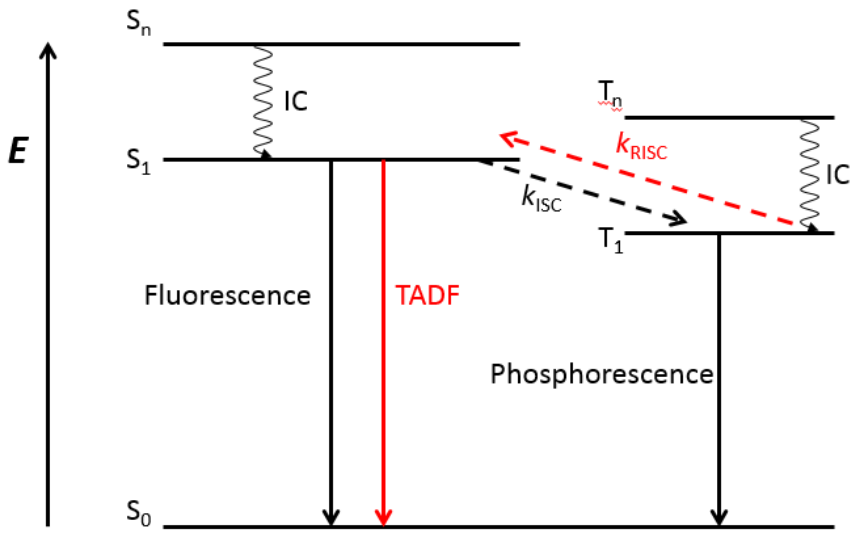

Figure 2.11 Jablonski diagram illustrating various excited state radiative decay pathways

2.3.2.1 Fluorescence

According to spin statics, 25% of all the excitons created in an organic semiconductor reside on the singlet state S_1 of the material. It is possible for excitons to reside on higher excited states (S_n/T_n), but they will transition to the lower state through internal conversion (IC) because radiative emission will is strongest when from the lowest excited state (S_1 or T_1) decaying to the ground state, S_0. Nonradiative (NR) relaxation of excitons is also possible but leads to the generation of heat.

Fluorescence is photon emission resulting from a singlet excited state radiatively decaying to S_0. In fluorescent materials, only singlet states can emit light; this is because the ground state is a singlet state, and the transition from triplets to singlets is forbidden due to the spin selection rules of quantum mechanics. This significantly affects the

efficiency of this process because only 25% of the total exciton population is under electrical excitation [31]. That means, at best, the internal quantum efficiency (IQE) for a fluorescence based devices is 25%. In order to increase this IQE, excitons from both the singlet S_1 and triplet T_1 states need to be harvested.

2.3.2.2 Phosphorescence

Baldo's seminal work that used heavy metal complexes induce spin-orbit coupling allowed for mixing of singlet and triplet states paved to way for high efficiency OLEDs [19]. This is accomplished by introducing a metal atom with a high orbital angular momentum into the molecule (generally Iridium or Platinum), which breaks the transition rules between singlet and triplet excitons and allows for singlet-to-triplet intersystem crossing (ISC) [44, 97]. Through ISC, all the excited excitons on the singlet state S_1 can transition to the triplet state T_1, where we now have 100% of all the excited excitons that can emit from T_1 to ground S_o. This process that can lead to an IQE of 100% is called phosphorescence. This discovery has paved the way for highly efficient OLEDs, but it is not without its limitations. While phosphorescent OLEDs have superior efficiencies to fluorescent devices, they suffer from significant efficiency degradation (henceforth referred to roll-off) at high applied biases, have poor operational lifetimes for blue-emitting materials and the heavy metal complexes used to induce the spin-orbit coupling contain rare earth metals, which make them expensive [28, 39, 98]. Until recently, phosphorescence was the only know way to achieve 100% IQE in organic semiconductors. But a recent discovery has shown that through clever material design and engineering, we can achieve 100% IQE from the fluorescence state through a process called thermally activated delayed fluorescence [51, 53, 99].

2.3.2.3 Thermally Activated Delayed Fluorescence

In thermally activated delayed fluorescence (TADF), triplet excitons are converted into the singlet excitons by a process called reverse intersystem crossing (RISC). RISC is made possible by a small gap in the singlet-triplet energy levels (ΔE_{ST}) of the molecule. If this energy gap is sufficiently small (< 0.1 eV), it allows for first-order mixing between the triplet and singlet states [39, 98, 99]. Now that all the excitons are on the singlet state S_1, we can obtain a 100% IQE from the $S_1 - S_o$ fluorescence state using heavy-metal free materials. This 100% IQE is the result of two different decay mechanisms: prompt fluorescence and delayed fluorescence.

In the prompt fluorescence mechanism, the emission occurs almost immediately (nanoseconds) after excitation with a decay from the $S_1 - S_o$ state. However, with delayed fluorescence, the singlet excitons created through RISC delays the illumination process and results in an increased fluorescence lifetime up to over 100 µs [98]. Although these mechanisms can be observed with two different fluorescence lifetimes, they have the same spectral distribution equal to the energy from the $S_1 - S_o$ state. The key to efficient TADF OLEDs is the harvesting of triplet excitons through RISC and designing emitters that have not only the necessary ΔE_{ST}, but also a stable T_1 state to allow for efficient RISC into S_1. This is vital to enhancing the fluorescence luminescence of the device. This discovery has led to a whole new area of research focusing on efficient TADF material design and device engineering and will be discussed in more detail in Chapter 5.

2.3.3 Energy Transfer Processes

Unlike basic fluorescence based device, phosphorescent and TADF emitters are doped at low concentrations (5% - 10%) in what is called a host material. This host material

acts a buffer layer between these dopants to maximize the performance of the device [44]. Excitons that are formed on the host can be transferred to the guest by both Förster [100] and Dexter [101] energy-transfer processes. The conductive host disperses the dopants to prevent undesirable quenching mechanisms, which have the ability to significantly impair the emission of light in the OLED device. However, we can ensure a high probability of radiative transitions by effectively selecting a suitable host material for a particular dopant to guarantee efficient energy transfer in these host-guest systems [25].

2.3.3.1 Förster Energy Transfer

The energy transfer from a donor to an acceptor via non-radiative dipole-dipole coupling is known as Förster transfer. This is called a 'long-range' process because it generally occurs at distances of up to 100 Å [19]. The probability of Förster energy transfer decays with R^{-6} , where R is the distance between the molecules (as shown in Eq. (2.19) [102])

$$E_{Förster} = \frac{1}{1 + \left(\frac{r}{R_0}\right)^6} \tag{2.19}$$

As a consequence of the pure dipole-dipole interaction, the total spin of each molecule has to be conserved during the energy transfer process. This means that triplet transfer from donor to acceptor is strictly forbidden in Förster transfer. The allowed mechanisms are:

$$\begin{aligned} D_S{}^* + A_S &\rightarrow D_S + A_S{}^* \\ D_S{}^* + A_T &\rightarrow D_S + A_T{}^* \end{aligned} \tag{2.20}$$

This process is illustrated in Figure 2.12.

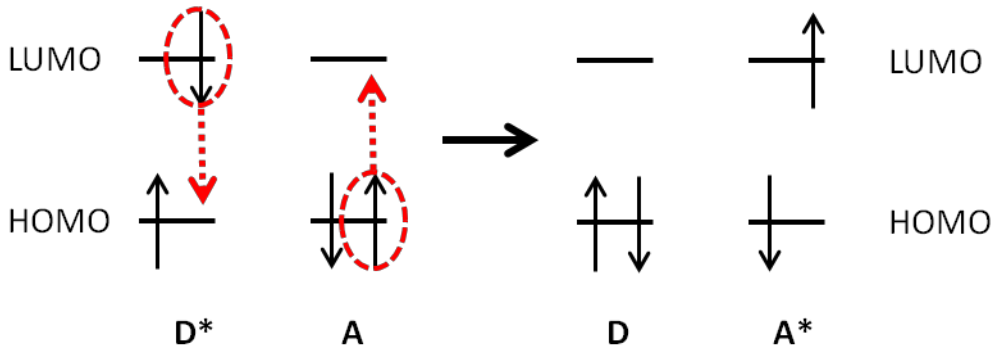

Figure 2.12 Graphical illustration of Förster energy transfer.

2.3.3.2 Dexter Energy Transfer

The energy transfer process between two neighboring molecules is called Dexter energy transfer. Dexter transfer requires an overlap of molecular orbitals, and thus typically occurs over shorter distances (10 Å) [102]. In this process, the total spin of both molecules needs to be conserved, which leads to the following allowed Dexter mechanisms:

$$D_S^* + A_S \rightarrow D_S + A_S^* \qquad D_T^* + A_S \rightarrow D_T + A_S^* \tag{2.21}$$

Unlike Förster transfer (which requires that the electrons remain confined to the same molecule), electrons are allowed to transfer between molecules in Dexter transfer, and Dexter transfer allows for both triplet-triplet and singlet-singlet energy transfer to occur between molecules [103]. A graphically illustration of Dexter transfer is shown in Figure 2.13. In order to design high efficiency OLEDS, it is important to choose host-guest systems with a host material that has a higher singlet and triplet energy level than the guest material. This will ensure an energy efficient, exothermic transfer of excitons from the host to guest material [25].

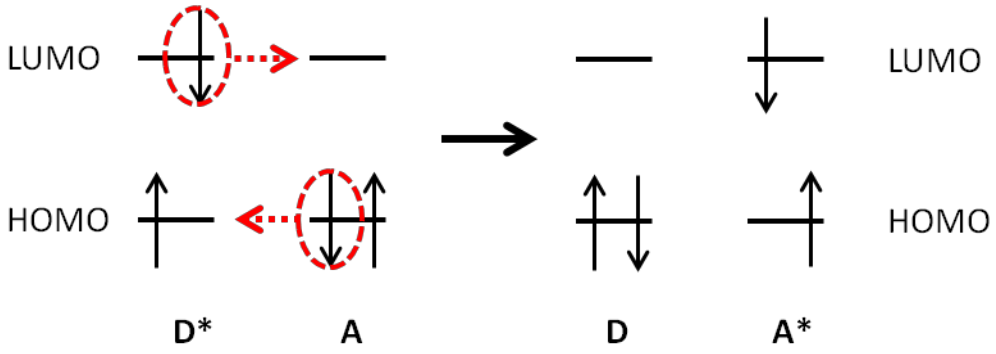

Figure 2.13 Graphical illustration of Dexter energy transfer

2.3.3.3 Exciton Quenching

Exciton interactions can also lead to exciton annihilation, where energy from an exciton is transferred to another excited state (generally an exciton or polaron) [77, 104, 105]. The annihilation of an exciton due to the interactions with other excited states is called quenching. It was worth noting that quenching can also occur through the present of defects and impurities in the film, but these issues can be quickly resolved through the use of gradient zone sublimation to purify the material [90]. Common exciton interactions in organic materials are: singlet-polaron annihilation (SPA), triplet-polaron annihilation (TPA), singlet-singlet annihilation (SSA), singlet-triplet annihilation (STA) and triplet-triplet annihilation (TTA) [104].

Quenching involving a singlet is dominated by Förster energy transfer because of the long-range dipole-dipole interaction. Triplet quenching, on the other hand, usually follows Dexter transfer mechanisms. SSA occurs through:

$$S_1 + S_1 \rightarrow S_0 + S_1 \tag{2.20}$$

This means that two excited singlets create one excited singlet and one singlet in the ground state. However, it is more common for singlet excitons to quench triplet excitons according to STA:

$$S_1 + T_1 \rightarrow S_0 + T_1 \tag{2.21}$$

Likewise, the interaction between two triplet excitons can lead to TTA and the following transfer mechanisms:

$$\begin{aligned} T_1 + T_1 &\rightarrow S_0 + T_1 \\ T_1 + T_1 &\rightarrow S_0 + S_1 \end{aligned} \tag{2.22}$$

In both TTA mechanisms, two excited triplets form a singlet in the ground state with either: an excited state triplet or excited state singlet, respectively. In both cases, these excited state excitons radiatively decay back down to the ground state. According to spin statistics, the first process that creates an excited triplet state is more likely to occur than the second [105].

Understanding these quenching mechanisms in an OLED, and which is dominant in a given device structure, is complex. Typically, a combination of several of these quenching processes can be observed in an OLED when driven at a high current density, and these are the primary cause for efficiency roll-off in OLEDs [28]. In order to design high efficiency OLEDs with long operational lifetimes, each of the transfer mechanisms needs to be suppressed.

2.3.4 OLED Efficiency

One of the most often reported figures of merit for an OLED is its external quantum efficiency (EQE). In its simplest form, EQE (η_{ext}) is simply the ratio between the number of photons emitted from the surface of the OLED to the number of injected electrons [31].

It can also be defined as the product of IQE η_{int} (the ratio between the number of photons emitted in the material to the number of injected electrons) times the out-coupling efficiency of the device η_{out}:

$$\eta_{ex} = \eta_{int} \cdot \eta_{out} \tag{2.23}$$

where η_{int} is dependent on the device architecture and the properties of the materials in the OLED:

$$\eta_{int} = \gamma \cdot \eta_{ST} \cdot q_{eff} \tag{2.24}$$

In this expression, γ represents the fraction of injected carriers that form excitons, η_{ST} is the fraction of spin-allowed excitons (also known as the singlet/triplet factor where η_{ST} = 0.25 for fluorescent emitters and η_{ST} = 1 for phosphorescent/TADF emitters) and q_{eff} is the effective radiative quantum efficiency of the emitting material [106].

Thus, in order to maximize the EQE of an OLED, Eq. (2.24) should be maximized. The charge carrier balance γ depends on the number of electrons and holes that are injected and transported in the device. If all these injected carriers recombine, then γ = 1. This can be achieved by effective device engineering to ensure charge balance in the emitting material of the device.

The fraction of spin-allowed excitons can be maximized through the use of host-guest systems that utilize guest molecules and energy transfer mechanisms to achieve 100% exciton harvesting. This has been shown possible with both heavy metal containing phosphors that emit from the triplet state, and TADF materials that emit from the singlet state.

The effective radiative quantum efficiency q_{eff} corresponds to the number of photons absorbed under photoluminescent (PL) excitation, and is defined as:

$$q = \frac{\Gamma_r}{\Gamma_r + \Gamma_{nr}} \tag{2.25}$$

where Γ_r is the radiative decay rate and Γ_{nr} is the sum of all competing non-radiative decay rates [30]. Thus, to maximize q_{eff} it is necessary to minimize Γ_{nr} to as close to zero as possible. However, due to the various layers with different optical properties that make-up an OLED, interference properties modify the radiative decay rate according to:

$$q = \frac{F \cdot \Gamma_r}{F \cdot \Gamma_r + \Gamma_{nr}} \tag{2.26}$$

where F describes the Purcell factor [107]. Consequently, the challenge to obtaining a $q_{eff} = 1$ now requires optimization of the OLED cavity to maximize the effects of the OLED cavity.

These three factors constitute the η_{int} of the device, but once the light is generated it needs to exit the device. The factor that describes this process is the outcoupling factor η_{out}, and it is a highly limiting factor for high-efficiency OLEDs [103]. The main issues with the η_{out} are due to the high index of refraction of the organic materials that cause total internal reflection (TIR) at the various material interfaces in the device, and TIR between the substrate and external medium [30]. This TIR leads to a significant portion of the emitted light getting trapped in either substrate emission modes (where emission is trapped within the substrate) or within waveguide modes (where the light is totally reflected at the interface between the substrate and the anode). However, these loses can be suppressed with creative device engineering and by employing out-coupling strategies to minimize the amount of light lost to TIR. Substrate emission modes have been shown to be effectively reduced by modification of the external interface to prevent TIR (i.e. roughening the

surface), through the addition of microlens arrays or nano-porous or micro-particle scattering films [103, 108].

CHAPTER 3

Performance Metrics and Experimental Procedures

In order to understand and measure the performance of an OLED, the research community has adopted a set of standardized performance metrics. These metrics allow for OLEDs fabricated in different laboratories across the world to be accurately evaluated and compared. In this chapter, the reader will be introduced to the main terms and metrics used to quantify the performance on an OLED. Additionally, the OLED fabrication and testing procedures used in our research group will be highlighted.

3.1 Performance Metrics

OLEDs are optoelectronic devices, which means that they can be evaluated both in terms of their electrical and optical characteristics. In order to fully quantify these OLED devices, a wide-variety of device characteristics are measured. The following subsections will provide a general overview of these terms and their definitions.

3.1.1 Luminance

Because OLEDs are generally designed for the human eye, the light output of these devices is measured in photometric units. Photometry differs from radiometry in that the light output is measured in candelas (instead of watts) and the response is weighed by the photopic sensitivity function, which is the response of the human eye under normal daylight conditions. The detection of light by the eye is a complex process. Light entering the eye is first transmitted through pre-retinal optics and ultimately received by the retina which contains two different types of eye receptors (rods and cones) [109]. Energy from the light is absorbed by the rods and cones and is converted into electrochemical signals

that are sent through the optical nerve to the brain. The rods are used for vision under low levels of illumination known as scotopic vision. The cones are used for photopic vision, or day vision, and are responsible for the perception of colors. The absorption spectra of the cones and the transmittance of the eye's pre-retinal optics cause the human eye to have varying degrees of sensitivity to the wavelengths of visible light (wavelengths ranging from 360 – 800 nm) [110].

In 1924, the Commission Internationale de l'Eclairage (CIE) described a standardized spectral response for the human eye which is known as the photopic response. The photopic response is often denoted *V(λ)* and is shown in Figure 3.1 [109]. As can be seen from this figure, the human eye is most sensitive to green light with a wavelength near 555 nm. The photopic response is used to convert radiometric quantities to eye response-weighted photometric equivalent quantities. Photometric quantities are usually denoted by the same symbols as radiometric quantities with an added subscript of '*v*' to indicate that they have been weighted against the photopic response function.

The term used to describe the radiated power from an OLED is luminance (L_v), and it is reported in candelas per square meter (cd/m^2). This term describes the amount of light that is emitted from an area of 1 m^2 per a given solid angle, and it is the metric that describes the subjective brightness of an object in photometry. Mathematically, luminance is defined as

$$L_{\mathrm{v}} = 683[\frac{lm}{W}] \int_{380}^{770} L(\lambda)V(\lambda)d\lambda. \qquad (3.1)$$

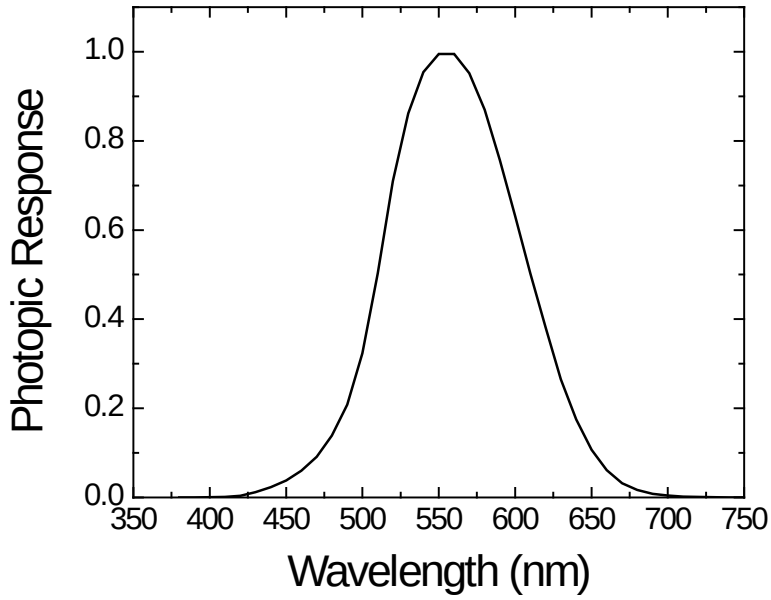

Figure 3.1 The photopic response of the human eye. Figure taken from [109].

where $L(\lambda)$ is the normalized spectrum of the OLED, $V(\lambda)$ is the photopic response and 683 is a normalization factor. For points of reference, typical luminance values for display technologies are presented in Table 1.

Table 1 Typical luminance values present in consumer electronic devices.

Device	**Luminance [cd/m^2]**	**Reference**
iPhone 6	560	[111]
iMac	450	[112]
Samsung 4K TV	1,000	[113]

It is crucial to accurately measure the luminance of a device because all the other performance metrics either utilize these values in their calculations, or for performance reference.

The luminance of an OLED is generally measured with a photodiode. The responsivity of the photodiode, $R_{det}(\lambda)$, is given by,

$$R_{det}(\lambda) = \frac{I_{det}(\lambda)}{\Phi_{det}(\lambda)} \tag{3.2}$$

where $I_{det}(\lambda)$ is the photocurrent produced by the detector and $\Phi_{det}(\lambda)$ is the power at a given wavelength impinging on the detector. A weighted detector responsivity can be derived by integrating the product of the wavelength-dependent detector response with the spectrum of a device under test, $S(\lambda)$:

$$R_{det} = \frac{\int_{380}^{780} R_{det}(\lambda)S(\lambda)d\lambda}{\int_{380}^{780} S(\lambda)d\lambda} = \frac{I_{det}}{\Phi_{det}} \tag{3.1}$$

where Φ_{det} and I_{det} are the total flux received by the detector and the total photocurrent produced by the detector, respectively. The current of the photodetector, I_{det}, can be derived from Ohm's law and is given by,

$$I_{det} = \frac{V_{det}}{R_f} \tag{3.4}$$

where V_{det} is the voltage produced at the output of the current-to-voltage converter and R_f (with a resistance of 5 MΩ) is the feedback resistor. A more detailed description of the OLED measurement set-up will be provided in section 3.3.

By combining these equations, the expression for radiance can be rewritten as:

$$L = \frac{I_{det}R^2}{R_{det}S_0A_0} = \frac{V_{det}R^2}{R_fR_{det}S_0A_0} \tag{3.5}$$

where R is the distance from the light source to the detector, A_0 is the area of the detector, and S_0 is the surface area of the light-emitting source. The luminance can then be obtained by converting the radiance to luminance using Eq. 3.1).

3.1.2 External Quantum Efficiency

EQE was introduced above in Section 2.4, and is defined as the ratio of the number of photons emitted in the forward direction of a device to the number of electrons injected into the diode. Mathematically, this can be defined as:

$$\eta_{EQE} = \frac{n_{ph}}{n_e} \times 100\% \tag{3.5}$$

where n_{ph} is the total number of photons emitted from the device into the forward hemisphere and n_e is the total number of electrons injected into the device. Thus, by effectively measuring n_{ph} we are able to experimentally determine η_{EQE}.

If we assume that the light source is a Lambertian emitter (that is, its radiance is independent of direction [109]), then the total number of emitted photons can be determined from the radiance measurement at the surface normal [114]. The definition of irradiance (E) for a Lambertian emitter gives:

$$E = \frac{d\Phi_{OLED}}{ds_0} = \pi L \tag{3.6}$$

where Φ_{OLED} represents the total flux emitted by the source. Solving for Φ_{OLED} and integrating over the source area yields:

$$\Phi_{OLED} = \pi L S_0 \tag{3.7}$$

Here, we can solve for L and substitute Eq. (3.7) into Eq. (3.4), to give:

$$\Phi_{OLED} = \frac{\pi V_{det} R^2}{R_f R_{det} A_0} \tag{3.8}$$

Now that we have a measureable relation for the total flux emitted by the source, we can measure n_{ph} through:

$$\eta_{ph} = \frac{\Phi_{OLED}}{hc} \frac{\int_{380}^{780} \lambda \times S(\lambda) d\lambda}{\int_{380}^{780} S(\lambda) d\lambda} \tag{3.9}$$

Lastly, we can easily determine the number of electrons injected into the OLED n_e by simply dividing the current by the charge of an electron q:

$$n_e = \frac{I}{q} \tag{3.10}$$

Thus, the total EQE of the OLED can be calculated according to Eq. (3.5):

$$\eta_{EQE} = \frac{\Phi_{OLED}}{hc} \frac{\int_{380}^{780} \lambda \times S(\lambda) d\lambda * q}{\int_{380}^{780} S(\lambda) d\lambda \ * I} \times 100\% \tag{3.11}$$

3.1.3 Current Efficacy

The current efficacy η_{CE} of a device is a widely used term in industry and academia, and it is given by the forward luminance L_v divided by the applied current density j:

$$\eta_{CE} = \frac{L_v}{J} \tag{3.12}$$

η_{CE} are generally expressed in units of mA/cm^2. This term is a valuable metric for defining light source performance because it relies on the luminance of the device, which is typically measured over a small solid angle in the direction of the surface normal, just as displays are typically viewed.

3.1.4 Luminous Efficacy

The luminous efficacy η_{LE} of a device is defined as the ratio between the emitted luminous flux Φ_v and radiant flux Φ:

$$\eta_{\mathrm{LE}} = \frac{\Phi_v}{\Phi}. \tag{3.13}$$

where Φ_v is weighted by the photopic response and given by:

$$\Phi_v = 683[\frac{lm}{W}] \int_{380}^{770} \Phi(\lambda)V(\lambda)d\lambda. \quad (3.14)$$

The quantity measures the effectiveness of a light source for producing visible light, and it is expressed in units of lumens per Watt (lm/W).

3.1.5 Power Efficacy

The power efficacy η_{PE} of a device is also expressed in units of lm/W, and it is the measure of the amount of light flux produced by a source at a given input power. It is expressed as:

$$\eta_{\mathrm{PE}} = \frac{\Phi_v}{\mathrm{P}} \quad (3.15)$$

where *P* is the input power in units of Watts. Table 2 highlights typical PE values for commercial light sources.

Table 2 Typical PE values present in consumer lighting sources (from [115]).

Type	**PE [lm/W]**
Incandescent Bulb	15
Halogen	20
Compact Fluorescent Lamp	73
Fluorescent Tube	108
LED Bulb	80-120
High-Intensity Discharge	105-115
OLED Luminaire	52

3.2 Colorimetry

3.2.1 CIE Spectral Coordinates

Thomas Young was the first to propose that the sensation of color is due to a mixture of responses of three 'particles' within the retina that are primarily sensitive to three principal colors [109]. Helmholtz further developed this ideal with color matching experiments and formed the basis of the trichromatic color vision theory. Our ability to distinguish color is a result of three different cone photoreceptor cell (short-, middle- and long-wavelength sensitive) [116]. The CIE 1931 Color System is a trichromatic system roughly based on the primary color stimuli of red, green, and blue [117]. Within the system, three primary color-matching functions denoted $\bar{x}(\lambda)$, $\bar{y}(\lambda)$, and $\bar{z}(\lambda)$, which are plotted in Figure 3.2, are used as weighting functions for a given color stimulus. The $\bar{y}(\lambda)$ is chosen to be exactly the normalized photopic response. The color of a stimulus can be uniquely characterized by the tristimulus values *X*, *Y*, and *Z*, which are obtained using the following definitions [109]:

$$X = \int_{380}^{780} S(\lambda)\bar{x}(\lambda)d\lambda \tag{3.16}$$

$$Y = \int_{380}^{780} S(\lambda)\bar{y}(\lambda)d\lambda \tag{3.17}$$

$$Z = \int_{380}^{780} S(\lambda)\bar{z}(\lambda)d\lambda. \tag{3.18}$$

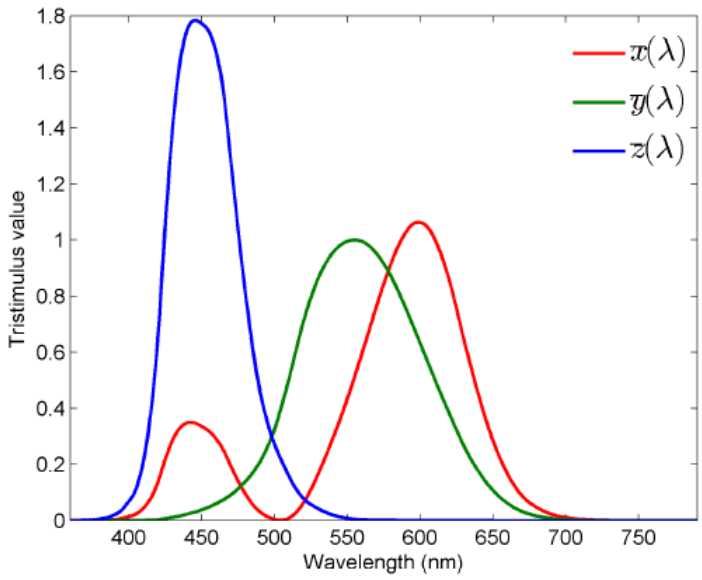

Figure 3.2 The three color-matching functions of the CIE 1931 color system

X, *Y*, and *Z* are the amounts of each primary color needed to match the color of a source. These define the CIE XYZ color space. We can normalize these tristimulus values to simplify the color analysis. The result defines the chromaticity coordinates (*x*, *y*, *z*) [116]:

$$x = \frac{X}{X + Y + Z} \tag{3.19}$$

$$y = \frac{Y}{X + Y + Z} \tag{3.20}$$

$$z = \frac{Z}{X + Y + Z}. \tag{3.21}$$

where

$$x + y + z = 1. \tag{3.22}$$

From Eq. (3.22), we can see that it is sufficient to specify only the (*x*, *y*) coordinates to uniquely identify any color. This specification is made with the chromaticity diagram, shown in Figure 3.3. This diagram illustrates all the colors perceptible by the human eye.

Pure colors of monochromatic light are located on the outer curve, and mixed colors (white) are located closer to the center.

In display applications, colors are achieved by additive mixing of the light that is emitted from red, green and blue (RGB) pixels. The CIE color coordinates for the RGB primary colors in CIE are (0.73, 0.27), (0.27, 0.72), and (0.17, 0.01), respectively, which corresponds to monochromatic light with a wavelength of 700 nm, 546.1 nm, and 435.8 nm, respectively.

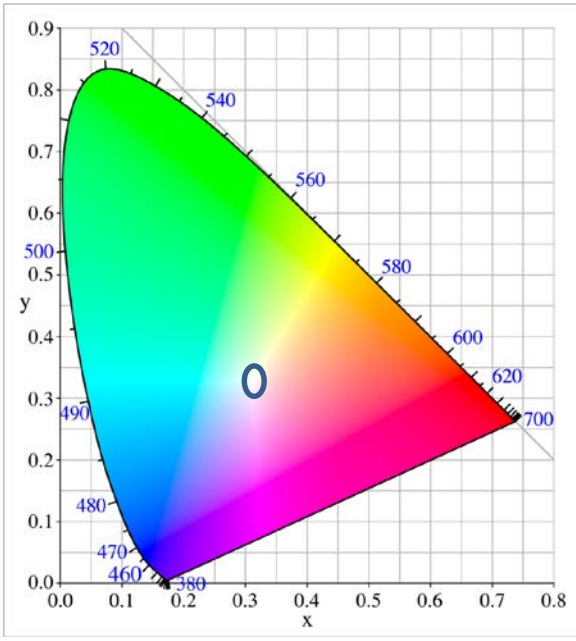

Figure 3.3 The CIE 1931 chromaticity diagram. Point in the center represents the point (0.333, 0.333) of equal energy and is the daylight white standard

3.2.2 White Light

In 1900, Max Plank described the electromagnetic radiation emitted by a black body in thermal equilibrium at a definite temperature [116]. This law is a pioneering result of modern physics and quantum theory, and is appropriately named Plank's law:

$$B(\lambda, \mathrm{T}) = \frac{2hc^2}{\lambda^5} \cdot \frac{1}{exp\left[\frac{hc}{\lambda \mathrm{k}_B T} - 1\right]} \tag{3.23}$$

where k_B is Boltzmann's constant, h is Plank's constant and c is the speed of light. In order for a white light source to be perceived as pleasant, not only does it need to appear 'white', but the spectral content must be such that colors illuminated by the source look the same as under a Planckian source. Mixing any two colors that form a straight line that intersects the point of equal energy (0.333, 0.333) on the CIE chromaticity diagram will produce color that 'appears' white, however the quality of the light quickly becomes bleak and unsaturated when colors are chosen lying away from this connecting line. The quality of this light is quantified by the color rendering index (CRI). The values of the CRI range from 0 -100, where higher values indicate better color rendering. It is widely accepted that a CRI > 90 is needed for a high quality solid-state lighting source [118]. An overview of the CRI values for different light sources is provided in Table 3. OLEDs have garnered a lot of interest as a next generation solid-state lighting alternative due to their broad and tunable emission spectrums. This provides device engineers with an ability to emulate the spectrum of thermal radiation and increase the device's CRI [47].

Table 3 Typical CRI values present in consumer lighting sources (from [115]).

Type	**CRI**
Incandescent Bulb	100
Halogen	100
Compact Fluorescent Lamp	80 – 90
Fluorescent Tube	50 – 95
LED Bulb	70 – 90
High-Intensity Discharge	65 – 95
OLED Luminaire	75 – 90

3.3 Fabrication and Measurement Details

3.3.1 OLED Fabrication

OLED substrates consisting of indium tin-oxide coated glass sheets (Colorado Concepts Coatings LLC) with a sheet resistance of 15 Ω/sq were cut into 1 × 1 inch squares and patterned using 1/2 inch strips of Kapton tape and exposing the remaining ITO to an acid bath of HCl: HNO_3 (3:1) for 5 min. The substrates were then cleaned by ultra-sonication (5510, Branson Ultrasonics) for 25 min in each of the following: water with detergent, distilled water, acetone, and isopropanol. They were then blown dry with nitrogen before exposed to oxygen plasma (Plasma-Preen II, Plasmatic Systems, Inc.) for 5 min. Immediately after, the samples were transferred to a glove box with a nitrogen atmosphere and loaded into a ultra-high vacuum thermal evaporation system (EvoVac, Armstrong Engineering Inc).

All the materials thermally evaporated are done so when the VTE system is evacuated to a base pressure of $< 1 \times 10^{-7}$ Torr. All metal layers were deposited at a rate of 2 Å/s and all other inorganic materials, such as LiF and MoO_3, were deposited at a rate of 0.2 Å/s. The organic layers were deposited at a rate of 1 Å/s. The typical active area of a completed device is about 3.6 × 4.2 mm. The patterning on a substrate was achieved by evaporating through a series of shadow masks sequentially placed in near-contact to the substrate. A general layout of a completed device is shown in Figure 3.4. Unless otherwise specified, all organic materials were purchased from Sigma-Aldrich (St. Louis, MO, USA) or Luminescence echnology Corporation (Hsin-Chu, Taiwan) and purified by

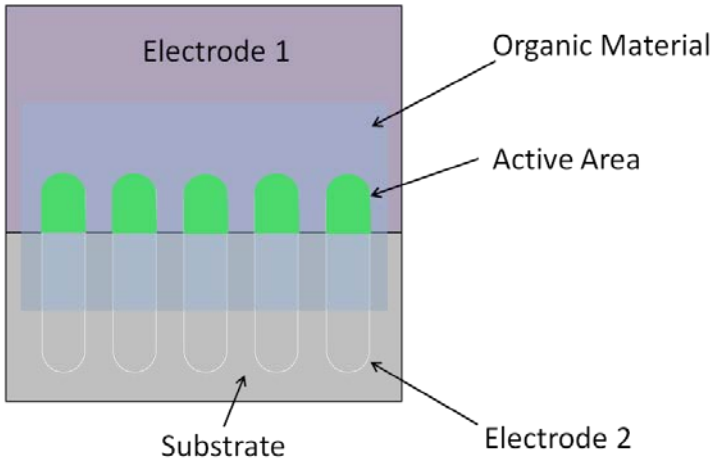

Figure 3.4 Substrate layout of a completed device.

gradient-zone sublimation prior to their deposition by thermal evaporation. After fabrication, the thermal evaporator is opened within a nitrogen-filled glove box, where the devices are measured.

3.3.2 OLED Measurement

Current vs. voltage and luminance vs. voltage characteristics of devices were acquired using a custom-built measurement setup consisting of various pieces of equipment controlled by a computer workstation running control software (National Instruments LabVIEW). When measuring OLEDs, they were placed behind a quartz window within a custom-built enclosure and connected to electrical pins. A general-purpose source measure unit (Keithley 2400 SourceMeter) was used to measure the current of the OLED as a function of the voltage applied. The emitted light exits the quartz window, and a radiometrically calibrated photodiode (Thorlabs Inc, FDS 100) was used to measure the optical power emitted from the OLED in the direction normal to its surface. The photocurrent generated by the photodetector was amplified by an operational amplifier

(AD 549LH) in a current-to-voltage converting circuit with an amplifying feedback resistor. The output voltage was acquired by a digital acquisition unit (National Instruments USB-6221) which was connected to the workstation.

A schematic view of the OLED measurement setup is shown in Figure 3.5. The workstation records the OLED voltage, OLED current, and photodetector voltage and uses these to calculate the OLED performance characteristics, such as luminance, current efficacy, and EQE (when the OLED is a Lambertian emitter) at each data point.

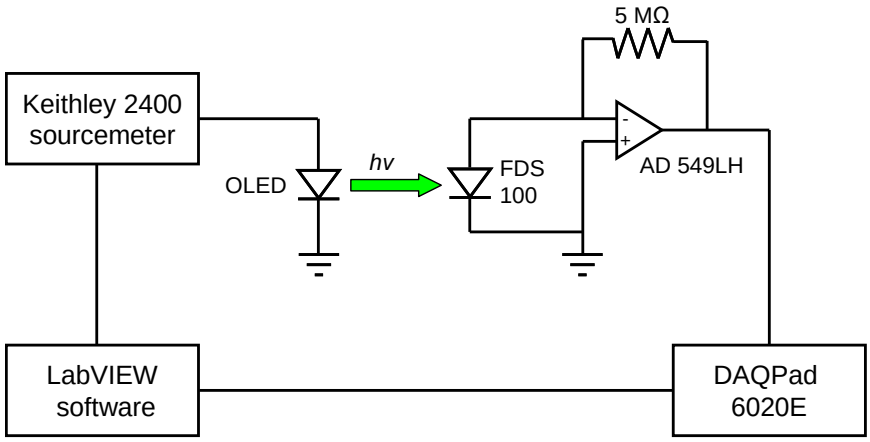

Figure 3.5 Graphically illustration of custom-built OLED test set-up used to characterize the electrical and optical properties of the device

In order to measure the angular-dependent electroluminescent spectra of the OLED, an electronically controlled rotation stage to accurately control and measure the device spectrum at various angles was designed and built. This stage worked by manually inserting an OLED into a housing unit that used electrical pins to hold the substrate in place and provide electrical contact to the device. A Keithley 2400 SourceMeter was used to bias the OLEDs and the spectra were collected with a radiometrically calibrated spectrometer (Ocean Optics USB4000) interfaced with a workstation. The spectrum was collected at

each angle of interest by rotating the device using a software-controlled motor connected to the rotatable stage.

CHAPTER 4

Electrophosphorescent OLEDs Using a Solution Processed Hole-Transport Layer and Universal Host Material

There is a strong focus in the OLED community to develop OLEDs based on electrophosphorescence because both singlet and triplet excitons can be harvested a for potential 100% IQE, which can lead to state-of-the-art efficiencies. However, these state-of-the-art OLED structures often utilize unstable materials and dopants, or involve complex device designs that are difficult to scale to high-volume manufacturing settings. In this chapter, we present a simple, three-layer OLED device structure that produces device efficiencies that are comparable to or better than state-of-the-art performance metrics reported in the literature. This device structure utilizes a pair of novel materials (a solution-processed HTL material and a universal host material) that are effective at harvesting excitons for both green and blue light emission. Experimental results are shown to support the conclusion that this novel pair leads to an optimal charge balance in the recombination layer.

4.1 State-of-the-Art Electrophosphorescent OLEDs

In one of the first reports of electrophosphorescence in an OLED, Baldo et al. used the green phosphorescent emitter *fac* tris(2-phenylpyridinato-N,$C^{2'}$) iridium ($Ir(ppy)_3$, as the emissive complex and obtained an external quantum efficiency (EQE) of 7.5% (26 cd/A) at 100 cd/m^2 [44]. Their device structure consisted of 4,4'-bis[*N*-(1-naphthyl)-*N*-

phenyl-amino]biphenyl (α-NPD) as the hole-transport layer, 4,4'-di(carbazol-9-yl)-biphenyl (CBP) as a host for $Ir(ppy)_3$, 2,9-dimethyl-4,7-diphenyl-1,10-phenanthroline (BCP) as a hole-blocking layer, and tris-(8-hydroxyquinolinato-N,O) aluminum (Alq_3) as an electron-transport layer. The device was capped with a Mg:Ag cathode. The chemical structures for these materials and the device layout are shown in Figure 4.1.

Since this first report, the OLED community has made great advances in understanding methods to improve the device efficiency, light output, turn-on voltage and

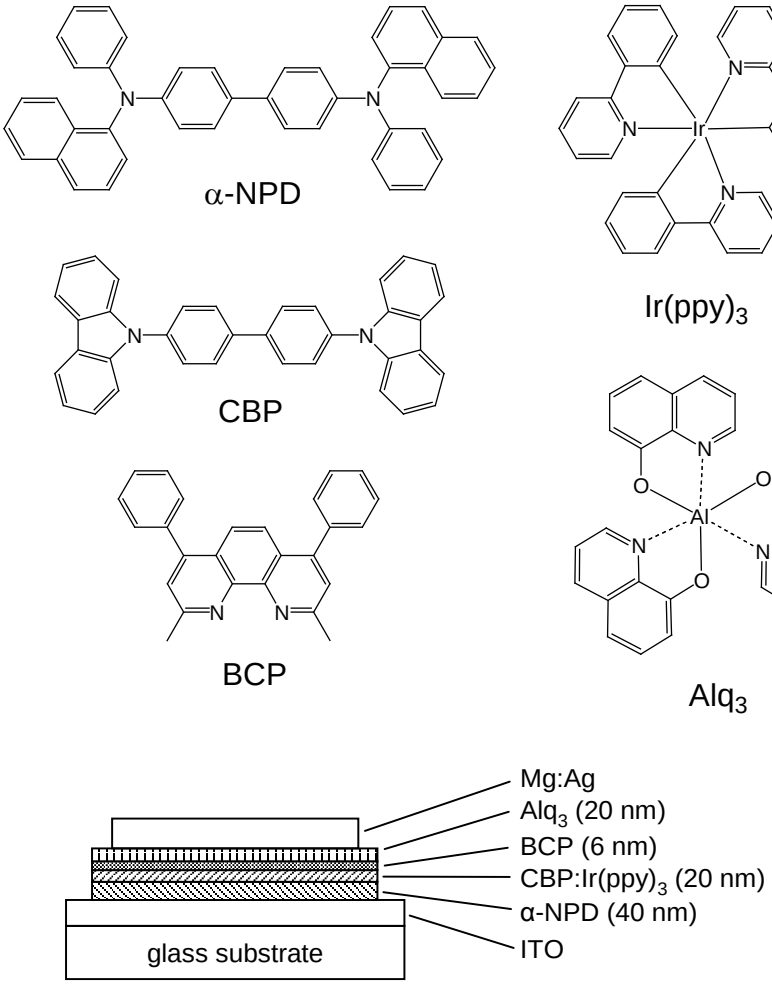

Figure 4.1 (Top) Chemical structures used in Baldo et al. device, and (Bottom) device structure from his first demonstration of efficient electrophosphorence. Figure taken from [41].

roll-off [29, 119]. These design strategies include using different host/guest materials to improve the energy transfer between materials, hole- and electron- blocking materials with large band-gaps for better exciton confinement in the emissive layer, doped hole- and electron- transport materials to enhance charge balance in the emissive layer and hole- and electron- injection materials to reduce the barrier between the electrodes and organic semiconductors [68, 120-122]. However, the most common design strategy is use a combination of multiple (or all) of these design methods.

The current state-of-the-art for an out-coupled device was demonstrated by Wang et al. in 2011 [20]. They showed that through a effective device design that minimized the energetic difference between the ETL 2,2',2" -(1,3,5-benzinetriyl)-tris(1- phenyl-1-H-benzimidazole) (TPBi) and host CBP it was possible to enhance charge transport and recombination in the EML. This device produced an EQE over 60% and a power efficacy over 250 lm/W at a turn-on luminance of 10 cd/m^2. However, their device structure relied on two different ETL materials and a complex electrode/substrate stack that improved their benchmark results by 150% through effective out-coupling. The state-of-the-art in performance for a non-out-coupled device was demonstrated by Kim et al. in 2013 [45]. Their devices produced an EQE of 30.2% and power efficacy of 127.3 lm/W at a turn-on luminance of 10 cd/m^2. These two reports had two things in common: they both utilized the horizontally oriented green phosphor bis(2-phenylpyridine) (acetylacetonate)iridium(III) (Ir(ppy)$_2$(acac)) doped in a CBP matrix as the EML and their device designs both required complex systems to generate equal charge-balance in the EML and high performance. The device structures from both Wang and Kim are shown in Figure 4.2. Ir(ppy)$_2$(acac) has been shown to be a superior dopant to Ir(ppy)$_3$ because of its

horizontal transition dipole moment that results in a much higher out-coupling efficiency than the vertically aligned $Ir(ppy)_3$ [45, 123]. This horizontal dipole alignment is believed to minimize the effect of polaron loses from the cathode [28].

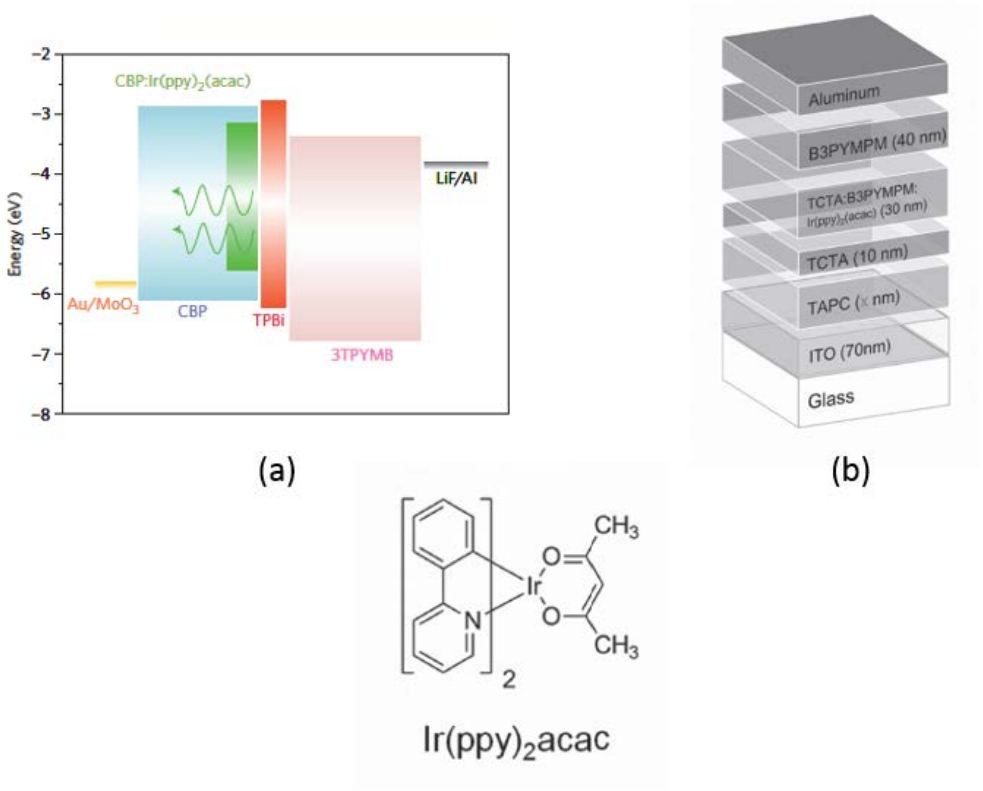

Figure 4.2 (a) Device Structure from Wang et al. [20] (b) Device structure from Kim et al. [45] (Bottom) Chemical structure of $Ir(ppy)_2(acac)$

The current state-of-the-art performance for blue-emitting OLEDs was demonstrated by Kido et al. in 2014 and incorporated the use of a novel ETL material Tm3PyP26PyB [22]. Their device had a structure of ITO/TPDPES (20 nm)/TAPC (30 nm)/DCzPPy:FIrpic (10 nm 0.87:0.13)/Tm3PyP26PyB (50 nm)/LiF (0.5 nm)/Al (100 nm) and produced devices with a peak EQE of 25.7% and a current efficacy of 65.8 cd/A. At

high luminance values of 1,000 cd/m^2, the EQE and current efficacy reduced to 22.6% and 49.8 cd/A, respectively. In their work, they attributed the high performance of these devices on the improved electron injection created with the new ETL material. They speculated that this increased injection induces an aggregation of electrons on the cathode side of the EML and thus increases the internal electric field. This should result in an acceleration of hole injection/transport from the anode due to the increased electric field.

4.1.1 Design Challenges

While these device designs offer high efficiencies, their complex structures and material choices offer inherent disadvantages that make them hard to reproduce, operational unstable and limited with regards to emitted color [124, 125]. It is advantageous to design an OLED structure with materials that have a glass transition temperature (T_g) 100 °C or greater because they provide greater stability and longer device lifetimes [26]. Wang et al. used CBP as the host matrix in his device. This material has a T_g of 62 °C and has been shown to crystallize after only five-minutes of operation and has a low triplet energy of 2.6 eV, which makes its unsuitable for blue- (or deep-blue-emitting) phosphors that have triplet energies upwards of 3.0 eV. While Kim et al. used a different host material (TcTa) with a higher (T_g = 151 °C), they were dependent on a complex tri-layer emission layer (TcTa:B3YMPM: Ir(ppy)$_2$(acac)) to achieve equal charge balance in their device. In this chapter, we present a simplified device structure that utilizes a novel HTL and ambipolar host material, which both have a T_g > 140 °C have and triplet energies > 3.0 eV. These materials can, thus, be applied to act as a universal HTL/host matrix combination that is suitable for red-, green-, and deep-blue-emitting phosphors. The novel

materials presented in this chapter were synthesized by collaborators in Prof. Seth Marder's group in the Georgia Tech College of Chemistry.

4.2 Solution-Processed Hole-Transporting Material Design

The hole transport material Poly(6-(9H-carbazol-9-yl)-9-(4-vinylbenzyl)-9H-3,9'-bicarbazole)) (Poly-TriCZ) was synthesized to exhibit superior hole-mobility, a high triplet energy and a high T_g to ensure operational stability. A Schlenk flask was charged with the tricarbazole-stryene monomer (1.0 g, 1.6 mmol), AIBN (7.0 mg, 0.042 mmol) and dry THF (20.0 mL). The polymerization mixture was purged with nitrogen, securely sealed and stirred at 60 °C for 7 d. After cooling to room temperature, the polymer was precipitated with acetone. The white precipitate was collected by filtration, dissolved in dichloromethane and precipitated with acetone again. This dissolution/precipitation procedure was repeated three more times and the resulting white solid was dried under vacuum (0.93 g, 93%). The chemical structure for Poly-TriCZ is shown below in Figure 4.3 and the material properties are provided in Table 4.

Films of Poly-TriCZ were created through spin-coating. To prepare the solution, 1 mg of Poly-TriCz was dissolved in 1 mL of anhydrous chlorobenzene (Aldrich) and placed on a spinner in a nitrogen glove box for 5 h to thoroughly dissolve. The solution was then dispensed through a 0.20 µm polyvinylidine fluoride filter and 50 nm-thick films were deposited by spin-coating the solution at 750 rpm for 60 s. The films were then annealed on a hot-plate at 110 ºC for 2 min.

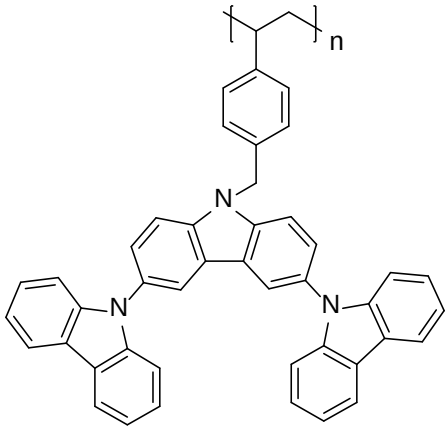

Figure 4.3 Chemical structure for the polymeric HTL Poly-TriCZ

Table 4 Electronic and thermal properties of Poly-TriCZ

Material	**IE (eV)**	**EA (eV)**	T_1 **(eV)**	S_1 **(eV)**	T_g **(** °C)
Poly-TriCZ	5.5	2.0	2.9	N/A	296

4.3 Ambipolar Sulfone-Carbazole Host Material Design

There are two main factors that contribute to the quantum efficiency of an electrophosphorescent OLED: energy transfer from the hosts to the guests and charge balance in the emissive layer [25, 29]. In order to maximize the performance of a device, it is critical to select a host material that not only has a higher triplet energy than the guest, but also provides equal electron- and hole-transport to optimize exciton formation (ambipolar transporting properties). Ambipolar host materials are effective strategies to optimize charge transport and recombination in the EML of an OLED. Thus, the development of new ambipolar host materials is critical to both improve device performance and simplify their design [28, 48]. Carbazole derivatives as host materials

have been widely used for phosphorescent OLEDs due to their tunable triplet energies and good hole-transport properties. These materials can produce ambipolar characteristics if electron-transport moieties are added to these materials as an acceptor. These electron-transport properties can be added with pyridine, triazine, phosphine-oxide, oxadiazole, triazole, benzimidazole, phenanthroline, phosphine-sulfide or sulfone moieties. The ambipolar host material investigated in this work 3,5-Di(carbazol-9-yl)-1-phenylsulfonylbenzene (mCPSOB) is based on a carbazole derivative with a sulfone acceptor. The chemical structure and material synthesis scheme of mCPSOB is shown in Figure 4.4.

mCPSOB was designed and synthesized to exhibit superior electron- and hole-mobility, a high triplet energy and a high T_g. Table 5 highlights the thermal and electronic properties of mCPSOB.

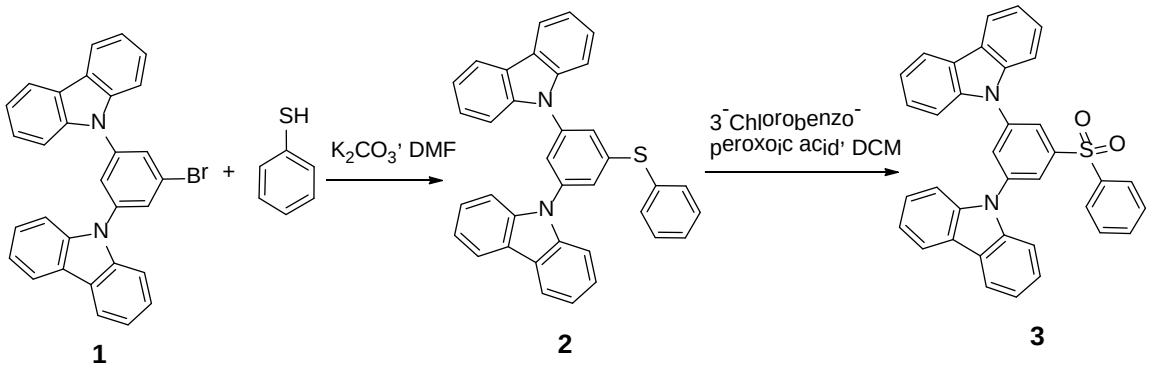

Figure 4.4 The synthesis scheme for the sulfone-carbazole host material mCPSOB

Table 5 Electronic and thermal properties of mCPSOB

Material	IE (eV)	EA (eV)	T_1 (eV)	S_1 (eV)	T_g (°C)
mCPSOB	5.8	2.5	3.02	2.93	140

The IE and EA of mCPSOB and Poly-TriCZ were obtained using cyclic voltammetry and absorption onset, the singlet and triplet energy levels were measured from the phosphorescence spectra in 2-methyltetrahydrofuran at 77 K and the T_g was measured by differential scanning calorimetry (DSC).

4.4 Design of Simplified OLED Architecture

As previously mentioned, modern small-molecule OLEDs are complex, multi-layer devices that consist of thin films of metals, inorganic materials and organic semiconductor materials. Each of the material in these devices serves a function in order to increase the performance of the device, whether that be a reduction in turn-on voltage, an increase in performance efficiency or an increase in operational stability.

The efficiency of conventional bottom-emitting OLED can be improved by making some of these modifications. It is well known that the barrier to hole injection from an ITO anode can be reduced by treating the ITO with O_2 plasma, which increases its work function from 4.2 eV to 4.7 eV [126-128]. The modified ITO work function of 4.7 eV still results in an injection barrier to many HTL materials, but the work function can be further increased by coating it with a conductive polymer with a higher work function, such as PEDOT:PSS or MoO_3 [129]. The PEDOT:PSS layer also planarizes the surface of the ITO and may act to prevent the diffusion of ions from the ITO into neighboring organic, enhancing the operational lifetime of the device [130, 131]. The process of electron injection can also be enhanced by replacing the Mg:Ag cathode with an Al/LiF cathode and by replacing the Alq_3 ETL with an ETL, such as BCP, TAZ or TPBi among others

[43]. Finally, the layer thicknesses can be optimized through a systematic experimentation and screening processes.

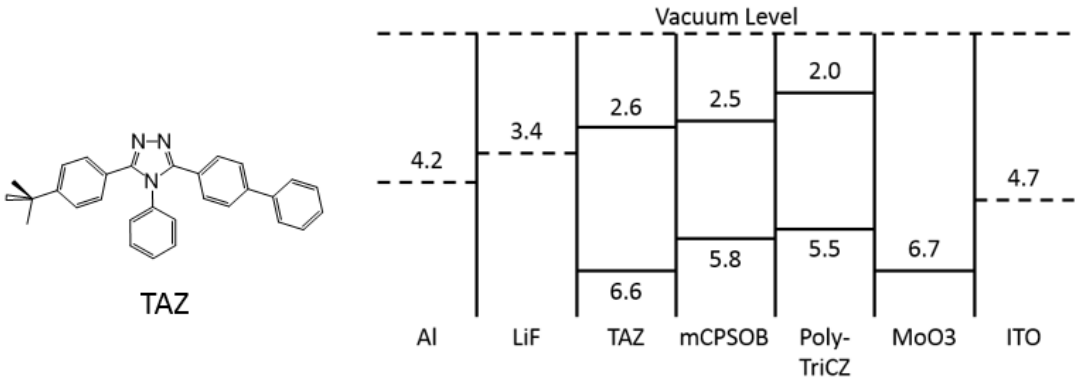

Figure 4.5 (Left) Chemical structure for the ETL material TAZ. (Right) Energy level diagram for the various materials used in the OLED design.

The work shown in this chapter uses the ETL TAZ due to its wide band-gap and favorable energy alignment to mCPSOB (Figure 4.5). This wide band-gap serves as both an efficient exciton confinement layer and a hole-blocking layer, which prevents holes from escaping the EML and quenching electrons before they have an opportunity to recombine [27, 132]. Additionally, two HIL materials PEDOT:PSS and MoO_3 are demonstrated in the device structure to highlight the performance advantages of each respected material on the completed device.

4.4.1 Green Electrophosphorescent OLED Results

Simple three-layer organic devices were prepared using the pair of novel materials Poly-TriCZ and mCPSOB highlighted above in Section 4.3. For the purpose of this study, the iridium complex $Ir(ppy)_3$ was selected as the guest material in the mCPSOB matrix and

the materials were co-deposited at a rate of 0.94:0.06 in a thermal evaporator. The structure for these devices is highlighted in Figure 4.6.

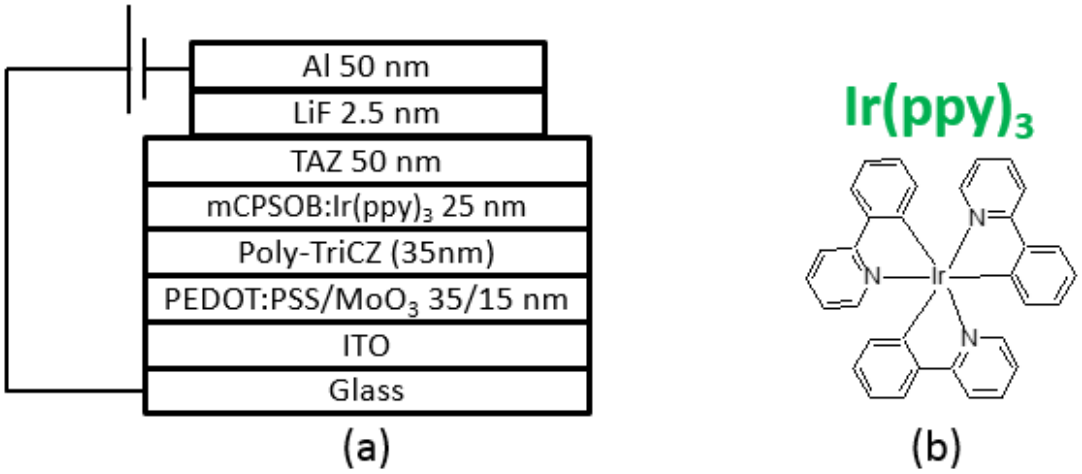

Figure 4.6 (a) Device structure for the three-layer green-emitting OLED (b) Chemical structure for the green-emitting phosphor $Ir(ppy)_3$

The HIL choice of PEDOT:PSS or MoO_3 each offer distinct design advantages. For comparison, the current density vs. voltage and EQE/luminance vs. voltage plots for both devices are shown in Figures 4.7 ad 4.8, respectively. The PEDOT:PSS HIL produced extremely efficiency devices, with a maximum EQE > 28% and a current efficacy of 103.4 cd/A. These values are on par with the state- of-the-art OLEDs with $Ir(ppy)_3$ as the green-emitting phosphor [124], and these results are achieved in a simple, three-layer organic stack. Moreover, these devices maintain an EQE

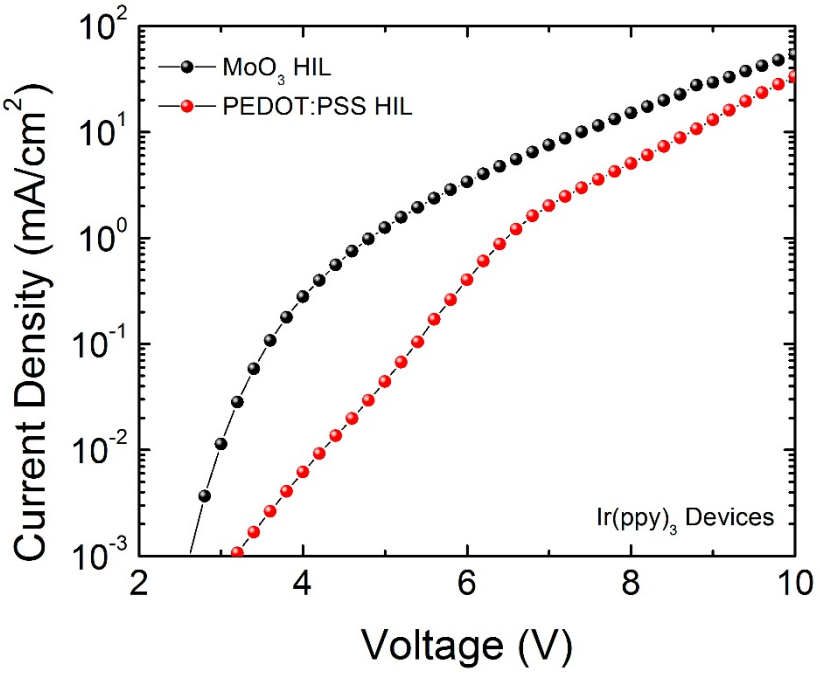

Figure 4.7 Current density versus voltage plot for $Ir(ppy)_3$ devices with a MoO_3 and PEDOT:PSS HIL

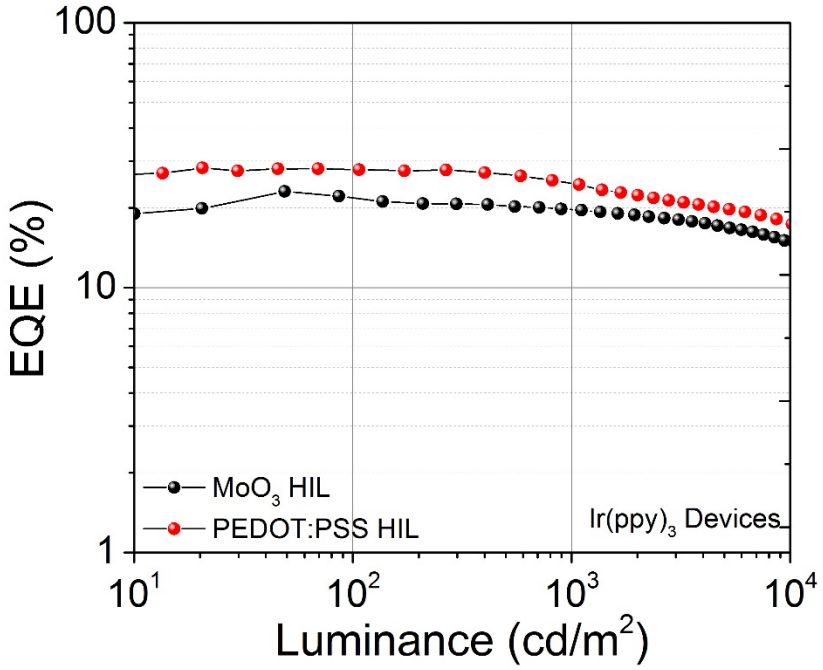

Figure 4.8 Luminance versus EQE data for $Ir(ppy)_3$ devices with a MoO_3 and PEDOT:PSS HIL

Table 6 Performance of mCPSOB:Ir(ppy)$_3$ Devices with MoO_3 and PEDOT:PSS HIL

HIL	V_{ON} (V)	EQE* (%)	EQE_{1000} (%)	Current Efficacy* (cd/A)	Current $Efficacy_{1000}$ (cd/A)
MoO_3	3.0	20.2	19.2	73.0	69.5
PEDOT:PSS	4.2	28.4	24.5	103.4	90.0

*Indicates values at turn-on voltage

near 25% and a current efficacy of 90 cd/A at a high luminance of 1,000 cd/m^2. The devices with a MoO_3 HIL displayed a similar high performance, but with a much lower efficiency roll-off.

Comparing the performance of these devices results in two key observations are made. One: the devices with the PEDOT:PSS HIL exhibit superior performance than those with the MoO_3 HIL. Two: the MoO_3 devices have a turn-on voltage of 1.2 V lower than those with PEDOT:PSS, and exhibit a better diode rectification/behavior. This suggest that PEDOT:PSS provides better charge balance in the EML of the device, but is much worst at injection holes into the Poly-TriCZ HTL than MoO_3. This can be explained by the deep work-function of MoO_3 compared to PEDOT:PSS (~ 6.7 eV and 5.0 eV, respectively), which might form a potential well at the MoO_3/Poly-TriCZ interface [133].

4.4.2 Blue Electrophosphorescent OLED Results

Because mCPSOB and Poly-TriCZ both have high triplet energy levels, they are both suitable material choices for blue-emitting devices. Engineering efficient blue-emitting OLEDs is difficult because the high energy of the emitting phosphors makes it difficult to pair them with host materials that can provide endothermic energy transfer, and

with transport materials that can confine these excited states in the EML and allow them to radiatively decay [25]. Because of these challenges, most state-of-the-art blue OLED structures employ extremely complex designs that utilize dopants, interlayers, blocking layers, confinement layers or a combination of the all. By extending the work highlighted in Section 4.4.3 with green-emitting phosphors, we were able to show state-of-the-art performance for blue-emitting OLEDs in this universal host/HTL system.

The blue-emitting iridium complex selected as the guest material in the mCPSOB matrix was FIrpic and the materials were co-deposited at a rate of 0.88:0.12 in a thermal evaporator. The structure for these devices is highlighted in Figure 4.9. As with the green-emitting devices, both HIL materials PEDOT:PSS and MoO_3 were investigated in this study and their results are compared side-by-side.

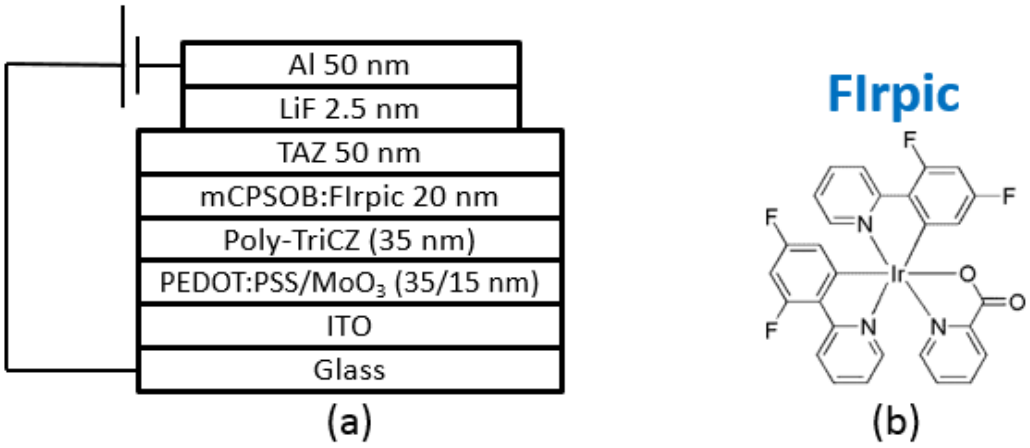

Figure 4.9 (a) Device structure for the three-layer blue-emitting OLED (b) Chemical structure for the green-emitting phosphor FIrpic

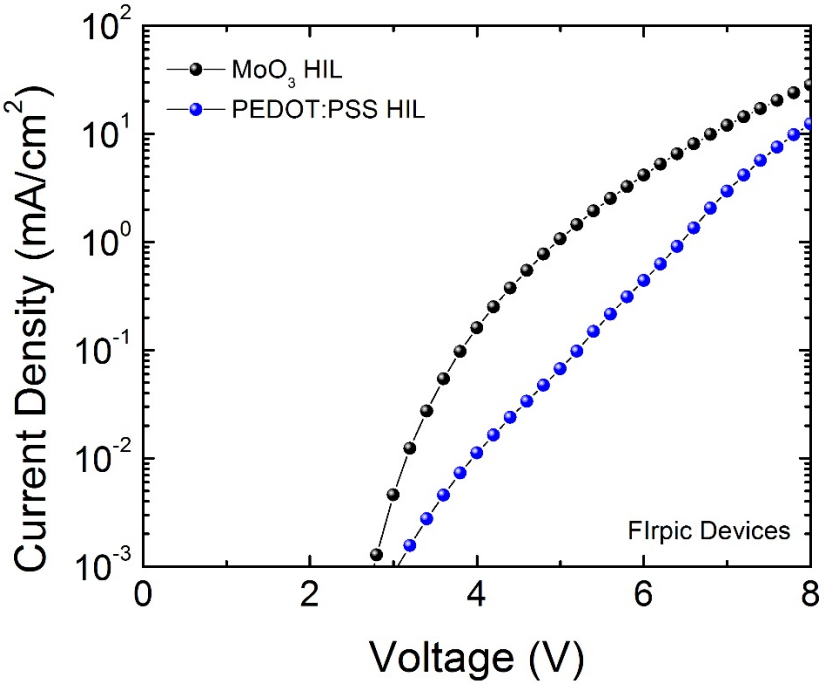

Figure 4.10 Current density versus voltage plot for FIrpic devices with a MoO_3 and PEDOT:PSS HIL

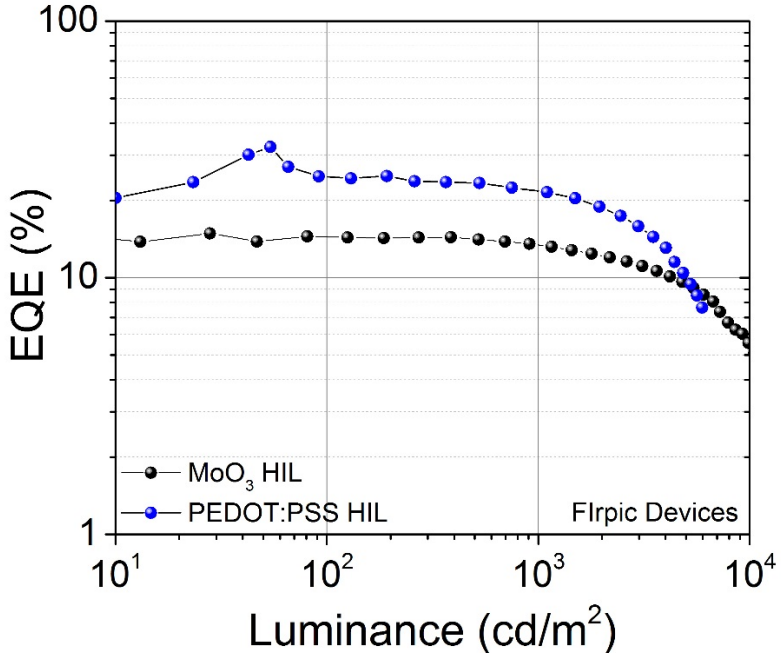

Figure 4.11 Luminance versus EQE data for FIrpic devices with a MoO_3 and PEDOT:PSS HIL

Table 7 Performance of mCPSOB:FIrpic Devices with MoO_3 and PEDOT:PSS HIL

HIL	V_{ON} (V)	EQE* (%)	EQE_{1000} (%)	Current Efficacy* (cd/A)	Current $Efficacy_{1000}$ (cd/A)
MoO_3	3.4	14.6	12.6	50.6	43.5
PEDOT:PSS	5.0	32.3	21.5	80.2	53.5

*Indicates values at turn-on voltage

Again, the PEDOT:PSS HIL produced extremely efficiency devices, with a maximum EQE > 32% and a current efficacy of 80 cd/A. These values represent the state-of-the-art in performance for blue-emitting OLEDs, and these results are achieved in a simple, three-layer organic stack. However, the roll-off is more pronounced in these devices than with the green-emitting phosphor $Ir(ppy)_3$, with an EQE of 21/5% and a current efficacy of 53.5 cd/A at a high luminance of 1,000 cd/m^2. Although this is a sizeable drop from the turn-on level efficiencies, they still represent very efficient devices and demonstrate the effectiveness of the Poly-TriCZ and mCPSOB HTL/EML combination and creating a charge balance in the EML.

The devices with a MoO_3 HIL did not display as high of a performance as the PEDOT:PSS devices, but they did follow the same trends as the $Ir(ppy)_3$ devices: they had a turn-on voltage of 1.6 V lower than PEDOT:PSS, demonstrated much lower efficiency roll-off, exhibited a much greater diode rectification/behavior. These are important observations and key factors to consider for future device design.

The electroluminescence (EL) spectrum from both the green-emitting and blue-emitting phosphors is provided in Figure 4.12. The CIE coordinates for the green-emitting

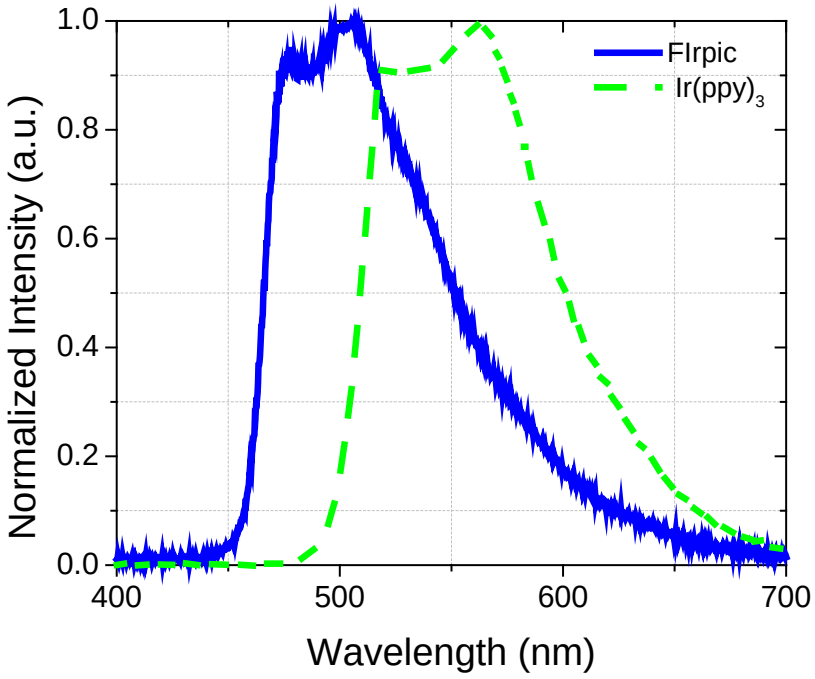

Figure 4.12 EL spectrum of OLEDs with the green-emitting phosphor $Ir(ppy)_3$ and the blue-emitting phosphor FIrpic in the device structurem illustrated in Figures 4.6 and 4.9, respectively

OLED and blue-emitting OLED were measured to be (0.40, 0.57) and (0.23, 0.47), respectively.

CHAPTER 5

High Performance Organic Light-Emitting Diodes from Thermally Activated Delayed Fluorescence

The work presented in this chapter builds on the work highlighted in Chapter 4. In this chapter, we use the simplified three-layer device structure that was shown to produce highly efficient blue- and green-emitting electrophosphorescent OLEDs and demonstrate its suitability with thermally activated delayed fluorescence (TADF) emitters. These TADF emitters are capable of generating the same 100% IQE as phosphorescent OLEDs, but without the need for expensive, heavy-metal based materials.

5.1 State-of-the-Art TADF OLEDs

Historically, high-efficiency OLEDs have been fabricated with phosphorescent emitters, such as iridium- or platinum-containing complexes [19, 31, 44]. Unlike common fluorescent emitters, which emit light from a singlet excited state, these heavy-metal containing phosphorescent emitting materials harvest excitons from both the singlet and triplet excited states for electroluminescence via enhanced intersystem crossing (ISC) [44]. This results in an internal quantum efficiency (IQE) close to 100% in phosphorescent based OLEDs . However, the precious metals (such as iridium) found in these present their own set of challenges, which have made it difficult for OLEDs to become competitive in the solid-state lighting markets.

Recently, Adachi and co-workers were able to show highly efficient OLEDs from thermally activated delayed fluorescence (TADF) [39, 53, 134-136]. This novel approach

utilizes emitter molecules wherein the small energy difference between the singlet and triplet states in select organic molecules to achieve TADF [135]. Like typical fluorescent emitters, the light emission in these emitters arises from the singlet excited state; however, efficient TADF allows for excitons from the triplet state to be harnessed from the singlet state by reverse intersystem crossing through thermal activation – producing IQE's near 100% from singlet state emission compared to the 25% in conventional fluorescent emitters [39, 53, 134-136]. This mechanism has allowed for a new class of efficient heavy-metal-free fluorescent emitters to be developed that have yielded efficiencies comparable to those of the most efficient heavy-metal phosphorescent-emitter-based OLEDs [39, 49, 50, 136].

In general, (4s,6s)-2,4,5,6-tetra(9H-carbazol-9-yl)isophthalonitrile (4CzIPN) has been used as the benchmark green-emitting TADF emitter, producing a maximum external quantum efficiency (EQE) of 19.3% when doped in a CBP host-matrix at a 1% wt. concentration [39]. However, recent work has shown that this efficiency can be further improved with the use of ambipolar host materials, and TADF devices with EQEs over 25% have been reported utilizing materials with similar hole and electron mobility values [49]. These host materials with ambipolar charge transport properties have been shown to be critical to the development of highly efficient phosphorescent OLEDs because they facilitate charge injection and charge balance within the emissive layer of these devices [26, 73].

These ambipolar host materials have also been shown to yield superior performance with blue TADF dopants as well. The sky blue TADF dopant 1,2-bis(carbazol-9-yl)-4,5-dicyanobenzene (2CzPN) has been the focus of increasing research in the OLED community and groups have demonstrated high efficiencies over 15% EQE when this

material is doped in a novel host matrix. Li et al. demonstrated devices that produced a maximum EQE of 15.8% at 1 cd/m^2, 9.0% at 100 cd/m^2 and 4.1% at 1,000 cd/m^2. The main issue with blue TADF dopants (and 2CzPN especially) is the poor stability of the devices. Due to the many complexities involved with designing efficient blue-emitting OLED structures, the efficiency roll-off present in blue TADF devices is a major concern. Maintaining an equal charge-balance in the EML with increased bias has proven to be very difficult with 2CzPN and clever design strategies are necessary to minimize this effect, via new host engineering, exciton confinement layers or high mobility transport materials.

5.2 Device Results

5.2.1 Green-Emitting TADF OLEDs

As described in Chapter 4, the host material mCPSOB (Figure 1) can act as a suitable matrix for both green and blue emitters due to its high triplet energy of 3.02 eV. the TADF emitters 4CzIPN and 2CzPN and produce state-of-the-art efficiencies for both green- and blue-emitting OLEDs. The ambipolar host material shows high singlet and triplet energies of 2.93 eV and 3.02 eV, respectively, measured from the phosphorescence spectra in 2-methyltetrahydrofuran at 77 K. The ionization energy (IE) (or (HOMO) energy) and the electron affinity (EA) (or (LUMO) energy) were determined to have values of 5.8 eV and 2.5 eV, respectively. When doped in this host matrix, 4CzIPN based OLEDs were produced that yielded EQEs of 26.5% and 21.5% at luminance values of 10 cd/m^2 and 1,000 cd/m^2, respectively and very low roll-off at high current densities. These are among the highest efficiencies ever reported for TADF based OLEDs.

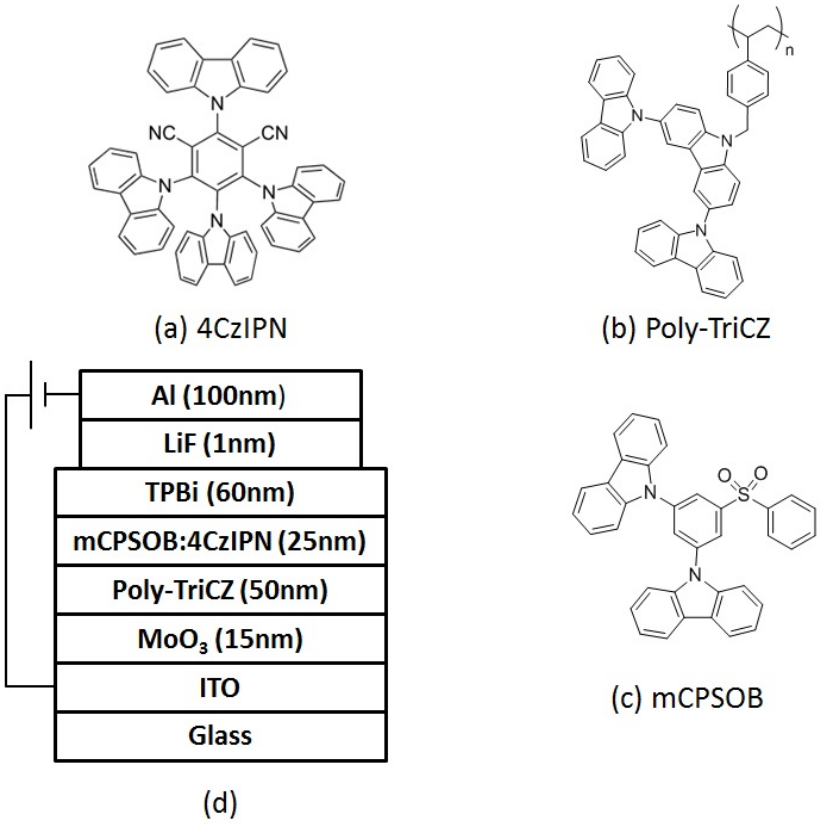

Figure 5.1 (a) Chemical structure of TADF dopant 4CzIPN. (b) Chemical structure of hole-transporting material Poly-TriCZ. (c) Chemical Structure of ambipolar host material mCPSOB. (d) Device structure of the TADF OLED using mCPSOB as the host material. CBP host device used the same structure.

The mCPSOB host used in this report was designed to exhibit ambipolar charge transport properties, and combines carbazole hole transporting materials with a phenylsulfone electron transporting moiety [48]. Additionally, it was measured to have a high glass transition temperature (T_g) of 140 °C. This high T_g helps produce thermally and morphologically stable films, which prevents mCPSOB from crystallizing during operation and reduces the possibility of phase separation upon heating of the device, increasing its operational stability [26].

The OLED device structure studied in this paper is presented in Figure 5.1. Poly-TriCZ was used as the hole transport material, and TPBi was used as the electron transport material. Devices with a CBP host were also fabricated as benchmarks to compare to the mCPSOB devices. These CBP host matrix devices were fabricated strictly for comparison to the mCPSOB devices and to highlight the device performance improvement obtained when only the host material was changed. The current state-of-the-art performance for CBP based TADF devices is 19.3%, as reported by Adachi et al [39]. Figures 5.2 and 5.3 show the current density versus voltage (*I*-*V*) and luminance versus voltage (*L*-*V*) characteristics of the mCPSOB host devices. The devices exhibited a turn-on voltage of 3.2 V at 10 cd/m^2 and 4.8 V at 1,000 cd/m^2. Table 8 shows the power efficacies of this device at various luminance values with average values and standard deviations measured over five devices. Strong rectification indicates efficient carrier injection and transport between the transport layers and the mCPSOB EML. Current efficacy and EQE are shown in Figures 5.4 and 5.5. The EQE reached 26.5% (80.6 cd/A), 24.3% (73.7 cd/A) and 21.5% (67.1 cd/A) at 10 cd/m^2, 100 cd/m^2, and 1,000 cd/m^2, respectively, with a doping concentration of 5 wt. % mCPSOB:4CzIPN. Not only are these values among the highest ever reported on TADF OLEDs, but they are also comparable to the most efficient green-emitting phosphorescent OLEDs reported as well [45]. It is worth noting that these devices were not fully optimized, and it has been shown that reducing the dopant concentration can further improve the device performance [39, 49, 50, 135].

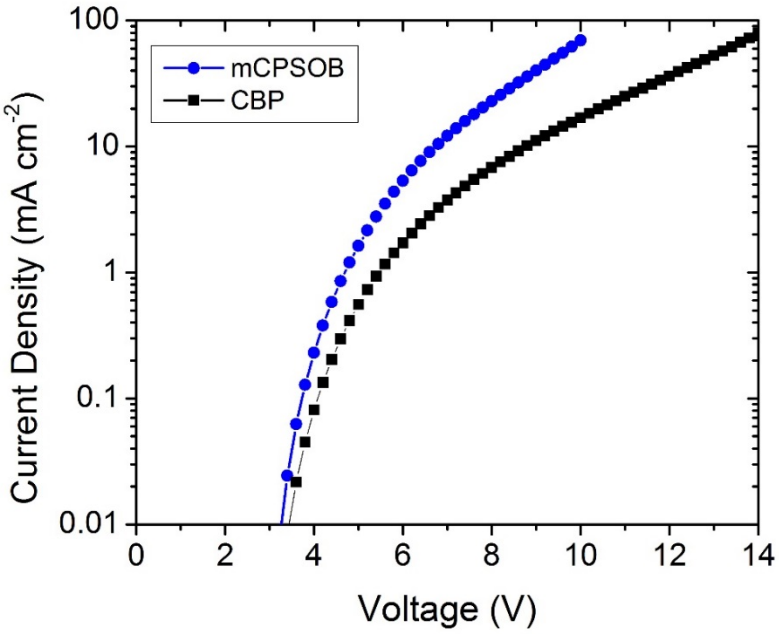

Figure 5.2 Current density versus voltage for mCPSOB- and CBP-based OLEDs.

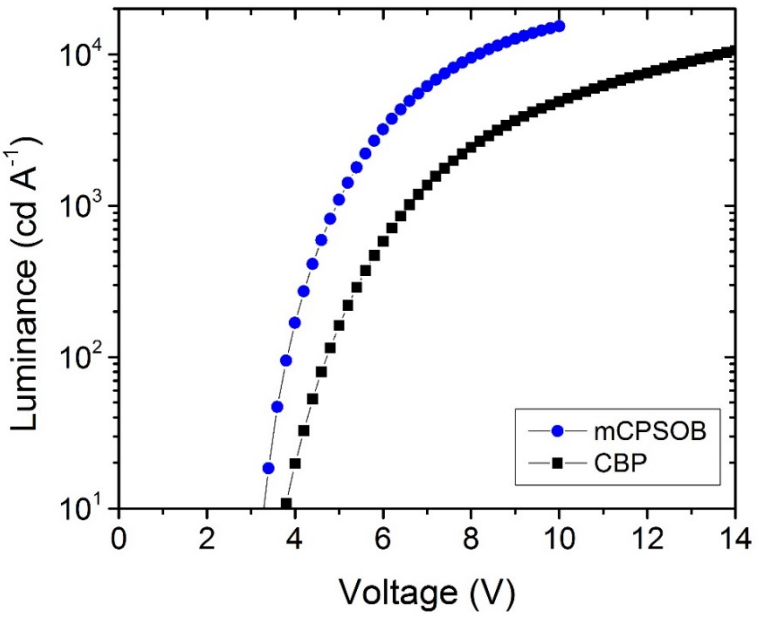

Figure 5.3 Luminance versus voltage for mCPSOB- and CBP-based OLEDs.

Table 8 Average values and standard deviation of mCPSOB:4CzIPN and CBP:4CzIPN devices measured over five devices.

Host	V_{ON} (V)	EQE* (%)	EQE_{1000} (%)	Current Efficacy* (cd/A)	Power Efficacy* (Lm/W)
mCPSOB	3.2	26.5 ± 0.5	21.5 ± 0.6	81 ± 2	79 ± 2
CBP	3.8	8 ± 3	13 ± 2	25 ± 8	20 ± 7

*Indicates values at turn-on voltage

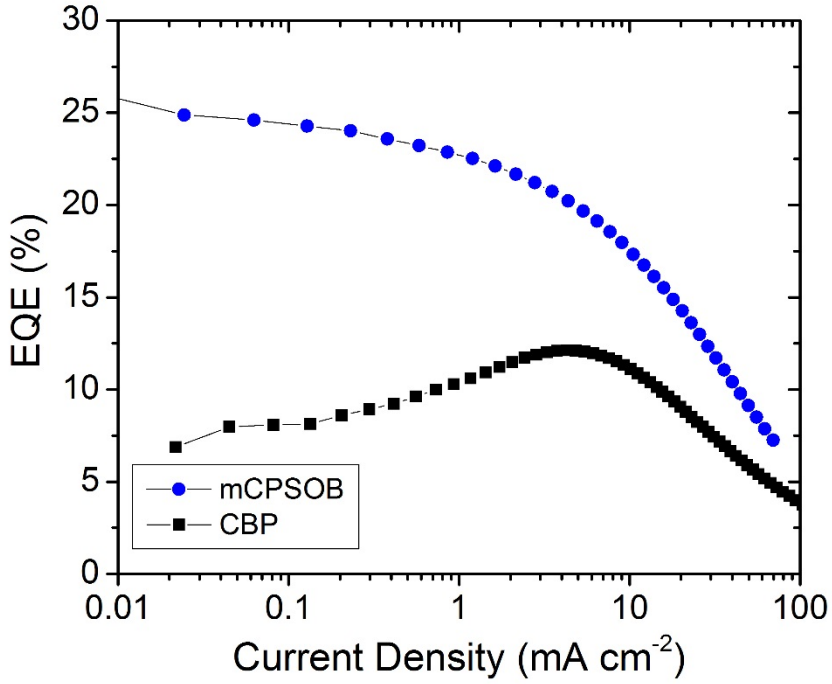

Figure 5.4 EQE versus current density for mCPSOB- and CBP-based OLEDs.

Comparing these results to those obtained in OLEDs based on a CBP host matrix revealed a substantial improvement in the TADF OLEDs in both overall efficiency and roll-off. CBP:4CzIPN devices showed an EQE of 8.2% at 10 cd/m^2, and 12.6% at 1,000 cd/m^2, with an increased turn-on voltage of 3.8V compared to 3.2V for mCPSOB:4CzIPN

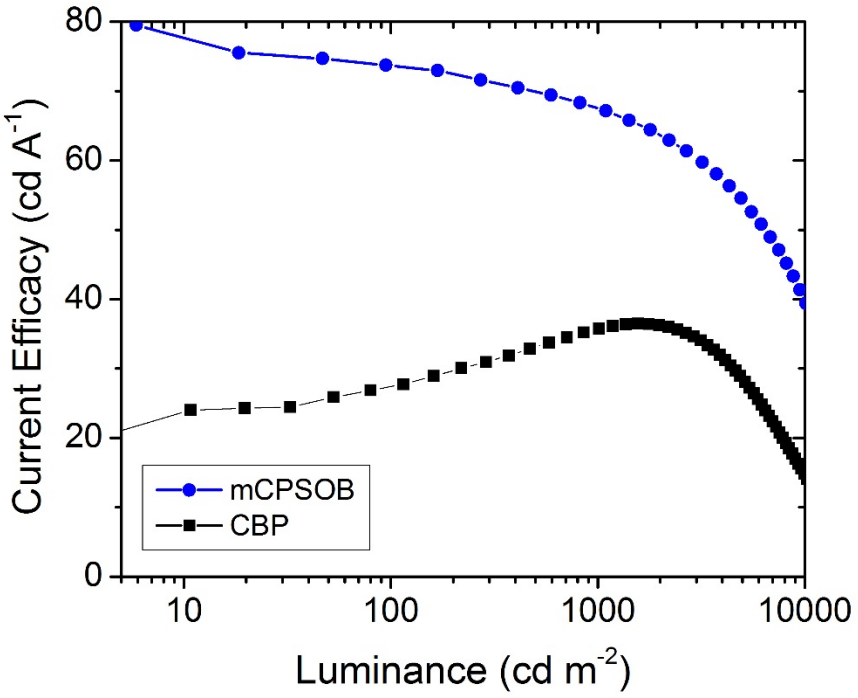

Figure 5.5 Current efficacy versus luminance for mCPSOB- and CBP-based OLEDs.

devices. It is also worth pointing out the roll-off performance between the two host materials shown in Figure 5.5. Unlike CBP, the mCPSOB devices show a peak EQE at the turn-on voltage, indicating a favorable charge-balance in the EML in these devices even at low current densities.

Energetically, the IE and EA (or HOMO/LUMO energies) for mCPSOB, CBP and 4CzIPN were estimated to be 5.8 eV and 2.5 eV, 6.1 eV and 2.8 eV [31], and 5.8 eV and 3.4 eV [31], respectively, using cyclic voltammetry and absorption onset. These estimations suggest that energetic alignment between the mCPSOB host material and 4CzIPN molecules is improved compared to that between CBP and 4CzIPN, facilitating charge transfer from the host to the emissive molecules and consequently device performance. Moreover, the mCPSOB devices showed a very-low efficiency roll-off at

high luminance values, maintaining an EQE > 22% at 1,000 cd/m^2, compared to 9.2% at 1,000 cd/m^2 for the CBP device. This high efficiency over such a broad range could be attributed to the suppression of the triplet exciton quenching processes due to the high triplet level of the host material mCPSOB (E_T = 3.02 eV) compared to the singlet energy of the emitter 4CzIPN (E_S = 2.43 eV), as well as mCPSOB's ability to maintain charge balance across larger range of applied biases compared to CBP. A high triplet energy would lead to efficient energy transfer between the mCPSOB and 4CzIPN, and contributes to the high performance of these devices. Additionally, it has been reported by other groups that ambipolar hosts may allow for the broadening of the recombination zone in the EML away from the EML/ETL or EML/HTL interface, further improving the device efficiency and reducing the exciton density across the EML [28]. These groups report that devices with narrow recombination zones tend to lead to greater triplet-triplet annihilation and steeper efficiency roll-off at high current densities due to an accumulation of triplet excitons [26, 49, 50]. Our mCPSOB:4CzIPN device results support these claims that the ambipolar charge properties of host materials help maintain charge balance across a broad region within the EML at high current densities [26, 28] and can be extended to TADF emitters. These material properties are crucial to the design of highly efficient OLEDs and will be needed in order for TADF based devices to compete with phosphorescent OLEDs.

5.2.2 Blue TADF Results

These results can be extended to suit the blue-emitting guest 2CzPN. Unlike CBP (and other common high efficiency host materials), mCPSOB has a triplet energy > 3.0 eV, which makes is compatible with blue (and even deep-blue) emitters. The triplet energy for 2CzPN was measured to be 2.6 eV [53], and the optimized device structure provided above

for the green-emitting material 4CzIPN can be used as a template for 2CzPN. This modified device structure and the chemical structure for 2CzPN are provided below in Figure 5.6.

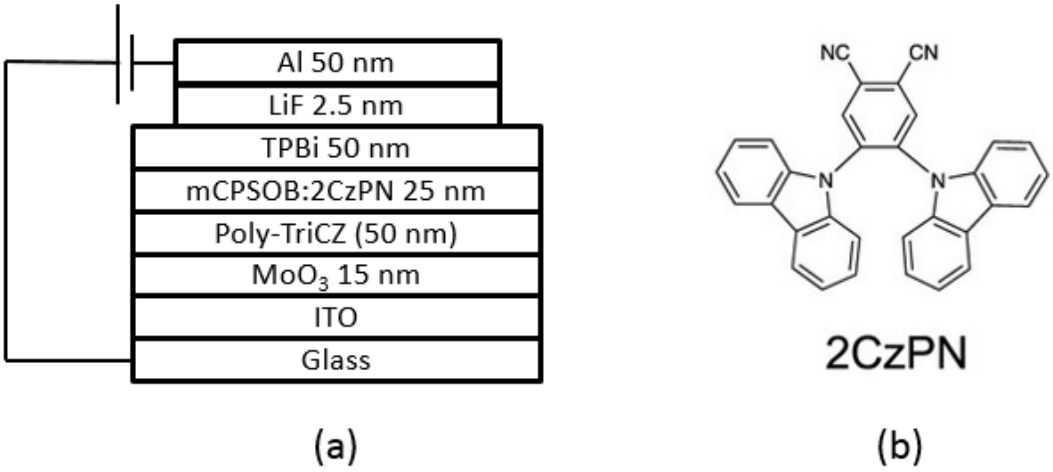

Figure 5.6 (a) Device structure for blue-emitting TADF OLED (b) Chemical structure for blue-emitting dopant 2CzPN

mCPSOB was co-deposited with 2CzPN at a concentration of 0.94:0.06. The results for these devices are provided below in Figures 5.7 and 5.8, with key performance metrics highlighted in Table 9.

Table 9 Average values and standard deviation of mCPSOB:2CzPN devices measured over five devices.

Host	V_{ON} (V)	EQE* (%)	EQE_{1000} (%)	Current Efficacy* (cd/A)	Power Efficacy* (Lm/W)
mCPSOB	3.0	22.0 ± 0.4	5.1 ± 0.4	53.8 ± 1	56.4 ± 1

*Indicates values at turn-on voltage

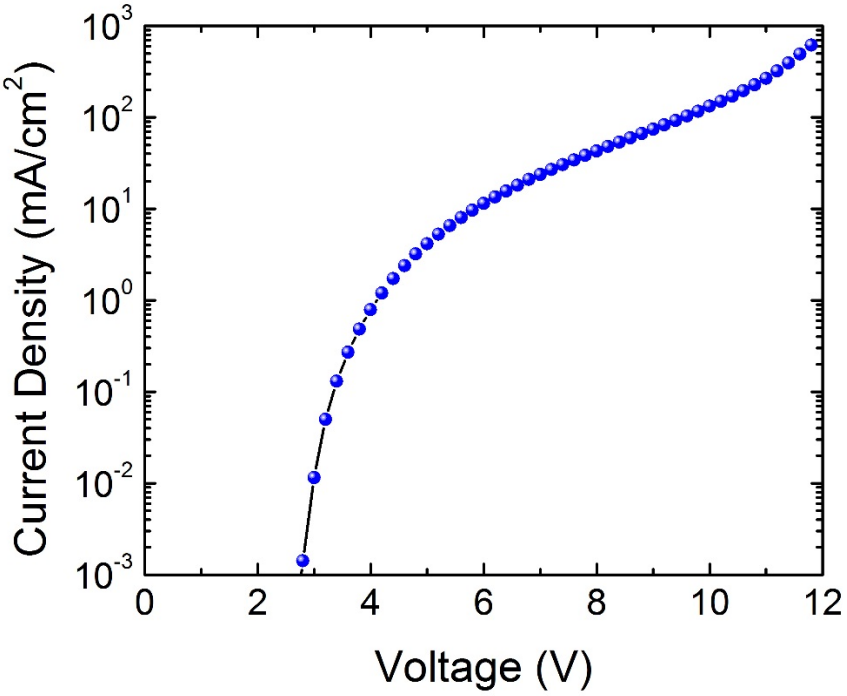

Figure 5.7 Current density versus voltage for mCPSOB:2CzPN blue-emitting OLEDs.

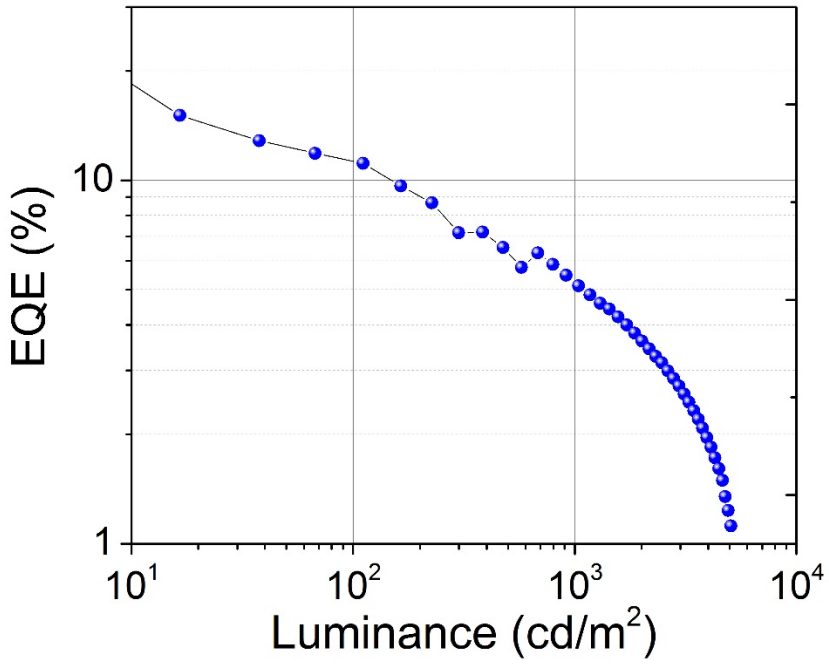

Figure 5.8 EQE versus luminance for mCPSOB:2CzPN blue-emitting OLEDs.

These results represent the most efficient blue-emitting OLED from TADF dopants, and were obtained simply by replacing the dopant in the simplified OLED structure presented in this thesis with 2CzPN. It is worth noting that these results are from an un-optimized device structure – these results can be further improved by modifying the dopant concentration in the EML, introducing exciton blocking layers between the ETL and EML, or through the use of thin interlayers to reduce the energetic barriers present between organic semiconductor materials. Addressing these concerns should help reduce the efficiency roll-off that has been an intrinsically limiting factor with these blue dopants.

Conclusion

In conclusion, highly efficient OLEDs based on TADF were fabricated usingthe simplified three-layer OLED device structure that utilizes the novel ambipolar host material mCPSOB and polymeric HTL Poly-TriCZ. By simply replacing the dopant material in the EML matrix, we were able to produce state-of-the-art efficiencies with both green- (4CzIPN) and blue- emitting (2CzPN) TADF emitters. These devices showed superior performance compared to those reported in the literature, with a maximum EQE of 26.5% at 10 cd/m^2 and 21.5% at 1,000 cd/m^2 for the green-emitting devices, and a maximum EQE of 22.0% at 10 cd/m^2 and 5.1% at 1,000 cd/m^2 for the blue-emitting devices. These results are not only amongst the highest ever reported for TADF OLEDs, but phosphorescent OLEDs as well.

CHAPTER 6

Organic Light-Emitting Diodes on Shape Memory Polymer Substrates for Flexible and Wearable Electronics

In this chapter, green-emitting electrophosphorescent organic light-emitting diodes (OLEDs) with inverted top-emitting structures are demonstrated on bio-compatible shape memory polymer (SMP) substrates for wearable electronic applications. The combination of the unique properties of SMP substrates with the light-emitting properties of OLEDs pave to the way for new applications, including conformable smart skin devices, minimally invasive biomedical devices, and flexible lighting/display technologies. In this work, SMPs were designed to exhibit a considerable drop in modulus when a thermal stimulus is applied, allowing the devices to bend and conform to new shapes when its glass transition temperature is reached. The results shown define the state-of-the-art in performance for light-emitting sources on conformable and/or deformable substrates.

6.1 Inverted Top-Emitting OLED Design

In recent reports, our group was able to discover a strategy to design efficient inverted top-emitting OLEDs that produced state-of-the-art current efficacy values of over 200 cd/A at 1,000 cd/m^2 [137]. In an inverted device structure, the anode and cathode are in 'inverted' positions, and a bottom vacuum-deposited cathode is now the first layer on the substrate. We discovered that electrons could be efficiently injected from this bottom-cathode if it was in contact with electron-transport materials with high electron mobility. Because the bottom electrode was no fully reflective, a top-anode was designed as an

alternate to ITO. It is possible to deposit ITO on-top of the device to provide a transparent anode, but this technique is very high-temperature and damages the underlying temperature sensitive organic materials and results in the degradation of the device. For these devices, a design choice is made to deposit a 15 nm-thick layer of MoO_3 as an HIL with a semitransparent 20 nm-thick Au anode. Transition-metal oxides, such as WO_3, V_2O_5, and MoO_3 have been used to make very effective HILs. They provide the additional benefits of being stable, low-cost, and easily processed through VTE [138]. When deposited on an anode, MoO_3 has been shown to strongly modify the anode's work function. For instance, the deposition of 1.6 nm of MoO_3 on ITO has been shown to increase the work function of ITO from 4.4 eV to nearly 6.9 eV [139]. This is because the EA of MoO_3 is 6.7 eV and the material is strongly *n*-type, with its Fermi level very close to its conduction band.

A thin layer of Au was chosen as the anode for both its high work function (5.1 eV [140]) and the reduced damage depositing it by VTE causes when compared to depositing ITO by radio frequency magnetron sputtering. The thickness was chosen to be 20 nm to simultaneously provide sufficiently high conductivity and high transmittance. The transmittance of MoO_3 and Au on glass is shown in **Error! Reference source not found.**. Across the visible wavelengths, the glass substrate has a high transmittance of 95% and a 15 nm MoO_3 layer on glass maintains a transmittance of about 90%. When 20 nm of Au is deposited on the MoO_3, the transmittance drops below 50% in the blue wavelengths. An undesired consequence of this device structure is a weak micro-cavity effect between the electrodes. This often leads to spectral narrowing and blue shifting of the device spectrum when viewed off-axis [141].

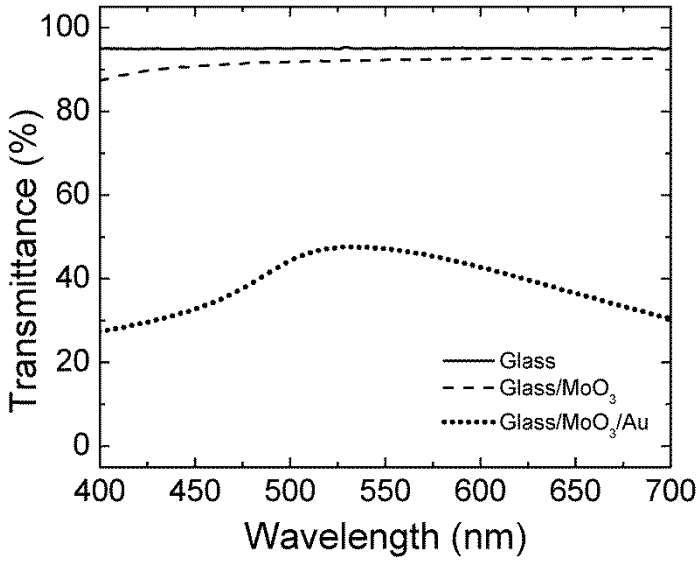

Figure 6.1 Transmission of the glass substrate, Glass/MoO3 (15 nm), and Glass/MoO_3 (15 nm)/Au (20 nm).

This device architecture allows for easy fabrication on flexible substrates. Unlike conventional bottom-emitting devices and devices have been successfully fabricated on flexible polymer substrates [such as polyethersulfone (PES)] and on recyclable nanocellulose/glycerol substrates in the past, which allowed for a limited deformation [137]. However, in order to fabricate solid-state lights and displays on truly conformable and deformable substrates, it is necessary to turn to a different group of substrates. In this chapter, we extend this work and demonstrate the most efficient OLED produced on a shape-memory polymer (SMP) substrate for flexible and conformable wearable electronic applications.

6.2 Review of Light-Emitting Devices on SMP Substrates

SMPs are mechanically active, smart materials that have the unique ability to change modulus once an external stimulus is applied (such as temperature, electric

potential, light, etc.) [137]. These stimuli allow the SMP substrate to exhibit a considerable drop in its modulus, after which the SMP rapidly softens to a rubbery state with a modulus up to three orders of magnitude lower than its original, glassy state. In this new rubbery state, the SMP can be easily deformed by external stresses into a temporary geometric configuration that can be retained even after the stress is removed by cooling the SMP to below T_g. Reheating the SMP causes strain relaxation within the polymer network and induces recovery of its original shape. These substrates have made a sizeable impact in solving neural interface issues for neural recording and stimulation applications [137] since the 'softened' state of the SMP has an elastic modulus that approaches that of human tissue.

The secret behind these materials lies in their molecular network structure, which contains at least two separate phases. The phase showing the highest thermal transition is the temperature that must be exceeded to establish the physical cross-links responsible for the permanent shape. The switching segments, on the other hand, are segments with the ability to soften past a certain transition temperature and are responsible for the temporary shape. Low cure stresses are present in the final polymer film because there is less volumetric shrinkage and delayed gelation, which leads to a highly uniform and dimensionally stable polymer film. These unique mechanical properties can also be extended to a new branch of electronic device applications. The combination of these unique SMP properties with the light-emitting properties of OLEDs paves the way to a new branch of applications, including: comfortable smart skin devices, minimally invasive biomedical devices and flexible, conformable, and wearable lighting/display devices.

Yu et al. first reported the development of polymer light-emitting diodes on SMP substrates by using a single-walled carbon nanotube/polymer composite electrode as an

indium tin oxide (ITO) replacement [137]. These devices produced a maximum current efficacy of 1.24 cd/A at 200 cd/m^2 with a turn-on voltage of 4.8 V, and a maximum luminance of 300 cd/m^2 (Figure 6.2).

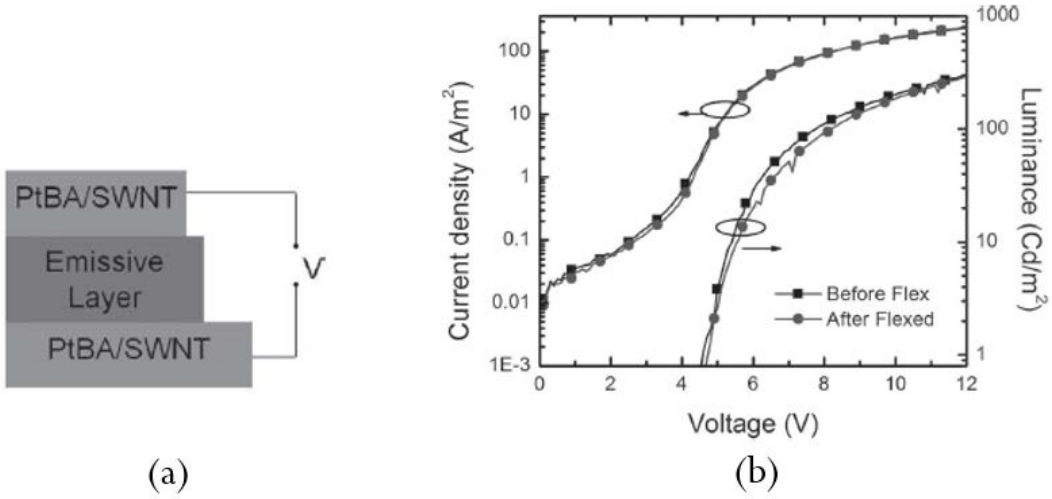

Figure 6.2 Polymer LED demonstration on SMP Substrates by Yu et al. (a) Device structure. (b) Current density vs. voltage and luminance vs. Voltage plots

6.3 Fabrication Details

6.3.1 SMP Substrate Synthesis

All polymer synthesis steps were performed in a fume hood. The substrates were fabricated using 1,3,5-triallyl-1,3,5-triazine-2,4,6(1*H*,3*H*,5*H*)-trione (TATATO), trimethylolpropane tris(3-mercaptopropionate) (TMTMP), and tricyclo[5.2.1.0^{2,6}]decanedimethanol diacrylate (TCMDA) purchased and used as received from Sigma–Aldrich. The chemical structures for these monomers are shown in Figure 6.3. The monomers were mixed in a glass vial in a stoichiometric ratio of alkene to thiol groups (TATATO and TMTMP), with a further addition of 30 wt. % TCMDA. Prior to curing, an additional 0.1 wt. % 2,2-Dimethoxy-2-phenylacetophenone (DMPA), as photoinitiator,

was dissolved in the solution using a fixed-speed vortex mixer. The solution was then placed in an ultrasonic cleaner for 5 minutes to remove any trapped gasses.

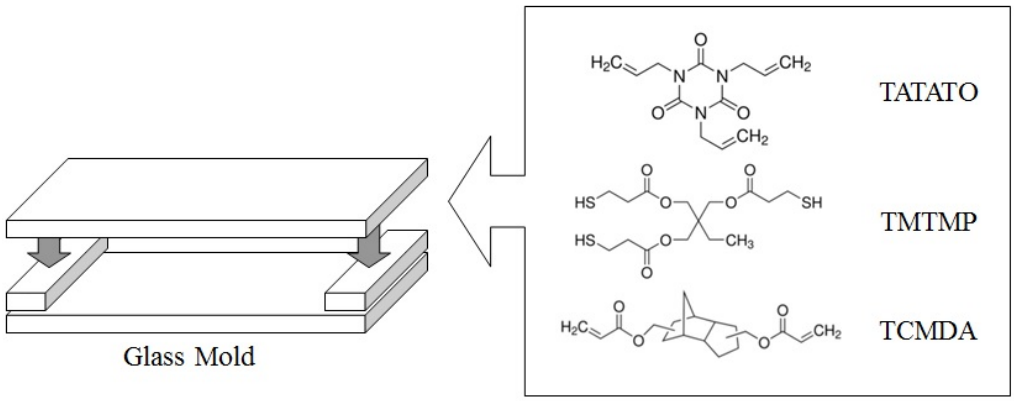

Figure 6.3 Graphical illustration of the mold used to fabricate SMP substrates. (Right) Chemical structure of monomers used in SMP synthesis.

Two clean glass microscope slides were cut to form a 1 × 1 inch mold area. The slides were cleaned by ultrasonication in acetone and isopropanol and blown dry with filtered nitrogen. The slides were then treated with two coats of a hydrophobic spray (Rain-X® Original Glass Treatment) to allow for the delamination of cured substrates. The slides were separated by glass spacers and clamped together to form a square mold with a thickness of approximately 1 mm. The monomer solution was injected to fill the mold using a glass Pasteur pipette. The solution was allowed to settle for 45 minutes and was cured under 365 nm UV light for 60 minutes. After curing, each polymer substrate was separated from its containing mold using a razor blade.

The cured substrates were exposed to oxygen plasma for 5 seconds. A film of poly(3,4-ethylenedioxythiophene)–polystyrene sulfonate (PEDOT:PSS Al 4083) was then deposited onto the substrates through a 0.45 µm polyvinylidene difluoride (PVDF) filter and spin coated at 5000 RPM for 60 s. Annealing was performed on a hot plate at 140 °C for 10 min.

6.3.2 OLED Fabrication

OLED substrates consisting of 1.0 mm-thick glass micro-slides (VWR international) and 500 µm-thick SMP substrates were cut into 1 x 1 inch squares. The glass slides were then cleaned by ultrasonication (5510, Branson Ultrasonics) for 25 min in each of the following: water with detergent, distilled water, acetone, and isopropanol. The SMP substrates were briefly rinsed with isopropanol. The substrates were then blown dry with nitrogen before exposed to oxygen plasma (Plasma-Preen II, Plasmatic Systems, Inc) for 5 min. PEDOT:PSS Al 4083 was dispensed onto the substrates through a 0.45 µm PVDF filter and spin-coated (WS-400B-6NPP/LITE, Laurell Technologies, Inc.) at a speed of 5000 rpm for 1 min. The PEDOT:PSS-coated substrates were heated on a hot plate at 140 °C for 10 min. The PEDOT:PSS layer was measured to have a thickness of 40 nm by spectroscopic ellipsometry (M-2000UI, J.A. Woollam Co., Inc.). When deposited on glass, PEDOT:PSS has been shown to improve the device yield and reliability of electron-dominated diodes. The PEDOT:PSS improves the wetting of the bottom aluminum electrode.

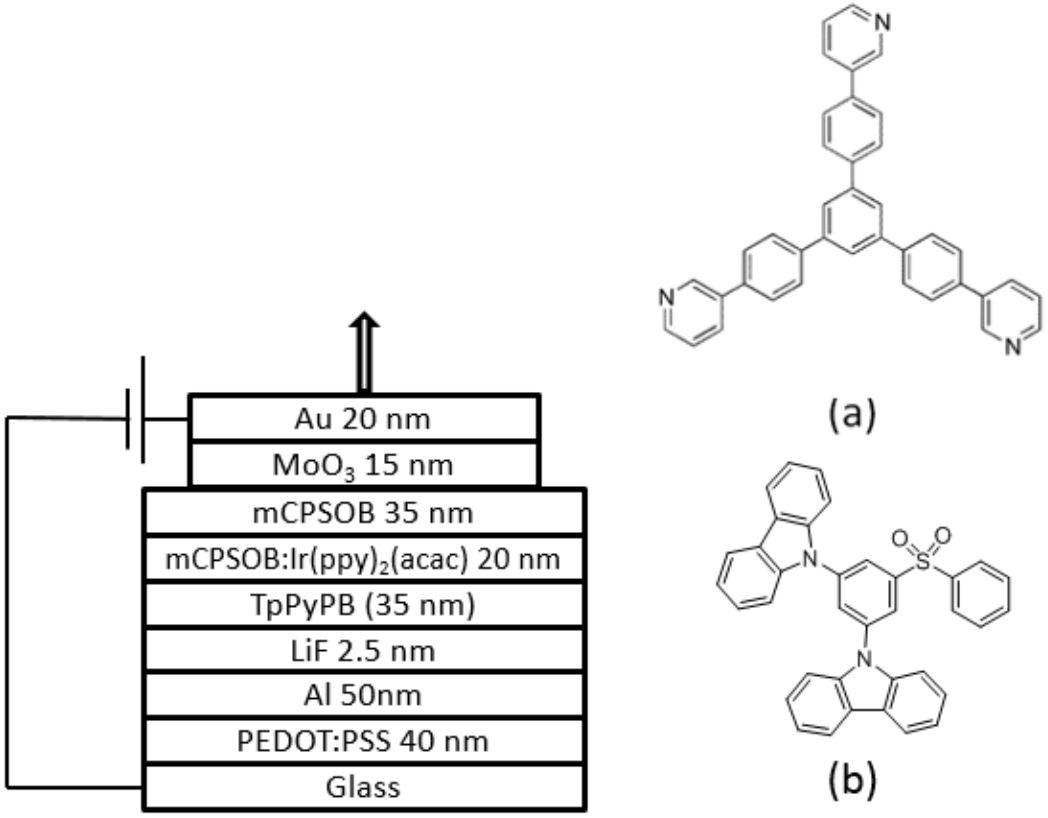

Figure 6.4 (Left) Device structure of the inverted top-emitting OLED using mCPSOB. (a) Chemical structure of electron-transporting material TpPyPB. (b) Chemical Structure of ambipolar host material mCPSOB.

The samples were then transferred to a high-vacuum thermal evaporation system (EvoVac, Armstrong Engineering Inc.). Once the chamber reached an ultra-high vacuum of $< 1.0 \times 10^{-7}$ Torr, a bottom 50 nm-thick aluminum cathode was deposited at a rate of 2.0 Å/s. To help facilitate electron injection, a 2.5 nm-thick lithium fluoride (LiF) layer was then deposited at a rate of 0.2 Å/s. The organic layers consisted of a bi-layer device structure to enhance charge injection/balance within the emissive layer. The bottom unit consisted of a 40 nm-thick electron transport layer of 1,3,5-tri(p-pyrid-3-yl-phenyl)benzene (TpPyPB). The emissive layer had a total thickness of 20 nm and consisted

of 3-(3,6-Di(carbazol-9-yl)carbazol-9-yl)-1-phenyl-sulfonylbenzene (mCPSOB) co-evaporated with 8% by volume of bis(2-phenylpyridine)(acetylacetonate)iridium(III) ($Ir(ppy)_2(acac)$), followed by a 35 nm-thick hole transport layer of mCPSOB. All organic layers were deposited at a rate of 1.0 Å/s. The top anode of the devices consists of a 15 nm-thick hole injection layer of molybdenum trioxide (MoO_3) that was deposited at a rate of 0.2 Å/s and a semitransparent 20 nm-thick top Au anode that was deposited at a rate of 2.0 Å/s. The active area of all the OLEDs is 4.2 x 3.6 mm^2. TpPyPB and $Ir(ppy)_2(acac)$ were purchased from Luminescence Technology Corporation (Lumtec). mCPSOB was synthesized as in Chapter 4. All other materials were purchased from Sigma-Aldrich. All organic materials were purified by gradient zone sublimation prior to thermal evaporation.

6.4 Device Results

6.4.1 SMP Substrate Mechanical Properties

The SMP synthesis highlighted above utilizes the advantages of thiol-ene reactions (click reactions). Low cure-stresses are present in the final polymer due to the nature of the step-growth mechanism in this polymerization, which results in highly uniform/dimensionally stable polymer networks with low shrinkage and surface roughness, as well as strong adhesion to metal layers [137]. More significantly, this allows for various material properties (such as T_g, rubbery modulus and hydrophobicity) to be altered by controlling the concentration of the constituting monomers [137]. The T_g of the SMP substrate shown here was tuned by varying the concentration of TCMDA added to the polymer solution prior to curing. A network consisting of TATATO and TMTMP with a 30 mol % of TCMDA was shown to provide a T_g above room temperature to facilitate

device fabrication and testing, while maintaining the low cure-stress paradigm of the thiol-ene reaction. Dynamic mechanical analysis (DMA) was performed on these samples to characterize their storage modulus as a function of temperature. These measurements were performed on a Metter Toledo DMA 861e/SDTA. Figure 6.5 shows the shear dynamic mechanical response of the synthesized system of polymers. T_g by DMA is denoted by the peak of the tangent delta curve, which is shown to be 43 °C for this network. It has been shown that the T_g of the substrate will increase with increasing diacrylates mol %, but the shear modulus below these transition temperatures will remain relatively unchanged [137].

6.4.2 OLED Performance Results

The device structure for the OLED used in these experiments is shown in Figure 6.2, along with the chemical structures for the host/hole transport material mCPSOB and electron transport material TpPyPB. Like CBP, mCPSOB was designed to exhibit ambipolar mobility properties but with an emphasis on a high T_g (> 140 °C compared to CBP 62 °C). This high T_g helps produce thermally and morphologically stable films, which prevents mCPSOB from crystallizing during operation and reduces the possibility of phase separation upon heating of the device, increasing its operational stability [137]. For these

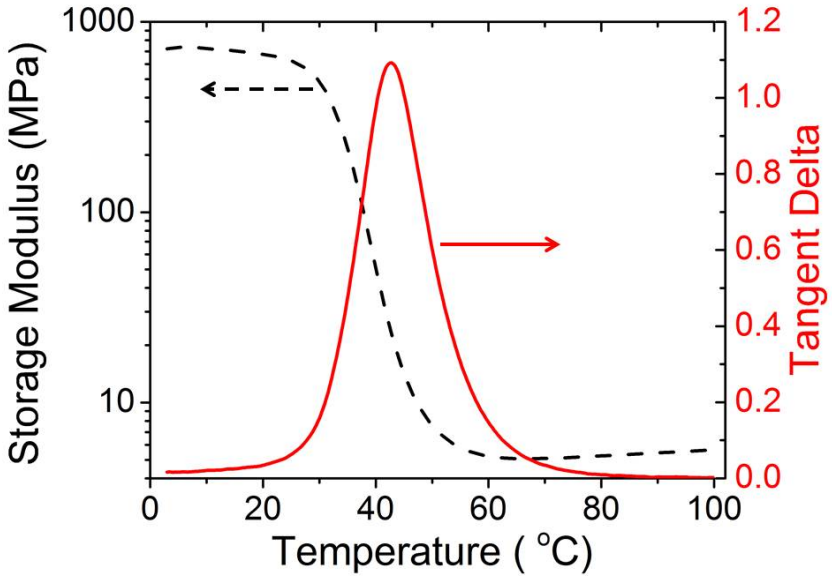

Figure 6.5 Shear dynamic mechanical response of the synthesized SMP substrate. Black dotted line represents storage modules (MPa) versus temperature (°C). Red solid line represents tangent delta versus temperature (°C).

reasons, mCPSOB was chosen as the host/HTL material in the OLED stack to ensure the OLED was thermally stable enough to withstand the necessary thermal stimulus needed to exploit the unique properties of the SMP substrate. The ionization energy (IE) and the electron affinity (EA) were determined to have values of 5.5 eV and 2.2 eV, respectively, based on cyclic voltammetry and absorption experiments. This material also showed a high triplet energy of E_T = 2.98 eV, making it suitable host for the deep blue dopants needed to produce white OLEDs with high color rendering indices. In addition to the OLEDs fabricated on SMP substrates, a device on a glass reference substrate was also tested and used as a benchmark.

Figures 6.6 and 6.7 show the luminance versus voltage and current density versus voltage characteristics, respectively, for both devices. From the curves, it is apparent that

the OLEDs fabricated on the SMP substrates perform equally as well as those fabricated on glass, with a turn-on voltage of 3.6 V and 3.4 V, respectively. The turn-on voltage is defined here as the voltage needed to achieve a luminance of 10 cd/m^2.

Table 10 Average values and standard deviation of performance parameters of OLEDs fabricated on SMP and glass reference substrates measured over five devices.

	V_{ON} (V)	**Current Efficacy at 100 cd/m^2 (cd/A)**	**Power Efficacy at 100 cd/m^2 (lm/W)**	**Current Efficacy at 1,000 cd/m^2 (cd/A)**	**Power Efficacy at 1,000 cd/m^2 (lm/W)**
SMP Substrate	3.6	33 ± 3	27 ± 3	28 ± 5	18 ± 3
Glass Reference	3.4	25 ± 4	20 ± 3	23 ± 4	14 ± 3

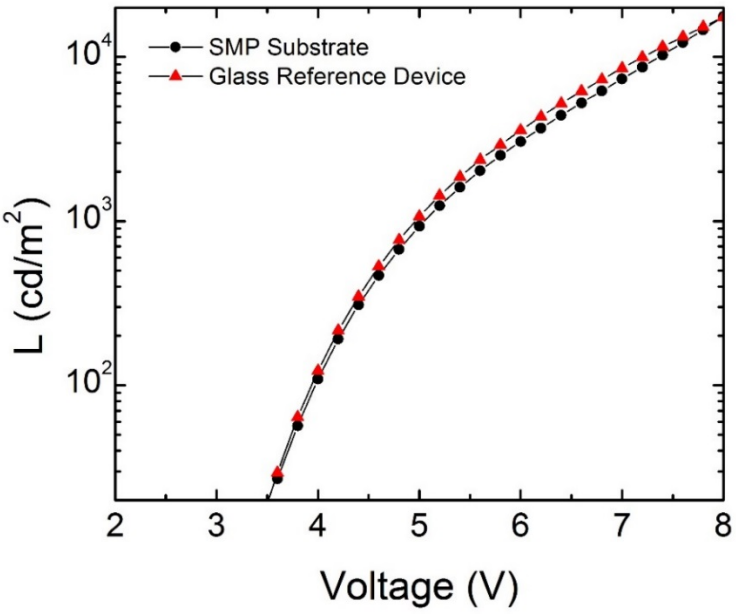

Figure 6.6 Luminance versus voltage for devices on SMP and glass substrates.

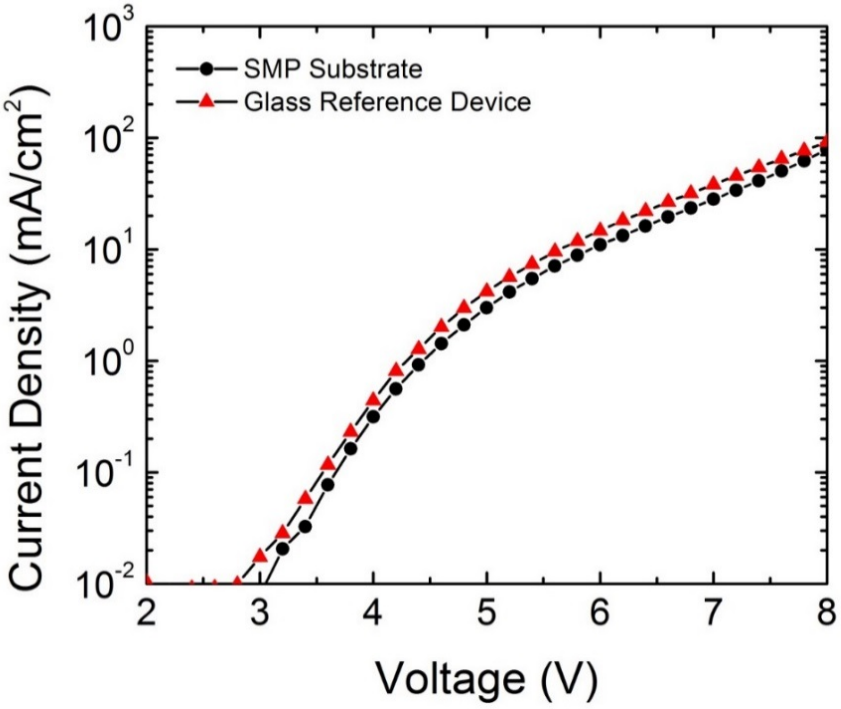

Figure 6.7 Current density versus voltage for devices on SMP and glass substrates.

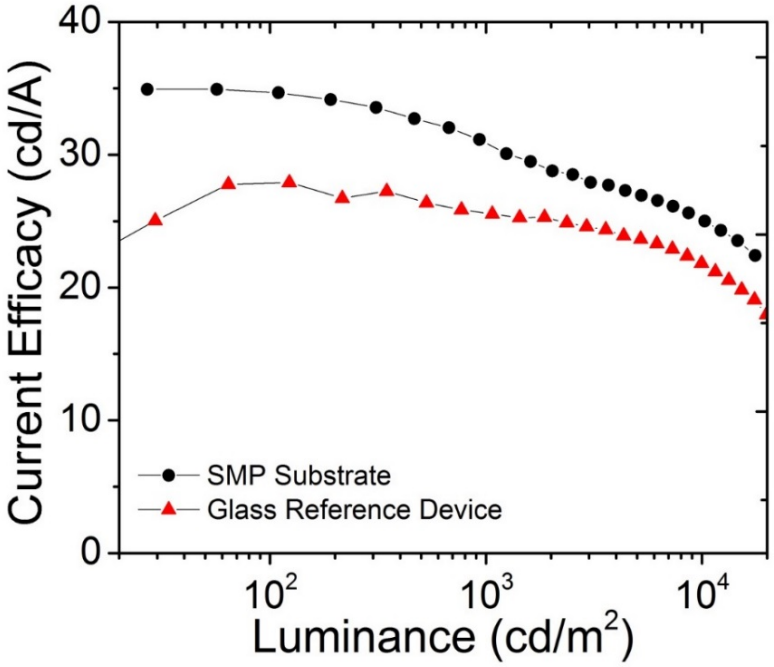

Figure 6.8 Current efficacy versus luminance for mCPSOB- and CBP-based OLEDs.

Both devices showed strong rectification, which indicates efficient carrier injection and balance at low applied biases and very little deviation in surface morphology between the SMP and glass substrates. The current efficacy versus luminance characteristics of both devices are shown in Figure 6.8, and Table 10 highlights the power efficacies of these devices at various luminance values with average values and standard deviations measured over five devices. While both devices exhibit similar diode characteristics, the OLEDs fabricated on the SMP substrates show superior performance to those on the glass reference slides, producing a maximum current efficacy of 33 cd/A at a luminance of 1,000 cd/m^2 when in its original, glass-like modulus, compared to 25 cd/A at 1,000 cd/m^2 for the glass reference device. We attribute this performance increase to the superior wetting abilities of the SMP substrate. It was shown in previous reports that PEDOT:PSS on glass improves the reliability of electron-dominated organic diodes, and increases the wetting ability of the aluminum on the glass substrate [137]. Because these SMP substrates are more hydrophobic than glass, we believe it provides for even better adhesion to the aluminum layers and, thus, a more uniform bottom cathode for the device. More comprehensive surface analysis on these layers/interfaces will be the focus of future work.

It is also worth noting the low efficacy roll-offs in these devices with the mCPSOB host material. This high efficiency over such a broad range could be attributed to the suppression of the triplet exciton quenching processes due to the high triplet level of the host material mCPSOB (E_T = 3.02 eV), as well as its ability to maintain charge balance across larger range of applied biases. A high triplet energy would lead to efficient energy transfer between the mCPSOB and Ir(ppy)$_2$(acac), and contributes to the high-performance of these devices. Additionally, it has been reported by other groups that ambipolar hosts

may allow for the broadening of the recombination zone in the EML away from the EML/ETL or EML/HTL interface, further improving the device efficiency and reducing the exciton density across the EML [28].

After the initial electrical characterizations, the OLED fabricated on the SMP substrates were placed on a hot-plate set at 45 °C for 60 s to allow for thermal stimuli to trigger the change in its elastic modulus. Once removed, the samples were manually re-shaped and softened into a curved form factor with a bending radius of 5 mm before being let to cool and return to its rigid elastic modulus. The electrical and optical properties of these re-shaped devices were re-characterized following this change in form factor. Figure 6.7 illustrates the normalized change in current efficacy between these reshaped devices compared to the initial, planar form. Although they show a significant performance drop at low luminance levels (100 cd/m^2), they perform equally as well when larger biases are applied and show great promise for applications that require high luminance values. These values are highlighted in Table 11. It is worth noting that these substrates were not fully pushed to limits where device degradation became present. These studies are the focus of current research and will be reported in future work. Figures 6.10 and 6.11 illustrate the softened SMP substrates curved with a radius of 5 mm and an illuminated device in this curved form. All the devices measured were able to withstand the initial heating, re-shaping and return to their original form factors. These tests successfully demonstrate the ability to thermally evaporate inverted top-emitting OLEDs on SMP substrates for flexible, conformable and deformable devices.

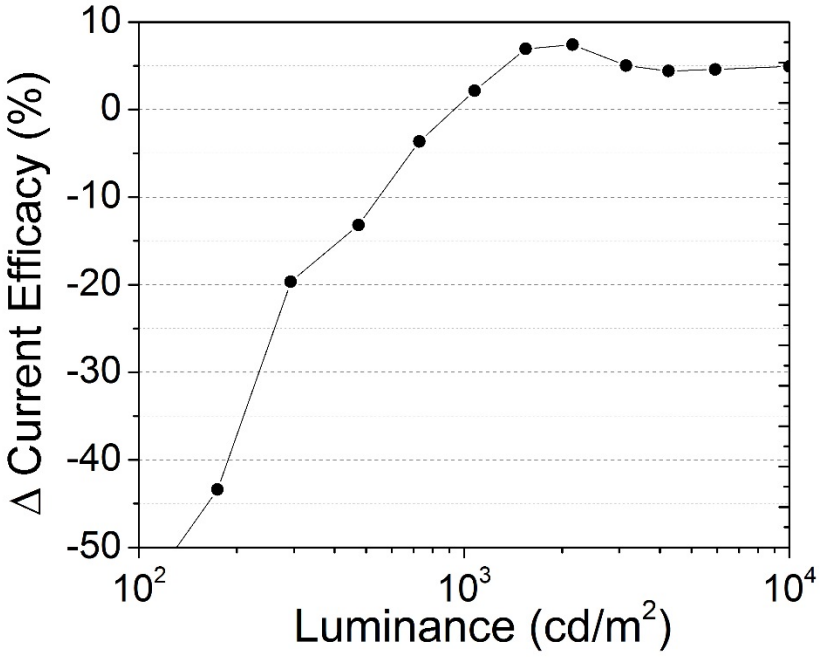

Figure 6.9 Normalized performance change in current efficacy vs. luminance between re-shaped SMP substrates and non-heated SMP substrates.

Table 11 Normalized performance change in current efficacy between re-shaped SMP substrates and non-heated SMP substrates at various luminance levels.

	100 cd/m^2	**1,000 cd/m^2**	**10,000 cd/m^2**
Re-Shaped Substrates	-43.4%	+2.2%	+4.9%

6.4.3 Conclusion

In conclusion, green phosphorescent inverted top-emitting OLEDs were demonstrated on SMP substrates. These devices employed a novel ambipolar host/HTL material with a high T_g value > 140 °C to yield films thermally and morphologically stable enough to withstand the thermal stimulation needed to trigger the change in elastic modulus for the SMP substrates. When compared to devices fabricated on glass reference substrates,

these OLEDs showed remarkably identical diode characteristics, but yielded higher current and power efficacy values of 33 cd/A and 21 lm/W, respectively, compared to 26 cd/A and 16 lm/W, respectively, at luminance values of 1,000 cd/m^2 and produced a maximum luminance over 30,000 cd/m^2. These results demonstrate an alternative method to fabricate flexible electronics using conformable substrates, and can be extended to a wide-range of potential applications ranging from bioengineering to flexible displays and lighting. The interfacial effects caused by the reshaping of the SMP substrate, as well as the lifetime of these devices, will be the focus of future work.

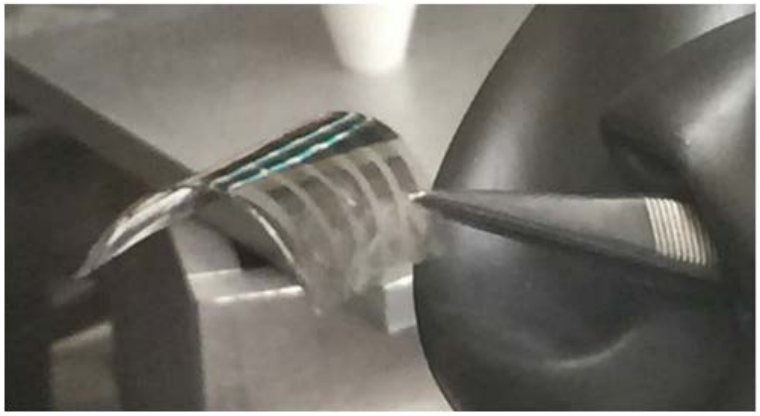

Figure 6.10 Curved SMP substrate after manual heating and manual bending.

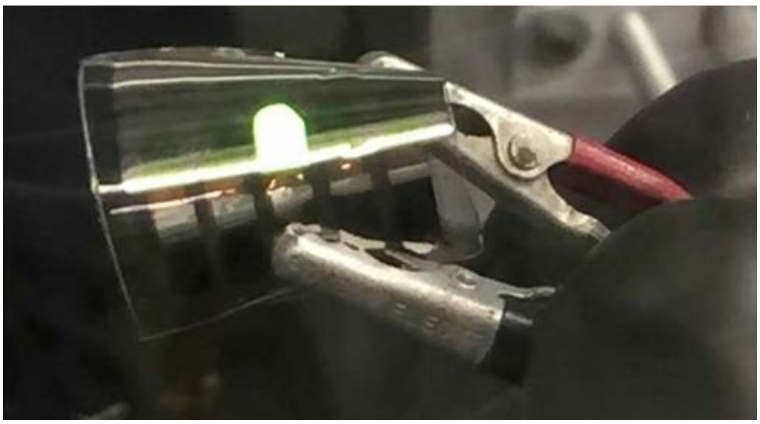

Figure 6.11 Curved SMP substrate with illuminated OLED

CHAPTER 7

Conclusions and Future Work

7.1 Conclusion

In conclusion, the work presented in this thesis reports on the design, fabrication and testing of state-of-the-art OLEDs in both conventional, bottom-emitting structures and inverted, top-emitting architectures. Both architectures utilize novel ambipolar host materials that improve charge balance in the EML of the device and can serve as universal host systems for deep blue, green or red dopant materials.

In Chapter 4, two novel materials were introduced: a polymeric HTL Poly-TriCZ and a small molecule host material mCPSOB. When used together, these materials were shown to produce state-of-the-art efficiencies with both green-emitting and blue-emitting dopants ($Ir(ppy)_3$ and FIrpic, respectively) in a simple, three-layer structure that produced results that defined the state-of-the art for blue electrophosphorescence with an EQE of 32.3% and a current efficacy of 80.2 cd/A at a luminance of 50 cd/m^2. More importantly, these devices experience reduced efficiency roll-off and still demonstrate and EQE and current efficacy of 21.5% and 53.5 cd/A at a luminance of 1,000 cd/m^2. The green-emitting devices produced an EQE and current efficacy of 28.2% and 103.4 cd/A, respectively, at a turn-on luminance of 40 cd/m^2. These result from these experiments provide a framework for developing high performance OLEDs.

In Chapter 5, these results were extended and used with the TADF emitters 4CzIPN (green-emitting) and 2CzPN (blue-emitting). The results demonstrated the state-of-the-art for both green and blue TADF OLEDs and provide further substance to our claim that the

Poly-TriCZ/mCPSOB sequence provides efficient charge balance and exciton confinement in the EML, regardless of the type of dopant (phosphorescent vs. TADF) or level of the triplet energy (blue vs. green). Green-emitting devices produced a maximum EQE and current efficacy of 26.5% and 81 cd/A, respectively, at a luminance of 20 cd/m^2; blue-emitting devices produced a maximum EQE and current efficacy of 22% and 55 cd/A, respectively, at 10 cd/m^2.

In Chapter 6, the ambipolar host material mCPSOB is demonstrated in an inverted top-emitted architecture and deposited on a SMP substrate. These devices produced current and power efficacy values of 33 cd/A and 21 lm/W, respectively, at luminance values of 1,000 cd/m^2, which is far greater than anything reported in the literature for light-emitting devices on SMP substrates (prior state-of-the-art was 1.24 cd/A). Moreover, these devices produced a maximum luminance of over 30,000 cd/m^2 and produced equal quality results after heating and deformation. These results prove that this technology can serve as an alternative method to fabricate flexible and deformable electronics, and can be extended to a wide-range of applications ranging from bioengineering to wearable electronics.

7.2 Recommendations for Future Work

Although much effort was put forth to investigate the work presented in this thesis, a complete understanding/characterization of these devices is laborious and not-practical to achieve in the scope of one Ph.D. thesis. Because of this, there are still many opportunities available for current (and future) students to better understand and improve upon this work. These opportunities include a better understanding of the roll-off behavior

in blue-emitting TADF devices, a comprehensive study of the mechanical properties of the SMP substrates and how OLEDs react to constant deformations, and lastly assessing their operational stability.

7.2.1 Blue-Emitting TADF OLEDs

Blue-emitting dopants all suffer from a similar roll-off behavior that worsens with increased applied bias. This trait adversely affects the performance and stability of these devices, and presents a great challenge for researchers to solve in order to make OLEDs a feasible alternative for next generation display and lighting technologies. Although great progress was made in addressing and understanding this issues in this work, more work needs to be done to further improve the efficiency roll-off. In particular, the use of ETL materials with high EAs and wide band-gaps are vital for efficient electron injection and exciton confinement in the EML. Moreover, the work presented in this thesis was solely focused on the blue-emitting material 2CzPN. There are other alternatives (both commercially available and novel from Prof. Seth Marder's group) that could provide better recombination and yield higher efficiencies. These materials need to be identified and screened using the optimized structures presented in this work. With this data, a greater understanding would be gained on the key design parameters needed for high performance blue-emitting TADF devices.

7.2.2 Mechanical Analysis of SMP Substrates

The use of SMPs for OLED substrates is an exciting project that has wide-reaching potential. This work has the ability to not only redefine the electronics industry, but also

make a sizeable impact in bioengineering and neurological testing. But before these breakthroughs can be made, we need to fully understand the mechanical properties of these substrates and how the OLEDs respond to continuous deformation. While we don't have the tools necessary to characterize this behavior in our lab, our partners at UT Dallas do and their involvement will be vital to fully understanding this behavior. Additionally, new monomer concentrations have yet to tried – these new concentrations can shift the T_g temperature of the substrate and modify the surface stress present in the rubber modulus phase of the substrate. Understanding this behavior and its effect on the OLED performance will be critical to elevating this technology/concept to the next level and could prove to be a very fruitful Ph.D. project for a future member of the group.

7.2.3 Device Lifetime

High performance devices are meaningless if they can't operate for an acceptable period of time. Because of this, a full understanding of the operational lifetime of all the devices presented in the work is necessary to understand the true significance of these results. The OLED community has assumed that materials with T_g temperatures > 100 °C are vital for operationally stable devices, but there have been few quantitative reports that fully investigated this issue. The work presented in this thesis had a strong focus on using materials with T_g temperatures > 100 °C, but their operational lifetime was not fully characterized. A comprehensive review of this hypothesis would provide answers to a lot of questions about effective OLED design and be a worthwhile project for future students.

Likewise, the operational lifetime of the OLEDs on SMP substrates was not investigated. The data in Chapter 6 highlighted a significant increase in the device

performance of OLEDs on SMP substrates compared to glass slides, and it will be worthwhile to further investigate the root cause of this performance increase and see if there is any correlation to operational lifetime. It is my believe that the SMP substrates have superior wetting abilities than glass (due to an increased surface energy) and allow the subsequent thermally evaporated layers to adhere better to its surface. This leads to better surface morphology between the organic layers, and a more stable/efficient device. However, this is purely a hypothesis and needs to be investigated in greater detail.

7.3 Publications and Conference Presentations

Michael P. Gaj, *et al.*, *"Organic Light-Emitting Diodes on Shape Memory Polymer Substrates for Wearable Electronics," Organic Electronics.* Vol. 25, pp. 151-155, 2015

Michael P. Gaj, Canek Fuentes-Hernandez, Yadong Zhang, Seth Marder, Bernard Kippelen**.,** *Highly efficient Organic Light-Emitting Diodes from thermally activated delayed fluorescence using a sulfone–carbazole host material.* Organic Electronics, 2015. 16(0): p. 109-112.

Yadong Zhang, **Michael P. Gaj**, Wojciech Haske, Seth Marder, Bernard Kippelen, *Ambipolar Charge Transporting Hosts with Sulfone and Carbazole Functional Moieties for Blue Phosphorescent Organic Light-Emitting Diodes.* Advanced Functional Materials, 2015. In Review.

Keith Knauer, Ehsan Najafabadi, Wojciech Haske, **Michael P. Gaj**, Kendal Davis, Canek Fuentes-Hernandez, Bernard Kippelen, *Stacked inverted top-emitting green electrophosphorescent organic light-emitting diodes on glass and flexible glass substrates.* Organic Electronics, 2013. 14(10): p. 2418-2423

(Poster Presentation Presentation) **Michael P. Gaj**, *et al.*, "Organic Light-Emitting Diodes for Next-Generation Wearable Electronics," FlexTech, Monterey, CA (2015).

(Poster Presentation) **Michael P. Gaj**, *et al.*, "High Performance Organic Light-Emitting Diodes from Thermally Activated Delayed Fluorescence," COPE Annual Industry Day, Atlanta, GA, (2015).

(Poster Presentation) **Michael P. Gaj**, *et al.*, "Organic Light-Emitting Diodes for Wearable Electronics," COPE Annual Industry Day, Atlanta, GA, (2015).

References

1. Tang, C.W. and S.A. Vanslyke, *Organic Electroluminescent Diodes.* Appl Phys Lett, 1987. **51**(12): p. 913-915.

2. Nelson, S.F., et al., *Temperature-independent transport in high-mobility pentacene transistors.* Applied Physics Letters, 1998. **72**(15): p. 1854-1856.

3. Hill, I.G., et al., *Molecular level alignment at organic semiconductor-metal interfaces.* Applied Physics Letters, 1998. **73**(5): p. 662-664.

4. Shen, Y., et al., *How to make ohmic contacts to organic semiconductors.* Chemphyschem, 2004. **5**(1): p. 16-25.

5. Adamovich, V.I., et al., *New charge-carrier blocking materials for high efficiency OLEDs.* Organic Electronics, 2003. **4**(2-3): p. 77-87.

6. Yun, C., et al., *Doping-Free Inverted Top-Emitting Organic Light-Emitting Diodes With High Power Efficiency and Near-Ideal Emission Characteristics.* IEEE Transactions on Electron Devices, 2012. **59**(1): p. 159-166.

7. Kulkarni, A.P., X. Kong, and S.A. Jenekhe, *High-Performance Organic Light-Emitting Diodes Based on Intramolecular Charge-Transfer Emission from Donor–Acceptor Molecules: Significance of Electron- Donor Strength and Molecular Geometry.* Advanced Functional Materials, 2006. **16**(8): p. 1057-1066.

8. Lee, Y.J., et al., *Study of thermal degradation of organic light emitting device structures by X-ray scattering.* Thin Solid Films, 2007. **515**(14): p. 5674-5677.

9. Tsujimura, T., *OLED displays: Fundamentals and applications*. 1st Ed. ed. 2013, Hoboken, N.J.: Wiley. 256.

10. Kera, S., et al., *Impact of an interface dipole layer on molecular level alignment at an organic-conductor interface studied by ultraviolet photoemission spectroscopy.* Physical Review B, 2004. **70**(8): p. 085304.

11. *OLED Myths and Misunderstandings*. 2015 [cited 2016 January 5]; Available from: http://www.oled-a.org/images/pdfs/OLED%20Myths.

12. Forrest, S.R., *The road to high efficiency organic light emitting devices.* Organic Electronics, 2003. **4**(2-3): p. 45-48.

13. Chen, H.F., et al., *1,3,5-Triazine derivatives as new electron transport-type host materials for highly efficient green phosphorescent OLEDs.* Journal of Materials Chemistry, 2009. **19**(43): p. 8112-8118.

14. Chang, C.C., et al., *Highly efficient white organic electroluminescent devices based on tandem architecture.* Applied Physics Letters, 2005. **87**(25): p. 253501.

15. Goushi, K., et al., *Triplet exciton confinement and unconfinement by adjacent hole-transport layers.* Journal of Applied Physics, 2004. **95**(12): p. 7798-7802.

16. Okutsu, S., et al., *Molecular design of hole transport material with various ionization potential for organic light-emitting diode applications.* IEEE Transactions on Electron Devices, 1997. **44**(8): p. 1302-1306.

17. Bernanose, A., *Electroluminescence of organic compounds.* British Journal of Applied Physics, 1955: p. S54-S56.

18. Pope, M., P. Magnante, and H.P. Kallmann, *Electroluminescence in organic crystals.* Journal of Chemical Physics, 1963. **38**(8): p. 2042-2043.

19. Baldo, M.A., et al., *Highly efficient phosphorescent emission from organic electroluminescent devices.* Nature, 1998. **395**(6698): p. 151-154.

20. Wang, Z.B., et al., *Unlocking the full potential of organic light-emitting diodes on flexible plastic.* Nature Photonics, 2011. **5**(12): p. 753-757.

21. Bin, J.-K., N.-S. Cho, and J.-I. Hong, *New Host Material for High-Performance Blue Phosphorescent Organic Electroluminescent Devices.* Advanced Materials, 2012. **24**(21): p. 2911-2915.

22. Li, G.M., et al., *Very High Efficiency Orange-Red Light-Emitting Devices with Low Roll-Off at High Luminance Based on an Ideal Host-Guest System Consisting of Two Novel Phosphorescent Iridium Complexes with Bipolar Transport.* Advanced Functional Materials, 2014. **24**(47): p. 7420-7426.

23. Hung, L.S. and C.H. Chen, *Recent progress of molecular organic electroluminescent materials and devices.* Materials Science & Engineering R-Reports, 2002. **39**(5-6): p. 143-222.

24. Chen, S.F., et al., *Recent Developments in Top-Emitting Organic Light-Emitting Diodes.* Adv. Mater., 2010. **22**(46): p. 5227-5239.

25. Adachi, C., et al., *Endothermic energy transfer: A mechanism for generating very efficient high-energy phosphorescent emission in organic materials.* Applied Physics Letters, 2001. **79**(13): p. 2082-2084.

26. Tao, Y., C. Yang, and J. Qin, *Organic host materials for phosphorescent organic light-emitting diodes.* Chemical Society Reviews, 2011. **40**(5): p. 2943-2970.

27. Matsushima, T., K. Goushi, and C. Adachi, *Charge-carrier injection characteristics at organic/organic heterojunction interfaces in organic light-emitting diodes.* Chem. Phys. Lett., 2007. **435**(4-6): p. 327-330.

28. Murawski, C., K. Leo, and M.C. Gather, *Efficiency Roll-Off in Organic Light-Emitting Diodes.* Advanced Materials, 2013. **25**(47): p. 6801-6827.

29. Chaskar, A., H.F. Chen, and K.T. Wong, *Bipolar Host Materials: A Chemical Approach for Highly Efficient Electrophosphorescent Devices.* Advanced Materials, 2011. **23**(34): p. 3876-3895.

30. Kim, J.S., et al., *Electroluminescence emission pattern of organic light-emitting diodes: Implications for device efficiency calculations.* J Appl Phys, 2000. **88**(2): p. 1073-1081.

31. Adachi, C., et al., *Nearly 100% internal phosphorescence efficiency in an organic light-emitting device.* J Appl Phys, 2001. **90**(10): p. 5048-5051.

32. Huang, Q., et al., *Performance improvement of top-emitting organic light-emitting diodes by an organic capping layer: An experimental study.* J Appl Phys, 2006. **100**(6): p. 064507.

33. Moller, S. and S.R. Forrest, *Improved light out-coupling in organic light emitting diodes employing ordered microlens arrays.* J Appl Phys, 2002. **91**(5): p. 3324-3327.

34. Sun, Y. and S.R. Forrest, *Enhanced light out-coupling of organic light-emitting devices using embedded low-index grids.* Nat Photonics, 2008. **2**(8): p. 483-487.

35. Knauer, K.A., et al., *Stacked inverted top-emitting green electrophosphorescent organic light-emitting diodes on glass and flexible glass substrates.* Organic Electronics, 2013. **14**(10): p. 2418-2423.

36. Najafabadi, E., et al., *Highly efficient inverted top-emitting green phosphorescent organic light-emitting diodes on glass and flexible substrates.* Applied Physics Letters, 2012. **101**(2): p. 023304.

37. Najafabadi, E., et al., *Efficient organic light-emitting diodes fabricated on cellulose nanocrystal substrates.* Applied Physics Letters, 2014. **105**(6).

38. Wu, C.C., et al., *Advanced Organic Light-Emitting Devices for Enhancing Display Performances.* J. Disp. Technol., 2005. **1**(2): p. 248-266.

39. Uoyama, H., et al., *Highly efficient organic light-emitting diodes from delayed fluorescence.* Nature, 2012. **492**(7428): p. 234-+.

40. Adachi, C., T. Tsutsui, and S. Saito, *Blue Light-Emitting Organic Electroluminescent Devices.* Applied Physics Letters, 1990. **56**(9): p. 799-801.

41. Holmes, R.J., et al., *Blue organic electrophosphorescence using exothermic host-guest energy transfer.* Applied Physics Letters, 2003. **82**(15): p. 2422-2424.

42. Lee, J., et al., *Effects of triplet energies and transporting properties of carrier transporting materials on blue phosphorescent organic light emitting devices.* Applied Physics Letters, 2008. **93**(12).

43. Liu, Z.W., et al., *Band Alignment at Anode/Organic Interfaces for Highly Efficient Simplified Blue-Emitting Organic Light-Emitting Diodes.* Journal of Physical Chemistry C, 2010. **114**(39): p. 16746-16749.

44. Baldo, M.A., et al., *Very high-efficiency green organic light-emitting devices based on electrophosphorescence.* Applied Physics Letters, 1999. **75**(1): p. 4-6.

45. Kim, S.Y., et al., *Organic Light-Emitting Diodes with 30% External Quantum Efficiency Based on a Horizontally Oriented Emitter*. Advanced Functional Materials, 2013. **23**(31): p. 3896-3900.

46. *http://www.udcoled.com/*. 2014 [cited 2014 January 19].

47. Reineke, S., et al., *White organic light-emitting diodes with fluorescent tube efficiency.* Nature, 2009. **459**(7244): p. 234-U116.

48. Zhang, Y., et al., *Ambipolar Charge Transporting Hosts with Sulfone and Carbazole Functional Moieties for Blue Phosphorescent Organic Light-Emitting Diodes.* Advanced Functional Materials, 2015. **In Review**.

49. Cho, Y.J., K.S. Yook, and J.Y. Lee, *A Universal Host Material for High External Quantum Efficiency Close to 25% and Long Lifetime in Green Fluorescent and Phosphorescent OLEDs.* Advanced Materials, 2014. **26**(24): p. 4050-4055.

50. Im, Y. and J.Y. Lee, *Above 20% External Quantum Efficiency in Thermally Activated Delayed Fluorescence Device Using Furodipyridine-Type Host Materials.* Chemistry of Materials, 2014. **26**(3): p. 1413-1419.

51. Nakanotani, H., et al., *High-efficiency organic light-emitting diodes with fluorescent emitters.* Nature Communications, 2014. **5**.

52. Sun, J.W., et al., *A Fluorescent Organic Light-Emitting Diode with 30% External Quantum Efficiency*. Advanced Materials, 2014. **26**(32): p. 5684-+.

53. Hirata, S., et al., *Highly efficient blue electroluminescence based on thermally activated delayed fluorescence.* Nature Materials, 2015. **14**(3): p. 330-336.

54. Han, T.H., et al., *Extremely efficient flexible organic light-emitting diodes with modified graphene anode*. Nature Photonics, 2012. **6**(2): p. 105-110.

55. Park, J.W., D.C. Shin, and S.H. Park, *Large-area OLED lightings and their applications.* Semiconductor Science and Technology, 2011. **26**(3).

56. PolyIC. *PolyIC Website*. [cited 2008 June]; Available from: www.polyic.com.

57. GE. *General Electrics Website*. [cited 2008 June]; Available from: www.ge.com.

58. CIE, *Commission Internationale de l'Eclairage Proceedings, 1931*. 1932, Cambridge: Cambridge University Press.

59. Abkowitz, M., I. Chen, and J.H. Sharp, *Electron spin resonance of the organic semiconductor alpha-copper phtalocyanine.* Journal of Chemical Physics, 1968. **48**(10): p. 4561-4567.

60. Almeleh, N. and S.E. Harrison, *Trapping effects in the organic semiconductor triphenylene.* Journal of Physics and Chemistry of Solids, 1966. **27**(5): p. 893-901.

61. McGinnes, J., P. Corry, and P. Proctor, *Amorphous-semiconductor switching in melanins.* Science, 1974. **183**(4127): p. 853-855.

62. Shirakawa, H., et al., *Synthesis of electrically conducting organic polymers - halogen derivatives of polyacetylene, $(CH)_x$.* Journal of the Chemical Society-Chemical Communications, 1977(16): p. 578-580.

63. Kelley, T.W., et al., *Recent progress in organic electronics: Materials, devices, and processes.* Chemistry of Materials, 2004. **16**(23): p. 4413-4422.

64. O'Brien, D.F., et al., *Hole transporting materials with high glass transition temperatures for use in organic light-emitting devices.* Advanced Materials, 1998. **10**(14): p. 1108-1112.

65. Hung, W.Y., et al., *Employing ambipolar oligofluorene as the charge-generation layer in time-of-flight mobility measurements of organic thin films.* Applied Physics Letters, 2006. **88**(6): p. 064102.

66. Bozano, L., et al., *Temperature- and field-dependent electron and hole mobilities in polymer light-emitting diodes.* Applied Physics Letters, 1999. **74**(8): p. 1132-1134.

67. Coropceanu, V., et al., *Charge transport in organic semiconductors.* Chemical Reviews, 2007. **107**(4): p. 926-952.

68. Hung, L.S., C.W. Tang, and M.G. Mason, *Enhanced electron injection in organic electroluminescence devices using an Al/LiF electrode.* Applied Physics Letters, 1997. **70**(2): p. 152-154.

69. Cao, Y., et al., *Improved quantum efficiency for electroluminescence in semiconducting polymers.* Nature, 1999. **397**(6718): p. 414-417.

70. Yang, X.H., et al., *Highly efficient polymeric electrophosphorescent diodes.* Advanced Materials, 2006. **18**(7): p. 948-954.

71. Moon, J.-M., et al., *Enhancement of hole injection using ozone treated Ag nanodots dispersed on indium tin oxide anode for organic light emitting diodes.* Applied Physics Letters, 2007. **90**(16): p. 163516.

72. Pope, M. and C.E. Swenberg, *Electronic Processes in Organic Crystals and Polymers*. 2nd ed. 1999, New York: Oxford Science Publications.

73. Lu, J.P., et al., *High-efficiency multilayer polymeric blue light-emitting diodes using boronate esters as cross-linking linkages.* Journal of Materials Chemistry, 2006. **16**(6): p. 593-601.

74. Oxtoby, D.W., W.A. Freeman, and T.F. Block, *Chemistry: Science of Change*. 4th ed. 2003, Pacific Grove: Thomson-Brooks.

75. Charas, A., et al., *Use of cross-linkable polyfluorene in the fabrication of multilayer polyfluorene-based light-emitting diodes with improved efficiency.* Applied Physics Letters, 2006. **89**(14): p. 143519.

76. Bredas, J.L., et al., *Organic semiconductors: A theoretical characterization of the basic parameters governing charge transport.* Proceedings of the National Academy of Sciences of the United States of America, 2002. **99**(9): p. 5804-5809.

77. Langevin, P., *The ionisation of gases.* Annales de Chimie et de Physique, 1903. **28**: p. 289-384.

78. Wu, G.L., et al., *Synthesis and characterization of photo-crosslinkable polyfluorene with acrylate side-chains.* Journal of Applied Polymer Science, 2006. **100**(3): p. 2336-2342.

79. Sandee, A.J., et al., *Solution-processible conjugated electrophosphorescent polymers.* Journal of the American Chemical Society, 2004. **126**(22): p. 7041-7048.

80. Silveira, W.R. and J.A. Marohn, *Microscopic view of charge injection in an organic semiconductor.* Physical Review Letters, 2004. **93**(11): p. 116104.

81. Campbell, I.H. and B.K. Crone, *Characteristics of an organic light-emitting diode utilizing a phosphorescent, shallow hole trap.* Applied Physics Letters, 2006. **89**(17): p. 172108.

82. Bassler, H., *Charge transport in disordered organic photoconductors - a Monte-Carlo simulation study.* Physica Status Solidi B-Basic Research, 1993. **175**(1): p. 15-56.

83. Kimyonok, A., et al., *Norbornene-based copolymers with iridium complexes and bis(carbazolyl)fluorene groups in their side-chains and their use in light-emitting diodes.* Chemistry of Materials, 2007. **19**(23): p. 5602-5608.

84. Bacher, E., et al., *Synthesis and characterization of photo-cross-linkable hole-conducting polymers.* Macromolecules, 2005. **38**(5): p. 1640-1647.

85. Dedeian, K., et al., *Photophysical and electrochemical properties of heteroleptic tris-cyclometalated iridium(III) complexes.* Inorganic Chemistry, 2005. **44**(13): p. 4445-4447.

86. Evans, N.R., et al., *Triplet energy back transfer in conjugated polymers with pendant phosphorescent iridium complexes.* Journal of the American Chemical Society, 2006. **128**(20): p. 6647-6656.

87. Borsenberger, P.M., L. Pautmeier, and H. Bassler, *Charge transport in disordered molecular solids.* The Journal of Chemical Physics, 1991. **94**(8): p. 5447-5454.

88. Coropceanu, V., et al., *Charge transport in organic semiconductors.* Chemical Reviews, 2007. **107**(4): p. 926-952.

89. Miller, A. and E. Abrahams, *Impurity conduction at low concentrations.* Physical Review, 1960. **120**(3): p. 745-755.

90. Marcus, R.A., *Theory of oxidation-reduction reactions involving electron transfer.* Journal of Chemical Physics, 1956. **24**(5): p. 966-978.

91. Borsenberger, P.M., W.T. Gruenbaum, and E.H. Magin, *Hole transport in vapor deposited bis(ditolylaminostyryl)benzene.* Physica B-Condensed Matter, 1996. **228**(3-4): p. 226-232.

92. Sakanoue, K., et al., *A molecular orbital study on the hole transport property of organic amine compounds.* Journal of Physical Chemistry A, 1999. **103**(28): p. 5551-5556.

93. Yan, H., et al., *A polymer blend approach to fabricating the hole transport layer for polymer light-emitting diodes.* Applied Physics Letters, 2004. **84**(19): p. 3873-3875.

94. Parmenter, R.H. and W. Ruppel, *2-carrier space-charge-limited current in a trap-free insulator.* Journal of Applied Physics, 1959. **30**(10): p. 1548-1558.

95. Kamohara, I., M. Townsend, and B. Cottle, *Simulation of heterojunction organic thin film devices and exciton diffusion analysis in stacked-hetero device.* Journal of Applied Physics, 2005. **97**(1): p. 014501.

96. Chopra, N., et al., *Effect of the charge balance on high-efficiency blue-phosphorescent organic light-emitting diodes.* ACS Appl Mater Interfaces, 2009. **1**(6): p. 1169-72.

97. Thompson, M.E., P.E. Burrows, and S.R. Forrest, *Electrophosphorescence in organic light emitting diodes.* Current Opinion in Solid State & Materials Science, 1999. **4**(4): p. 369-372.

98. Beljonne, D., et al., *Charge-recombination processes in oligomer- and polymer-based light- emitting diodes: A molecular picture.* Journal of the Society for Information Display, 2005. **13**(5): p. 419-427.

99. Becker, R.S., *Theory and Interpretation of Fluorescence and Phosphorescence*. 1969, New York: Wiley Interscience.

100. Yoo, S., B. Domercq, and B. Kippelen, *Efficient thin-film organic solar cells based on pentacene/C_{60} heterojunctions.* Applied Physics Letters, 2004. **85**(22): p. 5427-5429.

101. Bassler, H., et al., *Models of organic light-emitting diodes.* Synthetic Metals, 1997. **91**(1-3): p. 173-179.

102. Zhang, X.W., et al., *Highly efficient polymer light-emitting diodes using color-tunable carbazole-based iridium complexes.* Chemical Physics Letters, 2006. **422**(4-6): p. 386-390.

103. Mark, P. and W. Helfrich, *Space-charge-limited currents in organic crystals.* Journal of Applied Physics, 1962. **33**(1): p. 205-215.

104. Peumans, P. and S.R. Forrest, *Very-high-efficiency double-heterostructure copper phthalocyanine/C_{60} photovoltaic cells.* Applied Physics Letters, 2001. **79**(1): p. 126-128.

105. Yi, C., et al., *Red to near-infrared electrophosphorescence from an iridium complex coordinated with 2-phenylpyridine and 8-hydroxyquinoline.* Inorganica Chimica Acta, 2007. **360**(11): p. 3493-3498.

106. Evans, R.C., P. Douglas, and C.J. Winscom, *Coordination complexes exhibiting room-temperature phosphorescence: Evaluation of their suitability as triplet emitters in organic light emitting diodes.* Coordination Chemistry Reviews, 2006. **250**(15-16): p. 2093-2126.

107. Lukosz, W., *LIGHT-EMISSION BY MULTIPOLE SOURCES IN THIN-LAYERS .1. RADIATION-PATTERNS OF ELECTRIC AND MAGNETIC DIPOLES.* Journal of the Optical Society of America, 1981. **71**(6): p. 744-754.

108. Baldo, M.A., C. Adachi, and S.R. Forrest, *Transient analysis of organic electrophosphorescence. II. Transient analysis of triplet-triplet annihilation.* Physical Review B, 2000. **62**(16): p. 10967-10977.

109. Lamansky, S., et al., *Molecularly doped polymer light emitting diodes utilizing phosphorescent Pt(II) and Ir(III) dopants.* Organic Electronics, 2001. **2**(1): p. 53-62.

110. Kulkarni, A.P., et al., *Efficient blue organic light-emitting diodes based on an oligoquinoline.* Applied Physics Letters, 2005. **86**(6): p. 061106.

111. *iPhone 6 Display Technology*. [cited 2016 January 15]; Available from: http://www.displaymate.com/iPhone6_ShootOut.htm.

112. *Apple iMac with Retina 5K Display Review*. 2014 [cited 2016 Jan 15]; Available from: http://www.macworld.co.uk/review/imac/retina-imac-in-depth-review-lab-test-3581076/.

113. *Samsung UE65JS9500 4K TV Review*. 2015 [cited 2016 Jan 15]; Available from: http://www.pocket-lint.com/review/135740-samsung-ue65js9500-4k-tv-review-high-dynamic-range-master.

114. Krummacher, B., et al., *Influence of charge balance and microcavity effects on resultant efficiency of organic-light emitting devices.* Organic Electronics, 2006. **7**(5): p. 313-318.

115. Bardsley, N. *Solid-State Lighting Research and Development*. 2014 [cited 2016; Available from: http://apps1.eere.energy.gov/buildings/publications/pdfs/ssl/ssl_mypp2014_web.

116. Lee, T.W., et al., *High-efficiency stacked white organic light-emitting diodes.* Applied Physics Letters, 2008. **92**(4): p. 043301.

117. Adachi, C., M.E. Thompson, and S.R. Forrest, *Architectures for efficient electrophosphorescent organic light-emitting devices.* IEEE Journal of Selected Topics in Quantum Electronics, 2002. **8**(2): p. 372-377.

118. Gather, M.C., A. Koehnen, and K. Meerholz, *White Organic Light-Emitting Diodes.* Advanced Materials, 2011. **23**(2): p. 233-248.

119. Orselli, E., et al., *Orange phosphorescent organic light-emitting diodes with high operational stability.* Organic Electronics, 2012. **13**(9): p. 1506-1510.

120. Wakimoto, T., et al., *Organic EL cells using alkaline metal compounds as electron injection materials.* IEEE Transactions on Electron Devices 1997. **44**(8): p. 1245-1248.

121. Wang, Z.B., et al., *Highly simplified phosphorescent organic light emitting diode with > 20% external quantum efficiency at > 10,000 cd/m(2).* Applied Physics Letters, 2011. **98**(7).

122. Fukase, A., et al., *High-efficiency organic electroluminescent devices using iridium complex emitter and arylamine-containing polymer buffer layer.* Polymers for Advanced Technologies, 2002. **13**(8): p. 601-604.

123. Thomschke, M., et al. *Highly efficient inverted top-emitting organic electroluminescent devices with doped charge transport layers*. Org Photonics IV, SPIE Proc., 2010. **7722**, 77220.

124. Tanaka, D., et al., *Ultra high efficiency green organic light-emitting devices.* Japanese Journal of Applied Physics Part 2-Letters & Express Letters, 2007. **46**(1-3): p. L10-L12.

125. Ikai, M., et al., *Highly efficient phosphorescence from organic light-emitting devices with an exciton-block layer.* Applied Physics Letters, 2001. **79**(2): p. 156-158.

126. Milliron, D.J., et al., *Surface oxidation activates indium tin oxide for hole injection.* Journal of Applied Physics, 2000. **87**(1): p. 572-576.

127. Choi, J.H., et al., *Work function increase of indium-tin-oxide surfaces by atmospheric air plasma treatment with steady-state airflow.* Journal of Vacuum Science & Technology A: Vacuum, Surfaces, and Films, 2005. **23**(5): p. 1479-1482.

128. Steuber, F., et al., *Reduced operating voltage of organic electroluminescent devices by plasma treatment of the indium tin oxide anode.* Applied Physics Letters, 1999. **74**(23): p. 3558-3560.

129. Elschner, A., et al., *PEDT/PSS for efficient hole-injection in hybrid organic light-emitting diodes.* Synthetic Metals, 2000. **111**: p. 139-143.

130. Patel, N.K., S. Cinà, and J.H. Burroughes, *High-efficiency organic light-emitting diodes.* Ieee Journal of Selected Topics in Quantum Electronics, 2002. **8**(2): p. 346-361.

131. de Jong, M.P., L.J. van Ijzendoorn, and M.J.A. de Voigt, *Stability of the interface between indium-tin-oxide and poly(3,4-ethylenedioxythiophene)/poly(styrenesulfonate) in polymer light-emitting diodes.* Applied Physics Letters, 2000. **77**(14): p. 2255-2257.

132. Zhang, S.T., et al., *Electron blocking and hole injection: The role of N,N'-bis(naphthalen-1-y)-N,N'-bis(phenyl)benzidine in organic light-emitting devices.* Applied Physics Letters, 2004. **84**(15): p. 2916-2918.

133. Malliaras, G.G. and J.C. Scott, *The roles of injection and mobility in organic light emitting diodes.* Journal of Applied Physics, 1998. **83**(10): p. 5399-5403.

134. Nakanotani, H., et al., *Promising operational stability of high-efficiency organic light-emitting diodes based on thermally activated delayed fluorescence.* Scientific Reports, 2013. **3**: p. 2127.

135. Endo, A., et al., *Efficient up-conversion of triplet excitons into a singlet state and its application for organic light emitting diodes.* Applied Physics Letters, 2011. **98**(8): p. 083302.

136. Endo, A., et al., *Thermally activated delayed fluorescence from $Sn4^{+}$-porphyrin complexes and their application to organic light-emitting diodes - a novel mechanism for electroluminescence.* Advanced Materials, 2009. **21**(47): p. 4802-4806.

138. Wang, Z.B., et al., *Analysis of charge-injection characteristics at electrode-organic interfaces: Case study of transition-metal oxides.* Physical Review B, 2009. **80**(23): p. 235325.

139. Kröger, M., et al., *Role of the deep-lying electronic states of MoO_3 in the enhancement of hole-injection in organic thin films.* Applied Physics Letters, 2009. **95**(12): p. 123301.

140. Michaelson, H.B., *Work function of elements and its periodicity.* Journal of Applied Physics, 1977. **48**(11): p. 4729-4733.

141. Hofmann, S., et al., *Top-emitting organic light-emitting diodes: Influence of cavity design.* Applied Physics Letters, 2010. **97**(25): p. 253308.